Molecular Beam Epitaxy and Characterization of the Magnetic Topological Insulator (V,Bi,Sb)$_2$Te$_3$

15 83

Dissertation zur Erlangung des naturwissenschaftlichen
Doktorgrades der Julius-Maximilians-Universität Würzburg

vorgelegt von

Martin Winnerlein
aus Rosenheim

Würzburg, 2019

Eingereicht am: 26.09.2019
bei der Fakultät für Physik und Astronomie

1. Gutachter: Prof. Dr. Karl Brunner
2. Gutachter: Prof. Dr. Matthias Bode
3. Gutachter:
der Dissertation

Vorsitzender: Prof. Dr. Friedrich Reinert

1. Prüfer: Prof. Dr. Karl Brunner
2. Prüfer: Prof. Dr. Matthias Bode
3. Prüfer: Prof. Dr. Ronny Thomale
im Promotionskolloquium

Tag des Promotionskolloquiums: 22.07.2020

Doktorurkunde ausgehändigt am: ....

Contents

List of abbreviations

2D	Two-dimensional
3D	Three-dimensional
AFM	Atomic-force microscopy
AHE	Anomalous Hall effect
CPS	Counts per second
EDX	Energy-dispersive x-ray spectroscopy
FWHM	Full width at half maximum
IQHE	Integer quantum Hall effect
MBE	Molecular-beam epitaxy
PBN	Pyrolytic boron nitride
QAHE	Quantum anomalous Hall effect
QL	Quintuple layer
RHEED	Reflection high energy diffraction
RMS	Root mean square
SIMS	Secondary ion mass spectrometry
SQUID	Superconducting quantum interference device
TI	Topological insulator
UHV	Ultra-high-vacuum

XRD	X-ray diffraction
XRR	X-ray reflection
ZHP	Zero Hall plateau

1 Introduction

The discovery of the material class of semiconductors has slowly revolutionized the field of condensed matter physics. After more than a century of research, numerous applications like solar cells, LED displays and transistors in computer chips have been made possible and affect our daily lives profoundly. In 1988, Haldane presented a model predicting a new material class: topological insulators.[Hal88] In recognition of this groundbreaking work, Haldane was awarded the physics Nobel price together with Thouless and Kosterlitz in 2016.

Topological insulators typically consist of heavy elements, which cause significant spin-orbit coupling and energy corrections due to the relativistic mass-velocity term to the electronic band structure. These corrections can invert the electronic band structure, which makes these materials topologically distinct from trivial insulators. The inverted bands feature an energy gap resulting in insulating properties in the bulk. At the border between a topological insulator and a trivial insulator or vacuum these inverted bands must revert back causing topologically protected conducting Dirac surface states.

Many interesting physical phenomena like Majorana modes [FK08], image magnetic monopoles [QLZZ09], the topological magnetoelectric effect and axion electrodynamics [LWQZ10, EMV09] are predicted to be observable in topological insulators. Potential applications range from spintronic devices to quantum computing and resistance standards in metrology.

Since their prediction, topological insulators have quickly developed into a major field in modern condensed matter physics. In 2005, Kane and Mele proposed a two-dimensional topological state [KM05], the quantum spin Hall state, which was realized in 2007 in the Molenkamp group in HgTe quantum wells.[KWB$^+$07] Subsequently, in 2008, the topological surface states of the three-dimensional topological insulator alloy $\mathrm{Bi}_{1-x}\mathrm{Sb}_x$ were observed in ARPES measurements.[HQW$^+$08] In 2009, Zhang et al. predicted $\mathrm{Bi_2Se_3}$, $\mathrm{Bi_2Te_3}$ and $\mathrm{Sb_2Te_3}$ to be large gap three-dimensional topological insulators with single Dirac surface states at the Γ-point of the Brillouin zone. These stoichiometric compounds may maintain their insulating properties even at room temperature. While the predicted band structure, including the Dirac surface state, was soon confirmed in ARPES measurements [XQH+09, CAC+09], realizing a fully insulating bulk in transport measurements proved difficult.

The layered structure of these materials with weak van der Waals forces between the layers was found to harbor many crystal defects, like twin domains, antiphase domains, antisite defects and vacancy defects causing electronic doping in the bulk. While various attempts to reduce the residual bulk carrier concentration by e.g. counter doping, the reduction of crystal defects and the use of ternary materials led to considerable improvements, fully insulating bulk properties were not achieved.[MKS+18, TSL+14, HXY+12, RTS+10, TRS+11] Finally, in 2013, nearly fully insulating bulk properties were realized in thin Cr doped $(Bi,Sb)_2Te_3$ layers, which as a result exhibit almost only edge state conduction. The magnetic exchange coupling suppresses one edge state, causing the observation of the quantum anomalous Hall effect with little deviation.[CZF+13] In 2015, the quantum anomalous Hall effect was observed in V doped $(Bi,Sb)_2Te_3$ without deviations, proving the complete suppression of bulk conductance.[CZK+15b] The realization of a magnetic topological insulator featuring pure edge channel transport even in the absence of magnetic fields was a milestone in the development of topological insulators. In this material system, charge neutrality is achieved by mixing the n-type Bi_2Te_3 with the p-type Sb_2Te_3 at a specific ratio. Given that full suppression of bulk conductance was only observed in the magnetic system it seems that the magnetic doping plays a crucial role in localizing the bulk carriers.

Many questions regarding the magnetism, especially its coupling in such layers, and the exact mechanism of the quantum anomalous Hall effect remain unanswered and applications are severely limited by the low observation temperatures below 1 K. The experimental realization of the quantum anomalous Hall effect enables detailed studies of this new topological state of matter and is the primary goal of this thesis. The thesis is structured as follows:

- Chapter 1 gives a short introduction into the field and an overview of the thesis, which addresses the epitaxial growth and characterization of V doped $(Bi,Sb)_2Te_3$ magnetic topological insulator layers.

- Chapter 2 introduces the material class of topological insulators and the quantum anomalous Hall effect arising in magnetic topological insulators in particular.

- In chapter 3, the material system is introduced. The crystallographic structure and typical crystal defects and their influence on the electronic properties are discussed in detail. Furthermore, the origin of the inverted electronic band structure leading to the topological insulator properties and the quantum anomalous Hall effect are explained.

- In chapter 4, the method for the epitaxial growth of the topological insulator layers, molecular beam epitaxy, and the setup used in this thesis are described shortly. Characterization techniques are explained and the specific measurement conditions and setups used are outlined. Lastly, the photolithography process used to fabricate Hall bars and the cryogenic magneto-transport measurement techniques are briefly introduced.

- In chapter 5, the growth of pure Bi_2Te_3 and Sb_2Te_3 under varying growth conditions and on different substrates is studied. The ensuing crystal properties like the amount of twinning defects and the mosaicity-tilt are optimized and growth characteristics like the optimal temperature range for growth are determined.

- Subsequently, in chapter 6 mixed $(Bi,Sb)_2Te_3$ layers doped with V are investigated. Specifically, the substrate temperature and the Bi/Sb ratio and their influence on structural as well as magneto-transport properties is analyzed. The observation of the anomalous Hall effect allows a systematic optimization leading to the quantum anomalous Hall effect with fully suppressed bulk conductance.

- In chapter 7, the electronic and magnetic properties of the quantum anomalous Hall effect are studied in detail. The influence of substrate type, capping layer and layer thickness on structural and magneto-transport properties is investigated. High-precision measurements with metrological accuracy were prepared in collaboration with the Physikalisch-Technische Bundesanstalt and resonant photoemission spectroscopy measurements were conducted in collaboration with the group of EP7, characterizing the electronic states of Vanadium.

- In chapter 8, the influence of V doping on the structural and magnetic properties of the host material is studied systematically. To do so, a series of $(V,Bi,Sb)_2Te_3$ samples with increasing V content was fabricated and their surface morphology, composition, crystalline structure and magnetic properties are measured. This information is used to deduce the incorporation site of Vanadium.

- Chapter 9 focuses on heterostructures of magnetic and non-magnetic topological insulators. First, trilayer heterostructures with a non-magnetic layer sandwiched between two magnetic layers are investigated. These layers may act as axion insulators and feature a zero Hall plateau. Secondly, bilayers and trilayers with highly doped parts are studied. An unusual inverse sign of the anomalous Hall effect is observed and investigated further.

- In chapter 10, a comprehensive summary of the main results of the thesis is given.

2 Topological insulators and the quantum anomalous Hall effect

In this chapter, the new material class of topological insulators (TIs) is described and the quantum anomalous Hall effect (QAHE) as the consequence of the introduction of magnetism is explained.

After the observation of the quantum Hall effect in two-dimensional (2D) electron gases which exhibit 1D edge channels at large magnetic fields [TKNdN82], topology of bands was introduced as a concept to explain the accurate quantization of the Hall conductance:

$$\sigma_{xy} = n\frac{e^2}{h} \tag{2.1}$$

The Chern number n $\in \mathbb{Z}$ is equal to the number of edge channels and e^2/h is the inverse von Klitzing constant $R_K = h/e^2 = 25812.8074555\,\Omega$. Fig. 2.1 (a) shows a depiction of the edge channels for the quantum Hall effect. It was proposed that topologically non-trivial states of matter can also be achieved without applying a magnetic field to break time reversal symmetry.[KM05, BZ06] Instead, in material systems with strong spin-orbit coupling the energetic position of the conduction band and valence band can be inverted. This inverted band structure is topologically distinct from a non-inverted band structure and can not be reverted back by smooth transformation of the Hamiltonian. As a consequence, at the boundary between a TI with an inverted band structure and a trivial insulator (or vacuum) the conduction band and valence band have to cross generating a 2D surface state. These spin-polarized, metallic states are protected by time reversal symmetry and form a Dirac cone with a linear dispersion relation as shown in Fig. 2.2. The spins are perpendicular to the momentum direction and thus rotate by 2π along a Fermi surface arc. The wave function of an electron moving around such a closed loop will acquire an additional phase of π since spin 1/2 particles require a 4π rotation to acquire a phase shift of 2π.[OV15] This phase is called the Berry phase and is always π for TIs with insulating bulk and 0 for trivial insulators. The non-zero Berry phase in TIs is responsible for various phenomena like the suppression of backscattering due to destructive interference of wave functions for backscattered electrons.[ANS98]

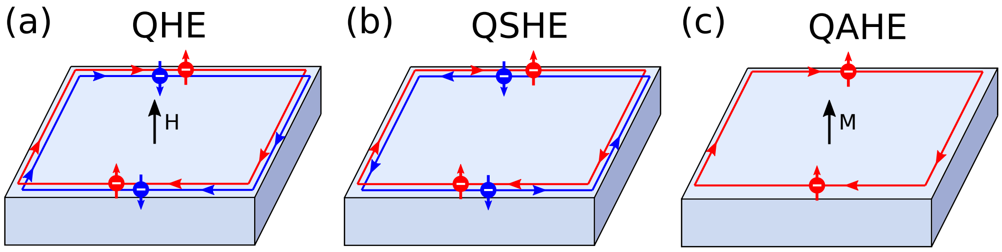

Fig. 2.1: Depiction of the edge states of the (a) quantum Hall effect, (b) quantum spin Hall effect and (c) quantum anomalous Hall effect.

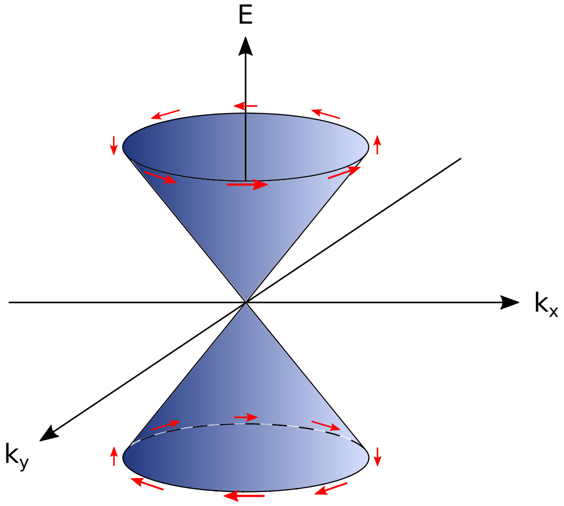

Fig. 2.2: Sketch of the dispersion of the surface states of a 3D TI in the form of a Dirac cone. The red arrows show the spin polarization.

When the thickness of a TI layer is decreased to only a few nanometers, the confinement effect restricts the momentum of the electrons on the z axis suppressing conduction of the four side surface states.[And13] The wave functions of the top and bottom surface states overlap and a hybridization gap opens.[ZHC$^+$10] Such a 2D TI features 1D edge states within the energy gap located at the boundary of the layer. The bands are spin-degenerate and thus provide two counter-propagating edge channels depicted in Fig. 2.1 (b). Transport through these channels causes the quantum spin Hall effect, which was experimentally observed in 2007 in HgTe-quantum wells.[KWB$^+$07] In a magnetic 2D TI, the introduction of magnetic dopants causes the ferromagnetic exchange interaction to shift the spin up and spin down bands. If this spin splitting has an opposite sign for the electron and hole bands and surpasses the hybridization energy, one of the spin states will become non-inverted.[LQD$^+$08] The remaining inverted band causes one chiral edge state at the boundary as depicted in Fig. 2.1 (c). Conduction through an edge channel is described by the Landauer-Büttiker formalism. [Büt86] In a typical four-point geometry the Hall conductivity is $\sigma_{xy} = e^2/h$ and the longitudinal conductivity $\sigma_{xx} = 0$ for the QAHE, reflecting the dissipationless transport through the chiral edge state. This signature of the QAHE was first observed in 2013 in Cr doped $(\mathrm{Bi,Sb})_2\mathrm{Te}_3$ layers.[CZF$^+$13]

In three-dimensional (3D) TIs an additional θ term is added to the Lagrangian to describe the electrodynamics [NN11]:

$$\mathcal{L} = \frac{1}{8\pi}(\epsilon \vec{E}^2 - \frac{1}{\mu}\vec{B}^2) + (\frac{\alpha}{4\pi^2})\theta \vec{E} \cdot \vec{B} \tag{2.2}$$

with $\vec{E}$ and $\vec{B}$ the electromagnetic fields, ϵ the dielectric constant, μ the magnetic permeability and $\alpha = e^2/\hbar c$ the fine structure constant. θ is either 0 for ordinary insulators or π for TIs. Nagaosa et al. [NN11] suggested a quantized Hall conductivity of $e^2/2h$ per surface state of a 3D magnetic TI as a consequence of these axion electrodynamics if the Fermi level lies within the gap of the surface Dirac fermions opened by the exchange interaction. The sum of the top and bottom surface state should thus result in a Hall conductivity of e^2/h equal to the Hall conductivity in 2D magnetic TIs exhibiting the QAHE.

3 The material system of $(V,Bi,Sb)_2Te_3$

Since Bi_2Se_3, Bi_2Te_3, and Sb_2Te_3 were predicted to be topological insulators, this material system has drawn much interest.[ZLQ+09] These chalcogenide crystals are built of stacked quintuple layers (QLs) consisting of five monolayers of e.g. Se-Bi-Se-Bi-Se on top of each other. Within the QLs strong covalent bonds act between the atoms, but only weak van der Waals bonds connect the QLs stacked on each other. The rhombohedral crystal structure of the trigonal space group $R\bar{3}m$ (D^5_{3d}) exhibits an inversion center in the Se/Te layer in the middle of a QL. The primitive cell consists of 5 atoms, but in crystallography a hexagonal basis with a unit cell consisting of 15 atoms is typically chosen. The crystal structure is displayed in Fig. 3.1. The lattice constants fulfill $a = b \neq c$ and the angles are given by $\alpha = \beta = 90°, \gamma = 120°$. The out-of-plane lattice constant c spans three QLs since the atomic layers forming hexagonal lattices are stacked in ABC or CBA stacking order and thus repeat after three QLs.

While the stacking order of the crystal can be transferred from the substrate, the limited coupling between substrate and layer via van der Waals forces usually results in the appearance of both stacking sequences. The crystal is thus not single crystalline anymore, but separated in individual domains of different stacking sequence called twin domains. The crystal can also be separated in individual domains at surface steps of the substrate called anti-phase domains. Furthermore, various point defects as well as stacking faults are typically found in this material as well.

The existence of an inversion center in the structure allows the calculation of well defined parity eigenvalues. The parity eigenvalues of the $P1^+_Z$ band of Bi or Sb and the $P2^-_Z$ band of Se or Te were found to be inverted in Bi_2Se_3, Bi_2Te_3 and Sb_2Te_3 due to the strong spin-orbit coupling as illustrated in Fig. 3.2.[ZLQ+09] This calculation led to the prediction that these materials are 3D TIs with an inverted

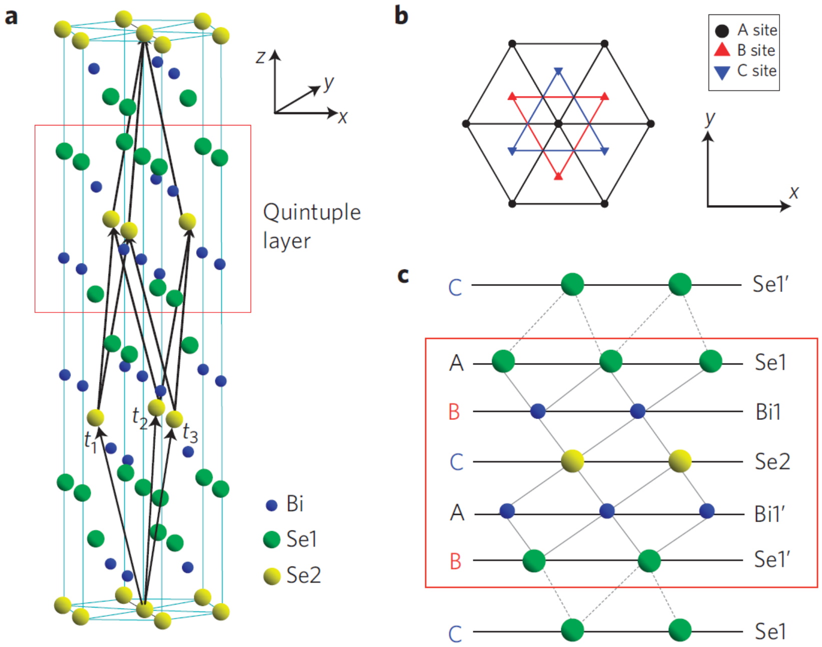

Fig. 3.1: (a) Side view of a unit cell of the Bi_2Se_3 crystal with the primitive lattice vectors $t_{1,2,3}$. (b) Top view of the hexagonal lattices with the sites A, B and C. (c) Side view of a quintuple layer with the stacking sequence $BACBA$.[ZLQ+09]

band structure.[ZLQ+09] At the edge of the sample these inverted bands have to revert back causing surface states at the crossing point. These surface states form a single Dirac cone at the Γ-point of the Brillouin zone within the bulk band gap and are protected by time-reversal symmetry. The calculated band structure of the three materials including the surface states are shown in Fig. 3.3.[ZLQ+09]

When the layer thickness of such a 3D TI is reduced sufficiently, it becomes a 2D TI with a hybridization gap. For Bi_2Se_3 angle-resolved photoemission spectroscopy measurements show the opening of the energy gap below 6 nm thickness.[ZHC+10] Despite significant efforts to realize these TIs experimentally, this was proven difficult. In real crystals the high number of crystal defects cause significant unintentional electronic doping resulting in a residual bulk conductivity and a shift of the Fermi energy into the bulk bands. Additionally, topologically trivial surface states may also contribute to the conductance.[dVPM+17] To realize a fully bulk insulating TI the defects have to be reduced or compensated, until pure surface conductivity is achieved.

Besides twin domains and anti-phase domains, point defects like anti-site and vacancy defects caused by the low polarity of the bonds play a major role. V_{VI} (group-V-on-group-VI) anti-site defects and group-V vacancies are electron accep-

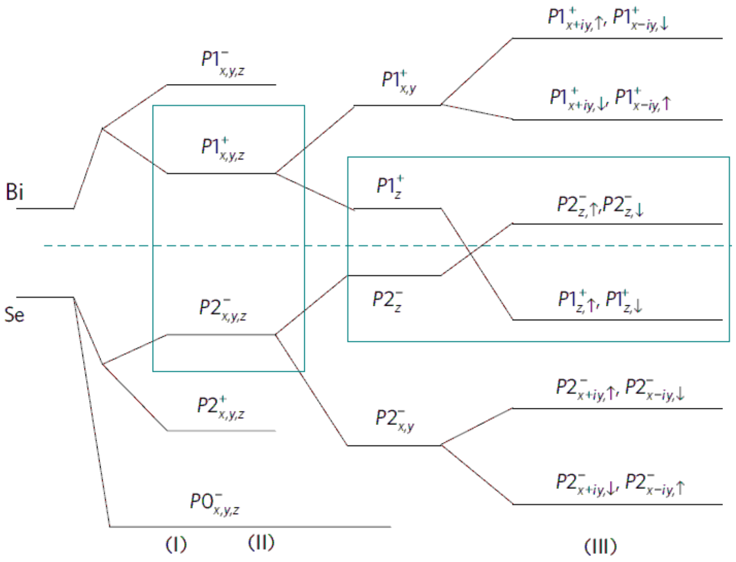

Fig. 3.2: Schematic of the evolution of the p orbitals of Bi and Se into the band structure of Bi_2Se_3 at the Γ-point. The stages (I), (II), (III) represent the effect of chemical bonding, crystal-field splitting and spin-orbit coupling, respectively.[ZLQ+09]

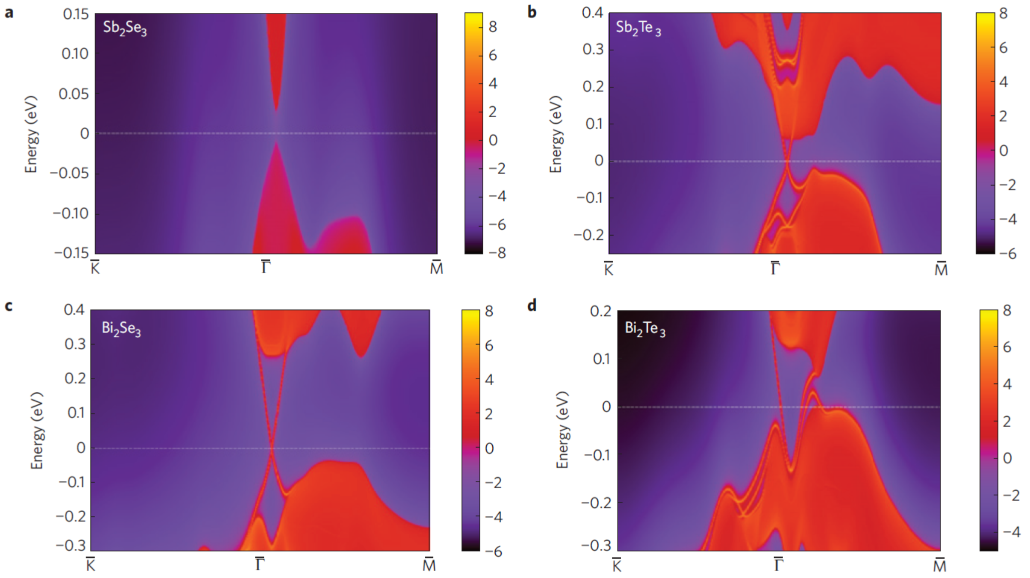

Fig. 3.3: Energy and momentum dependence of the local density of states of the bulk and surface states for the trivial insulator (a) Sb_2Se_3 and the topological insulators (b) Sb_2Te_3, (c) Bi_2Se_3 and (d) Bi_2Te_3.[ZLQ+09]

tors and cause p-type doping [JSC+12], while VI_V (group-VI-on-group-V) anti-site defects are electron donors [WZS+11]. Bi_2Se_3 typically features n-type conduction due to Se_{Bi} anti-site defects and V_{Se} vacancy defects.[XZZ+13] Bi_2Te_3 can exhibit n-type conduction due to Te_{Bi} anti-site defects for Te-rich growth conditions or p-type conduction due to Bi_{Te} anti-site defects for Bi-rich growth conditions.[FGT+88] Sb_2Te_3 can be dominated by Sb_{Te} anti-site defects for Sb-rich conditions or feature a mix of both anti-site defects as well as V_{Sb} vacancies for Te-rich conditions resulting in p-type conduction in both cases.

Various efforts were made to eliminate the bulk conduction by e.g. counter doping with Ca or Na, reducing defect densities or utilizing ternary materials. The bulk carrier concentrations could be reduced resulting in dominating surface conductance, but no fully insulating bulk was realized in the non-magnetic chalcogenides. [MKS+18, TSL+14, HXY+12, XHW+11, SLF+11, QHX+10, RTS+10, TRS+11, JSC+12]

Finally, in 2013, close to fully insulating bulk properties were realized in thin Cr doped $(Bi,Sb)_2Te_3$ layers, which exhibited the novel quantum anomalous Hall effect.[CZF+13] Perfect quantization with fully insulating bulk was achieved in V doped layers soon afterwards.[CZK+15b]

Given that fully suppressed bulk conduction was only observed in the magnetic system, it seems that magnetic doping plays a crucial role in localizing the bulk carriers. Still, the layers exhibit the QAHE only at very low temperatures in the mK range and typically need an applied gate voltage to fine-tune the position of the Fermi level. Furthermore, the layers require precisely controlled, specific growth conditions and material compositions. A major influence seems to be the Bi/Sb ratio in the layers, which presumably determines the position of the Fermi level. Since Bi_2Te_3 is typically n-type and Sb_2Te_3 p-type, a mixed alloy with compensating point defects is possible. Adding Bi to Sb_2Te_3 reduces the Sb_{Te} anti-site defects significantly, due to the increasing bond polarity.[SHSS88] The more ionic bonding of Cr or V may also play such a role. Besides the material composition, the surface temperature during growth and the group-V/VI flux ratio also affect the formation energy of the different point defects, e.g. a lower substrate temperature or a higher Te flux would result in less Te vacancies and Sb_{Te} anti-site defects, but more Te_{Sb} anti-site defects.[JSC+12] The optimization of these conditions and the reproduction of the QAHE is a major goal of this thesis.

4 Methods

The experimental methods used to fabricate and analyze the samples in this work are explained in this chapter. First, the deposition of the layers by molecular beam epitaxy (MBE) is described, then the characterization techniques reflection high energy electron diffraction (RHEED), x-ray diffraction (XRD), x-ray reflection (XRR), atomic force microscopy (AFM) and energy dispersive x-ray spectroscopy (EDX) are explained. Finally, a description of the photolithography process and cryogenic magneto-transport measurement techniques is given.

4.1 Molecular beam epitaxy (MBE)

Molecular beam epitaxy (MBE) is a technique for the deposition of thin-film crystals on a single crystalline substrate developed in the late 1960s. MBE offers unique advantages over other methods of crystal growth like chemical vapor deposition, including a precise control of beam fluxes and growth conditions and the absence of chemical reacting agents. Furthermore, low-temperature MBE realizes strong non-equilibrium growth conditions, which allow homogeneous incorporation of high doping concentrations above regular solubility limitations.[HTN+97] In this thesis a CreaTec MBE system was used to deposit crystalline thin films of magnetic TI layers. The system consists of a main chamber separated from a load lock by a valve to maintain ultra-high vacuum (UHV) conditions in the growth chamber while loading substrates. The load lock is pumped by a scroll pump creating a pre-vacuum and a turbo molecular pump to reach UHV. The main chamber is further pumped by a titanium sublimation pump and an ion getter pump resulting in a base pressure below 10^{-10} mbar measured by a Bayard-Alpert ionization gauge. UHV conditions are necessary to prevent unintentional doping and contamination of the layers by residual atoms before and during growth. Substrate holders can be transferred from the load lock onto the manipulator in the main chamber, where the substrate temperature can be controlled with a filament behind the substrate. The temperature is monitored with a thermocouple located at the same distance from the filament as the substrate. The 2-inch substrates are clamped on molybdenum sample holders with a pyrolytic boron nitride (PBN) plate behind the substrate for homogeneous heat distribution. During the crystal growth, the manipulator can rotate the substrate, which leads to a homogeneous distribution of the molecular beams over the substrate surface.

Material deposition is realized by thermal evaporation of ultra pure (99.9999%) elements from effusion cells pointing towards the middle of the substrate. The temperature and thus the beam fluxes are regulated accurately using filaments wound around the crucibles containing the material. The system is equipped with eight effusion cells filled with Bi, Sb, Cd, Te, Se, Cr, V and Al. Cooling shrouds around the cells and a cooling shield in the top half of the chamber are kept at -20°C to prevent cross contamination between the cells, remove waste heat and trap residual gas atoms. Most of the cells are standard effusion cells equipped with a PBN crucible, which can be operated up to 1400°C. During this thesis the cell used for V and its PBN crucible was replaced with a cell with a tungsten crucible designed for higher temperatures to reduce the high background pressure observed at the high operation temperature of 1400°C required for evaporation. This upgrade also enabled higher V fluxes necessary for V rich layers used in chapter 8 and 9.2.

Individual shutters in front of the effusion cells are used to block the beam flux to the sample, enabling sharp interfaces between different materials, which was utilized for the heterostructures in chapter 9. A RHEED system composed of an electron gun aimed at a grazing incidence angle to the substrate with a fluorescent detector screen on the opposite side is used to monitor the surface processes during deposition.

Prior to growth, the beam fluxes are typically determined by a Bayard-Alpert ionization gauge. The ionization gauge partially ionizes the flux and collects the ions resulting in a collector current $I_c = \sigma_i \cdot L \cdot n \cdot I_e$, with σ_i being the ionization cross section of a gas molecule, L the length of ionizing space, $n = P/kT$ the molecular density and I_e the electron emission current.[DWSY17] The displayed beam equivalent pressure is deduced using $P = I_c/(S \cdot I_e)$ with S being the gauge sensitivity factor. The sensitivity factor depends on the material and its temperature. A nominal sensitivity factor for nitrogen at room temperature is usually provided by the gauge manufacturer, but precise values depend on the state of the gauge and the geometry. The displayed BEP can thus deviate from the real pressure of a beam flux, but $P \propto \sigma_i \cdot n$ holds. Furthermore, $\sigma_i \propto \eta_i$ with η_i being the ionization probability. Thus, the flux $J \propto n \cdot \sqrt{\frac{T}{M}}$ is also $\propto \frac{P}{\eta_i} \cdot \sqrt{\frac{T}{M}}$ and the flux ratio between material x and y is thus given by: [JB93]

$$\frac{J_x}{J_y} = \frac{P_x \eta_y}{P_y \eta_x} \sqrt{\frac{T_x M_y}{T_y M_x}} \tag{4.1}$$

M_x is the mass of the molecular species x and the temperature T_x can be estimated as its source temperature. The size of the molecules depends on the material and its source temperature. The ionization probability relative to N_2 is given by: [JB93]

$$\eta/\eta_{N_2} = (0.4Z/14) + 0.6 \tag{4.2}$$

with Z being the sum of the atomic numbers of the atoms in the molecule. The calculated molecular beam flux multiplied by the provided number of atoms per molecule yields the atomic beam flux.

When the molecular beam reaches the substrate surface, the processes depicted in Fig. 4.1 can take place. Particles can adsorb, forming a weak physical bond, which allows surface diffusion or diffusion along a step edge. If a particle meets another particle, they can nucleate forming an island or reaching a step edge of an existing layer it can incorporate in the lattice forming strong chemical bonds. Without chemical bonds the particle may desorb after some time leaving the surface. Furthermore, atoms within the lattice may change place by interdiffusion. The probabilities of these processes depend on the growth conditions, like the substrate temperature and fluxes during growth or the deposited element, which affect e.g. migration lengths and desorption rates.

In this thesis, layered van der Waals crystals are grown, whose layers are only weakly coupled by van der Waals bonds, resulting in so-called van der Waals epitaxy. The weak bonds are not strong enough to convey strain to the layers, which relaxes the lattice matching condition between substrate and layer. For van der Waals epitaxy it is recommended to saturate the dangling bonds of the substrate before depositing the first layer.[WLG$^+$11] In this thesis, this is mainly achieved by dipping the substrate in 50% HF before growth resulting in a H passivated surface. Growth of these van der Waals crystals often occurs in growth modes like the step-flow growth or the spiral-growth. In the step-flow growth mode layers grow laterally starting at step edges of miscut substrates, while in the spiral-growth mode screw dislocations or jagged step edges act as pinning centers for the

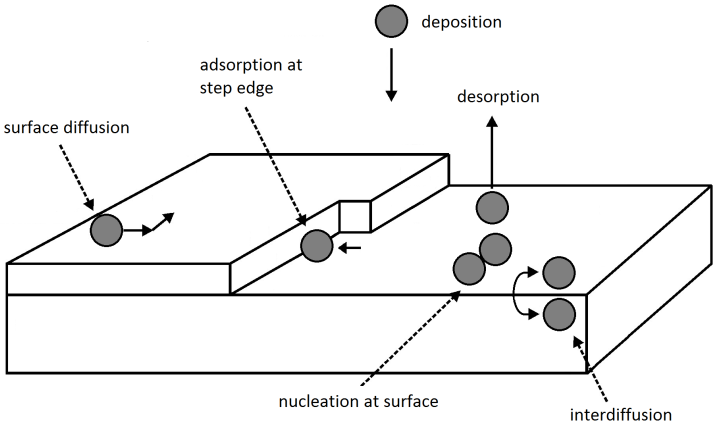

Fig. 4.1: Illustration of individual surface processes occurring during epitaxial growth.

growth of spirals [LNK+00, CL02, LWL12] Despite the weak interaction between substrate and layer, the layer quality was found to benefit from a small lattice mismatch promoting smooth, high quality layers. The weak interaction with the substrate can lead to loss of information about the stacking order of the substrate resulting in twin domains of different stacking orders in the layer.[WLG+11]

4.2 Reflection high energy electron diffraction (RHEED)

A common method to study the crystalline properties *in-situ* during deposition is reflection high energy electron diffraction (RHEED). This technique is based on the reflection and diffraction of a high-energy electron beam from the surface of the layer in UHV conditions. The RHEED system consists of an electron gun operated at 15 keV aimed at a glancing incidence angle below 3° at the crystalline sample surface, which reflects the electron beam onto a fluorescent screen mounted on the opposite site of the gun. The resulting specular spot as well as a diffraction pattern are observed and analyzed qualitatively with the naked eye or more quantitatively with a camera setup. Intensity oscillations of the specular spot during growth are often used to determine the growth rate, assuming the deposition of exactly one monolayer between two intensity maxima, which result from flat, fully closed layers.

The electrons can not penetrate deep into the flat layer, but interact only with the topmost atomic layers leading to a high surface sensitivity.[Has12] This causes a broadening of the reciprocal lattice points to rods perpendicular to the surface. The observed diffraction pattern can be understood by constructing an Ewald sphere around the incident electron wave vector as shown in Fig. 4.2.

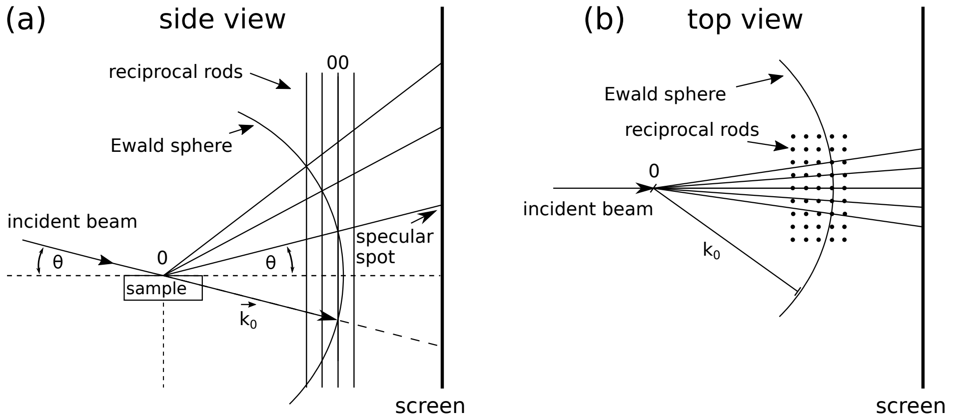

Fig. 4.2: Schematic illustration of a RHEED setup including the construction of the Ewald sphere.

At the intersections between the Ewald sphere and the reciprocal lattice rods, both the elastic scattering and the diffraction condition are fulfilled. The vectors from the center of the Ewald sphere to the intersections are wave vectors of the diffracted waves which cause a signal in their direction on the screen.[Has12] Note, that the Ewald sphere has a large radius with a finite extension due to the spread in electron energy and beam convergence and the reciprocal lattice rods are broadened by finite domain sizes and mosaicity tilt. This results in longer intersections, especially for flat layers with rods broadened by a small domain size or significant disorder causing streaks on the screen. The spacing between the streaks and their width reflects the lateral lattice constant and the crystalline quality, respectively. For surfaces consisting of small crystalline 3D islands, the electron beam transmits through the islands, the reciprocal lattice consists of points instead of rods and a spotty transmission pattern is observed on the screen. A rough 3D polycrystalline material with randomly oriented crystallites causes rings on the screen.

Sufficiently thick layers of high quality can furthermore cause Kikuchi lines to appear as a result of multiple scattering events. RHEED can also be used to analyze surface reconstructions, which are usually observed as additional intermediate streaks due to a periodic arrangement of ad-atoms at the surface in multiples of the lattice constant.

4.3 X-ray diffraction (XRD) and reflection (XRR)

X-ray diffraction (XRD) is a destruction free method used to analyze crystalline thin films. In this thesis, XRD is typically employed to study the crystal structure, lattice constants and crystalline quality in terms of tilt and twist mosaicity as well as twinning of thin films. Mainly, the Bruker D8 Discover system was used as well as occasionally a Panalytical X´pert MRD system. Given that the studied layers are very thin, the Bruker setup was optimized for high intensity over resolution. The primary beam is generated by a copper anode resulting in Cu $K_{\alpha 1}$ characteristic x-rays with a wavelength of 1.54056 Å. It passes through a 40 II Goebel mirror, a 0.2 mm slit and a Ge(022) asymmetric monochromator until it reaches the sample glued on a glass plate. For symmetric reflections the apertures on the secondary side consist only of two slits of 1.0 mm and 0.2 mm width. For the asymmetric reflections a soller aperture replaces the slits. A rotatable scintillation detector is used to detect the diffracted x-rays. The sample mounted on a goniometer can be rotated in various directions sketched in Fig. 4.3. The angle between incident beam and sample surface ω is usually kept equal to the Bragg angle θ, half the angle between incident beam and reflected beam, to fulfill the Bragg condition. The sample can furthermore be tilted along ψ perpendicular to ω and rotated full 360° along ϕ.

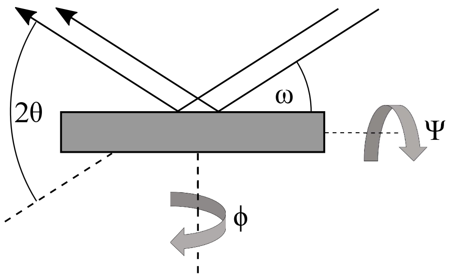

Fig. 4.3: Illustration of the relevant angles along which the goniometer can rotate the sample.

X-ray diffraction can be described by reflection at different lattice planes causing constructive interference. At specific angles, the differences in path length of beams reflected at lattice planes are integer multiples of the wavelength. This results in constructive interference as described by the Bragg equation:

$$\lambda = 2d_{hkl}sin(\theta) \tag{4.3}$$

with d_{hkl} being the spacing between the lattice planes and λ the wavelength of the x-rays. An alternative, equivalent condition can be deduced from scattering at individual atoms given by the Laue condition:

$$\vec{G} = \vec{k_{in}} - \vec{k_{out}} = \Delta\vec{k} \tag{4.4}$$

For constructive interference, the difference between the incident and diffracted wave vectors $\vec{k_{in}}$ and $\vec{k_{out}}$, called the scattering vector $\Delta\vec{k}$, has to be equal to a reciprocal lattice vector $\vec{G} = h\vec{b_1} + k\vec{b_2} + l\vec{b_3}$, with the primitive translation vectors of the reciprocal lattice:

$$\vec{b_1} = 2\pi\frac{\vec{a_2} \times \vec{a_3}}{\vec{a_1}(\vec{a_2} \times \vec{a_3})};\ \vec{b_2} = 2\pi\frac{\vec{a_3} \times \vec{a_1}}{\vec{a_1}(\vec{a_2} \times \vec{a_3})};\ \vec{b_3} = 2\pi\frac{\vec{a_1} \times \vec{a_2}}{\vec{a_1}(\vec{a_2} \times \vec{a_3})}; \tag{4.5}$$

$\vec{a_1}$, $\vec{a_2}$ and $\vec{a_3}$ are the primitive vectors of the Bravais lattice with the relation $\vec{a_i}\vec{b_j} = 2\pi\delta_{ij}$ and form the Bravais lattice vector $\vec{r} = x\vec{a_1} + y\vec{a_2} + z\vec{a_3}$.

Using the Laue equation, diffraction can be described conveniently with the reciprocal space, in which each point represents reflection at a specific set of planes. The Laue condition can be visualized using the Ewald sphere as shown in Fig 4.4. The origin of the lattice is at the tip of the incident wave vector and the Ewald sphere is displaced to the origin of the incident wave vector. The magnitude of $\vec{k_{out}}$ is used for the radius of the Ewald sphere, which is equal to the magnitude of $\vec{k_{in}}$ due to elastic scattering. Any cut between the Ewald sphere and a reciprocal lattice point fulfills the Laue condition. In standard $\omega_{\pm}$ geometry, the accessible part of the reciprocal space is limited by absorption of the sample and the wavelength of the x-rays to the light gray area sketched above the sample.

The position of the reciprocal lattice points is given by the reciprocal lattice vector with the magnitude $|\vec{G}_{hkl}| = 2\pi/d_{hkl}$ with the Miller indices h, k and l and the direction perpendicular to the planes. It is thus tied to the out-of-plane lattice constant c and in-plane lattice constant a, which in the hexagonal material system are given by [Bir06]:

$$\frac{1}{d_{hkl}^2} = \frac{4}{3}\frac{h^2 + hk + k^2}{a^2} + \frac{l^2}{c^2} \tag{4.6}$$

The lattice constant c can thus be deduced from the position of symmetric peaks with $h = k = 0$ determined from a $2\theta - \omega$ scan, which is also called $2\theta - \theta$ scan. This scan rotates sample and detector simultaneously, and cuts through the reciprocal space along the direction of the origin to the studied reciprocal lattice point. The observed broadening of the peaks in k_z direction is due to the finite

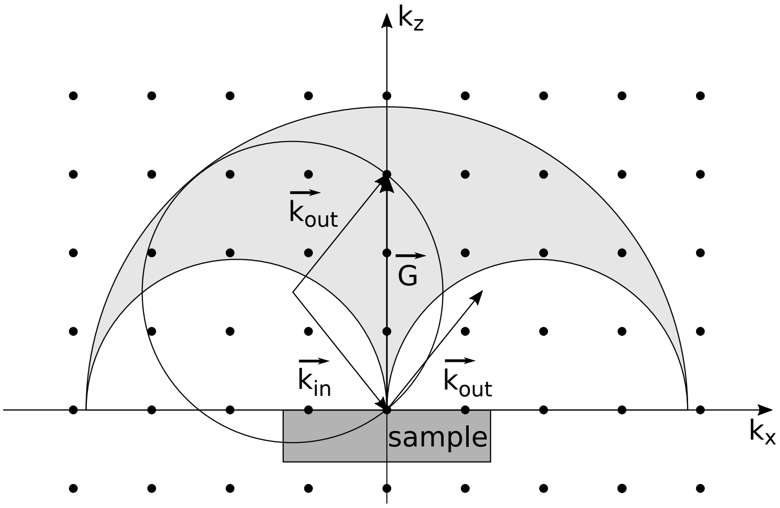

Fig. 4.4: The Ewald sphere constructed around the origin of the incident wave vector cuts through a reciprocal lattice point enabling diffraction. Only reciprocal lattice points in the light gray area are accessible due to limitations of the geometry and the used wavelength.

crystallite height, which is usually equal the film thickness in thin films and given by the Scherrer formula:

$$L = \frac{K \cdot \lambda}{\Delta(2\theta) \cdot cos\,\theta} \tag{4.7}$$

with L the crystallite height, K the shape factor close to unity and $\Delta(2\theta)$ the full width at half maximum (FWHM) of the reflection in radian. Similarly, the finite lateral crystallite size leads to broadening of the reflections in the k_x and k_y directions. This can be observed in rocking curve scans, in which the sample is tilted around ω at a fixed 2θ detection angle, leading to a cut through the reciprocal space along an arc around the origin. For symmetric reflections this arc is approximately in the (k_x, k_y) plane. Additionally, the peak is broadened by the out-of-plane tilt of the mosaic crystallites along this arc. These two broadening mechanisms can be distinguished by choosing an asymmetric reflection where the arc deviates significantly from the k_x direction or by analyzing a series of symmetric reflections, which will be affected differently by the two broadening mechanisms depending on their distance from the origin. The latter is called the Williamson-Hall like analysis and is described in detail in [DLRHT11].

In the case of unconventional mosaic crystals, a two-component peak consisting of a broad peak affected by the lateral crystallite size and the mosaicity tilt as well as a narrow Bragg peak is observed in rocking curve scans. This narrow peak is likely a result of partially coherent scattering between individual crystallites with limited displacement towards each other and is regularly observed in the material

system studied in this thesis.[DLRHT11]
Besides symmetric reflections, asymmetric reflections with non-zero h or k can be measured by tilting the sample in ω or ψ direction until the respective planes are in reflection geometry. Measuring the position of such an asymmetric reflection gives access to the in-plane lattice constant a using equation 4.6 since h, k or both are non-zero.
Measuring an asymmetric reflection while rotating the sample around ϕ can be used to probe the rotation of the domains around the z-axis. In the Sb_2Te_3 material system three $\{015\}$ peaks are expected in a 360° pole scan due to the threefold symmetry of the material. Twin domains rotated by 60° will cause three additional peaks whose integrated intensity relative to the original three peaks equal the degree of twinning in the layer. The spread in the in-plane rotational orientation of the domains, called mosaicity twist, is given by the FWHM of the peaks.

The XRD setup was furthermore used for x-ray reflection (XRR) measurements. XRR is based on the interference of x-rays reflected from the surface and interfaces between different materials, e.g. between air and layer or layer and substrate, as sketched in Fig. 4.5. While the layer does not have to be crystalline, it needs sufficient density contrast to the substrate and a high reflectivity.

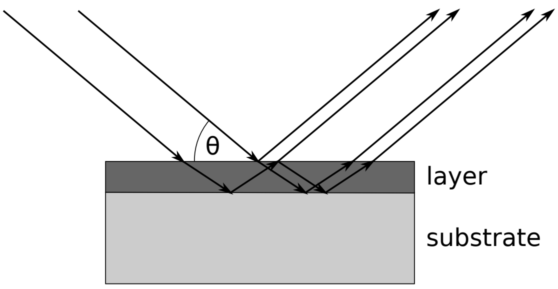

Fig. 4.5: Illustration of x-ray reflection at the interfaces between air, layer and substrate.

The XRD was set up with the same apertures used for symmetrical reflections and sample and detector are rotated simultaneously during a $2\theta - \omega$ scan at low grazing incident angles. Total reflection is observed up to the critical angle θ_C, which depends on the mass density of the material. At slightly higher angles the intensity oscillates due to constructive or destructive interference causing a pattern of so-called Kiessig fringes. The spacing between maxima can be used to determine the layer thickness using the following equation [Bir06]:

$$d = \frac{\lambda}{2 \cdot (sin(\theta_{m+1}) - sin(\theta_m))} \approx \frac{\lambda}{2 \cdot (\theta_{m+1} - \theta_m)} \tag{4.8}$$

with d the layer thickness and θ_m the angle of the maximum of the fringe of the order m. For an accurate determination of layer thickness, surface- and interface roughness simulations were performed with the ”Leptos” software from Bruker and fitted to the data. An example of such a fit for a 52 nm thick (V,Bi,Sb)$_2$Te$_3$ layer is shown in Fig. 4.6.

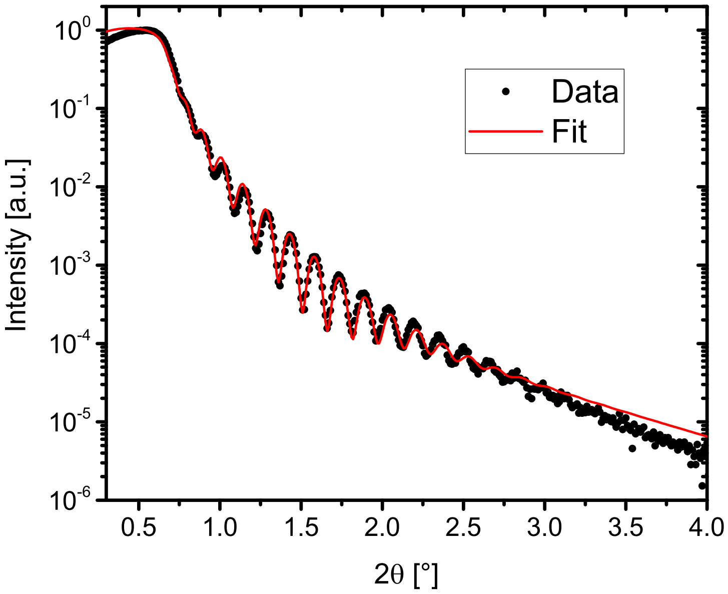

Fig. 4.6: XRR scan of a 52 nm thick (V,Bi,Sb)$_2$Te$_3$ layer on a Si(111) substrate with the data points in black and the fitted simulation in red.

4.4 Atomic force microscopy (AFM)

Atomic force microscopy (AFM) is a measurement technique, which can determine the topography of a sample surface. A small area of the surface is probed by a tip with a small diameter mounted on a cantilever which is systematically scanned in the xy-plane across the surface. Such small and precise movement can be realized by utilizing piezoelectric actuators. During this scanning process the tip interacts with the topmost surface atoms by Van der Waals forces.

In the tapping mode used in this thesis, the cantilever is oscillated at a frequency close to the resonance frequency, which shifts due to forces acting on the tip. This results in a damping of the oscillation since the excitation frequency is not adjusted to the new resonance frequency. The oscillation amplitude of the cantilever is monitored by measuring a laser beam reflected at the back of the cantilever with a photo-detector. If the damping is observed to change, a feedback loop coupled to a piezoelectric element adjusts the tip-sample distance of the cantilever to keep the damping constant. This constant damping results in constant forces and a constant distance to the surface as well, thus the movement of the cantilever mirrors the topography of the sample. The described setup of an AFM is depicted in Fig. 4.7.

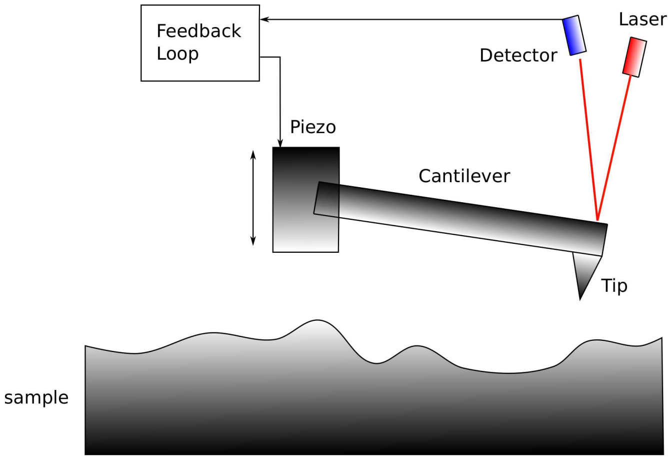

Fig. 4.7: Sketch of an AFM setup.

In this thesis, a DME DualScope 95-50 scanner equipped with Si tips is employed. Due to the finite diameter of the tip the resulting image is a convolution between the topography of the tip and the surface. This limits the lateral resolution to the tip radius of around 10 nm, while the vertical resolution is below 1 nm. The AFM is operated in air, which can cause artifacts due to acoustic noise, air moisture, air flow and dust particles. Typical image corrections are applied to minimize the effect of such artifacts. The line mean procedure shifts each scan line to the same average height, which reduces the impact of low frequency noise. A plane is subtracted from the image to flatten the result and remove the effect of a tilted sample. In some cases, conservative FFT filtering was applied to remove specific noise frequencies from the image.

In this thesis, the resulting image is typically analyzed in regard to island shape, height and size, and the roughness is quantified as root mean square (RMS) rough-

ness defined as $R_q = \sqrt{\frac{1}{n}\sum_{i=1}^{n} y_i^2}$ with y_i the deviation of each measurement point i from the average height. For an accurate comparison of the RMS roughness between samples, the measurement conditions like scan speed and the employed tips are kept as comparable as possible.
AFM images are presented with two numbers next to the scale bar: one indicates the full height scale from the lowest to the highest point represented by the full bar, while the number in brackets provides the range of the color code from black to white, which is smaller due to the removal of outliers necessary to provide a high contrast.

4.5 Energy dispersive x-ray spectroscopy (EDX)

Energy dispersive X-ray spectroscopy (EDX) is typically used to quantitatively analyze the chemical composition of samples. It is based on the detection of characteristic x-rays caused by the interaction of the sample with an electron beam. The UHV setup used in this thesis utilizes the electron beam of a scanning electron microscope (Phillips XL30) and an ”EDAX” Si(Li) detector to analyze the emitted x-rays.
The electron beam, accelerated with a high voltage, can excite and eject core electrons of the atoms in the sample, if the energy is sufficient. The electron hole can then be filled by an electron from a higher shell causing the energy difference to be transmitted as a characteristic x-ray, which is distinct for each element. This process is illustrated in Fig. 4.8 (a) for a K-L transition. These x-rays are detected and the relative intensity of the individual element specific lines is used to determine the chemical composition of the sample. The deceleration of the electrons of the beam in the sample furthermore causes Bremsstrahlung, which is detected as a broad background.
An acceleration voltage of 12 kV is applied in this thesis, which results in efficient excitation and a high signal from the V K-$L_{2,3}$ transition allowing the detection of even small V doping concentrations. The count rate of the detector is regulated to about 2000 counts per second (CPS) by limiting the beam spot size to yield a high acquisition rate, while keeping sum peak artifacts in check. Such artifacts occur when two x-ray photons hit the detector at the same time and are interpreted as one photon with the sum of the energy.
The lateral resolution of bulk samples in EDX is typically several µm due to

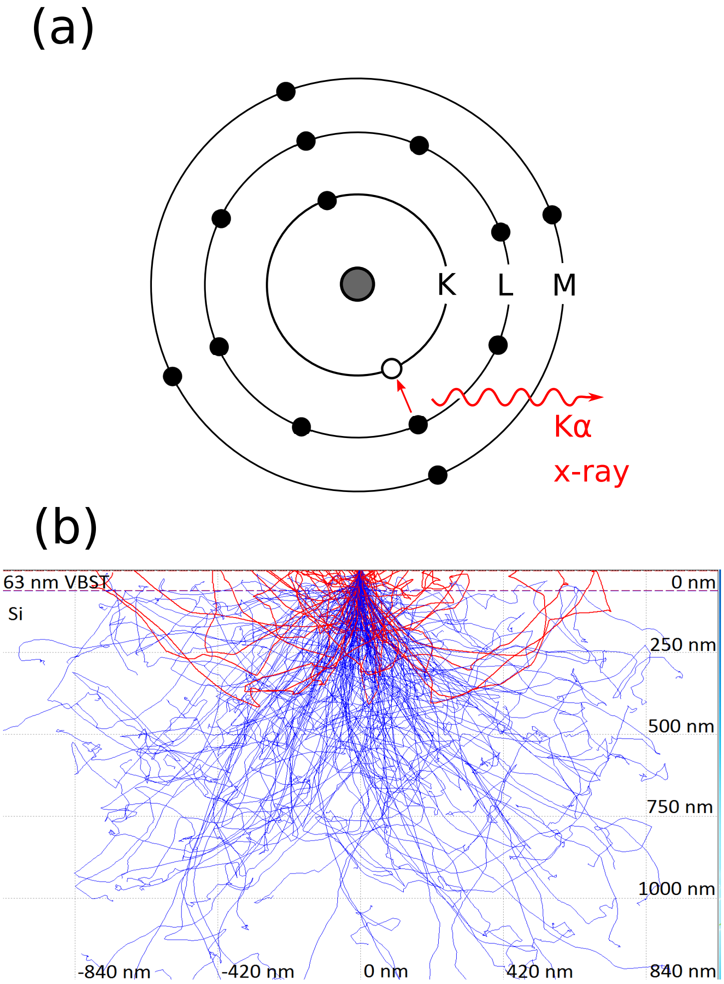

Fig. 4.8: (a) Illustration of the generation process of characteristic x-ray emission. (b) Simulated electron trajectories in a 63 nm thick $(V,Bi,Sb)_2Te_3$ layer on top of a Si substrate for an electron beam of 10 nm diameter using the CASINO program [DRCJ$^+$07].

the broadened pear-shaped interaction volume of the electrons in the sample. In the case of a thin layer on a substrate most of the broadening takes place within the substrate, though. A simulation using the CASINO program [DRCJ$^+$07] of the electron trajectories for an electron beam of 10 nm diameter in a 63 nm thick $(V,Bi,Sb)_2Te_3$ layer on Si is shown in Fig. 4.8 (b). While the low thickness of the layer helps maintain a high lateral resolution the signal intensity of thin films is low. To improve the signal intensity from the thin film, a low grazing incident angle between electron beam and sample surface can be used to increase the interaction volume in the layer. A grazing incident angle of 10° between electron beam and sample surface is typically used in this thesis.

To quantify the elemental composition of the sample the ”NIST-DTSA-II” software is used to simulate and fit the measurement curves.

4.6 Photolithography and magneto-transport measurements

The lithography and magneto-transport measurements in this thesis were conducted by Stefan Grauer, Kajetan Fijalkowski and Matthias Hartl in the spintronics and quantum transport group of EP3.
A structure with two Hall bars was defined by optical lithography to conduct the magneto-transport measurements. Typically, a bigger Hall bar with dimensions of 600 x 200 μm^2 and a smaller Hall bar with dimensions of 30 x 10 μm^2 were fabricated with 6 contacts each and a gate on top as shown in Fig. 4.9. The results from the two Hall bars do not differ qualitatively, so no distinction was made.

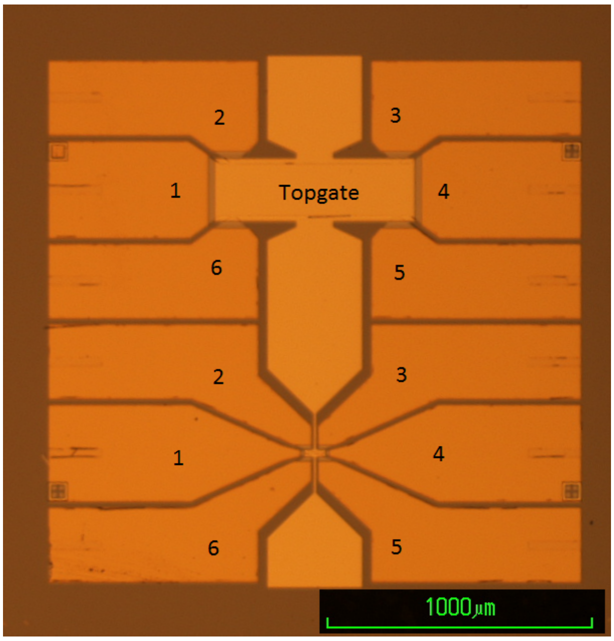

Fig. 4.9: A small and a big Hall bar structure after lithography with 6 contacts each and a topgate.

The films were patterned either by ion beam etching with Ar^+ or by wet etching with a brom:ethylene glycol (1:200) solution. After removing the Te capping layer at the contact areas, metallic contacts of 50 nm AuGe, 5 nm Ti and 50 nm Au were deposited by evaporation in an UHV chamber. A top gate is fabricated by atomic layer deposition of a 20 nm thick insulating AlO_x and 1 nm HfO_x layer with a metal electrode of 5 nm Ti and 100 nm Au on top. The processed samples are finally glued in chip carriers and the contacts are connected to the carrier by ultrasonic wire bonding. The sample in the chip carrier can be mounted on a sample stick for measurements in ^{4}He cryostats at 4.2 K or 1.8 K when pumped. ^{3}He-^{4}He dilution refrigerator cryostats were used for even lower temperatures in the 10-100 mK range.

Measurements are performed by standard low frequency lock-in techniques with a magnetic field applied in perpendicular direction. The current flowing from contact 1-4 through the sample is determined by the voltage drop over a reference resistor and the longitudinal resistivity ρ_{xx} and Hall resistivity ρ_{xy} are calculated from the voltages measured between the contacts 2-3 or 5-6 and 2-6 or 3-5, respectively. The Hall conductivity σ_{xy} and longitudinal conductivity σ_{xx} can be determined from the resistivities with the following equations:

$$\sigma_{xy} = \frac{\rho_{xy}}{\rho_{xx}^2 + \rho_{xy}^2} \qquad \text{and} \qquad \sigma_{xx} = \frac{\rho_{xx}}{\rho_{xx}^2 + \rho_{xy}^2} \tag{4.9}$$

5 Structural characterization of epitaxial Bi_2Te_3 and Sb_2Te_3

5.1 Analysis of Bi_2Te_3 films

The topological insulator Bi_2Te_3 has a large indirect band gap of 165 meV hosting topologically protected surface states within.[CAC$^+$09] While for intrinsic Bi_2Te_3 the Fermi level is located within the energy gap, in real materials the Fermi level commonly lies within the bulk conduction band, thus n-type bulk conductance is observed. This is due to the formation of Te_{Bi} antisite defects in the layer, which act as electron donors.[WZS$^+$11] Furthermore, the Dirac point is located close to the valence band edge. It has been shown that doping Bi_2Te_3 with transition metals like Mn can lead to stable ferromagnetism in the alloy.[HRB$^+$10, CCC$^+$04] By mixing n-type Bi_2Te_3 with p-type Sb_2Te_3 it is possible to shift the Fermi energy into the bulk band gap. With additional magnetic doping, bulk conductance can be fully suppressed, leading to the observation of the QAHE.[CZF$^+$13] In this chapter, the growth of pure Bi_2Te_3 is studied to better understand its growth properties and its influence on the growth of mixed $(Bi,Sb)_2Te_3$ alloys.

The Bi_2Te_3 layers are grown by MBE and their dependence on growth parameters like substrate temperature, growth rate as well as the used substrate type and surface preparation is analyzed. The properties investigated include the mosaicity-tilt and -twist of the crystal, the appearance of twinning defects and the topography of the surface.

The layers were grown by operating a Bi effusion cell at temperatures between 585°C and 606°C resulting in BEPs between 1.0×10^{-8} mbar and 2.3×10^{-8} mbar and a Te effusion cell at 360°C with a resulting BEP of 1.3×10^{-6} mbar. The Te:Bi BEP ratio is always above 50 in the Te overpressure regime, to avoid the formation of Bi rich phases, Te vacancy and Bi_{Te} antisite defects. During and after the growth, RHEED shows streaks suggesting a relatively smooth layer growth.

The first step is to establish the growth of pure Bi_2Te_3 with expected lattice constants and close to parallel alignment to the substrate planes. In Fig. 5.1, a wide range $2\theta - \theta$ XRD scan of a representative sample is shown. The 003, 006, $00\underline{15}$, $00\underline{18}$ and $00\underline{21}$ reflections are visible, while the 009 and $00\underline{12}$ reflections are strongly suppressed as it is typical for Bi_2Te_3. The 111 and the 222 reflections of the Si substrate are visible too, confirming the nearly parallel orientation of the (00n) layer planes to the (111) substrate planes. No additional peaks of other phases were detected. The out-of-plane and in-plane lattice constants c and a were determined for all samples by equation 4.6 using d_{006} and d_{015}. The average value of c and a is 30.41 Å and 4.394 Å with standard deviations of 0.02 Å and 0.002 Å, respectively. No correlation between the lattice constants and the substrate temperature or growth rate was observed in the sampled regime. In the literature, the reported lattice constants depend on the growth conditions and methods employed, though. MBE grown samples show a lattice constant c of 30.4 Å for lower Te overpressure, consistent with our results, and 29.9 Å for high Te overpressure favoring Te_{Bi} antisite formation.[CKD$^+$99] Samples grown by melting techniques show values of c and a of 30.497 Å and 4.386 Å.[Nak63] Such slight differences are expected due to the differing growth conditions.

5.1.1 Influence of substrate temperature and growth rate

In the following, the influence of the substrate temperature T_{Sub} during growth on the structural properties of the layers is investigated. A series of samples was grown at T_{Sub} =190°C, 220°C, 260°C, 300°C and 320°C with the same Bi cell temperature of 606°C and a growth time of 4 hours. The resulting layer thicknesses were generally measured by XRR, only for the samples grown at 300°C and 320°C the thickness was estimated with the Scherrer formula given in equation 4.7 using the measured FWHM of the 006 reflection instead. This was necessary since no Kiessig fringes were visible for the rough layer surfaces. The calculated growth rate is shown in Fig. 5.2 against T_{Sub}. At low substrate temperatures a growth rate of 11.1 nm/h corresponding to a thickness of 44.4 nm is observed. The growth rate starts to decrease strongly between 260°C and 300°C and decreases further at 320°C. This can be explained by partial desorption of the offered Bi atoms at elevated temperatures. The Te atoms, offered in excess in the Te overpressure

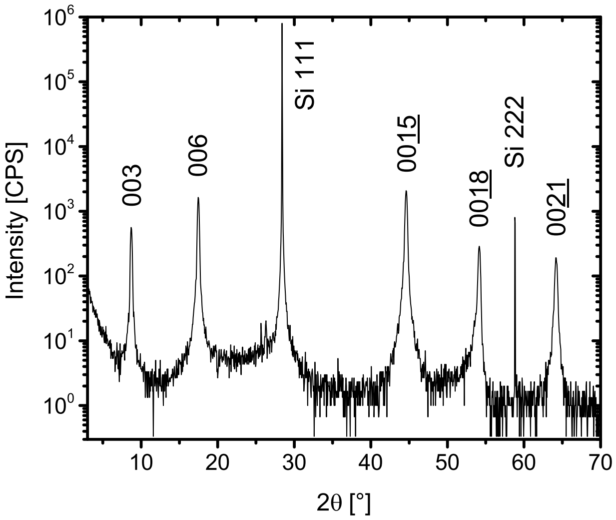

Fig. 5.1: $2\theta - \theta$ XRD scan of a representative 38 nm thick Bi_2Te_3 layer grown on a Si(111) substrate.

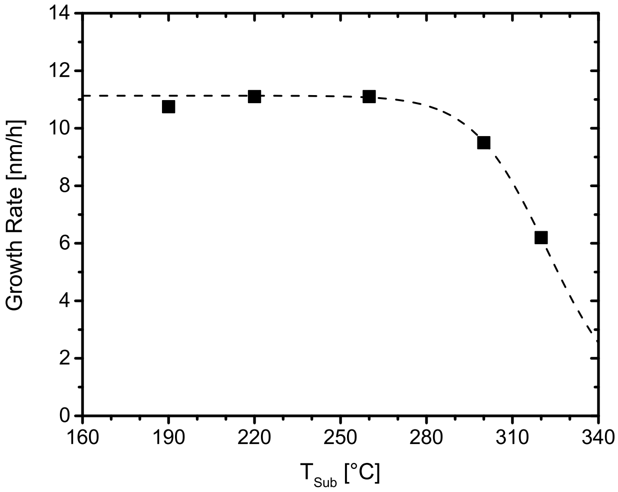

Fig. 5.2: The growth rate of the layers in dependence of the substrate temperature T_{Sub} during growth. The dashed line represents the performed fit based on equation 5.1.

regime, desorb at these temperatures if they do not react with a Bi partner. At lower temperatures an additional nucleation of amorphous Te atoms is possible, but is not observed here. At 190°C the growth rate is even slightly decreased as a consequence of the formation of flakes at lower temperatures, which do not contribute to the layer thickness determined by XRR. The actual growth rate with the material in the flakes included is likely to be consistent with the growth rate at 220°C.

The temperature dependence of the incorporation rate can be described by modifying equation (6) in [WDSW82]. For the incorporation constant K' a thermally activated behavior is assumed now, analog to the desorption, with a negative activation energy E_k corresponding to the binding energy of Bi_2Te_3. For the binary Bi_2Te_3, both fluxes simplify to J_{Bi}. The following equation is thus derived:

$$r_{inc} = J_{Bi}^2/(\frac{D_0}{K_0} \cdot \exp(-\frac{E_d - E_k}{k_B T}) + J_{Bi}) \tag{5.1}$$

J_{Bi} is the arrival rate of Bi atoms, D_0 and K_0 desorption and incorporation constants and E_d and E_k the activation energy for desorption and the binding energy. The incorporation rate multiplied by the volume of a unit cell divided by the number of Bi atoms per unit cell yields the growth rate. The growth rate is thus direct proportional to the incorporation rate and can be fitted similarly. The sample at 190°C was excluded for the aforementioned reason and the result of the fit is shown as a dashed line. The combined activation energies $E_d - E_k$ were determined to be (2.3 ± 0.5) eV, which agrees within the error with the expected value for the enthalpy for vaporization of Bi of 1.86 eV [ZEY11]. While the error is significant, it indicates that the reduced growth rates at higher temperatures are indeed due to thermal desorption of Bi from a mobile precursor state before reacting with Te.[JZS+91] For the further analysis the samples at 300°C as well as 320°C were not included due to a significant unintentional miscut of more than 1° for both substrates.

The samples grown at 190°C, 220°C and 260°C were further characterized by XRD. Rocking curve scans of the 006 reflection are shown in Fig. 5.3 (a). The dashed line indicates the peak position expected for layer planes parallel to the substrate planes. For all three layers the broad diffuse peak shows nearly parallel alignment to the substrate in the probed horizontal measurement axis ω. The FWHM of these peaks is 0.67°, 0.50° and 0.45°, decreasing with increasing T_{Sub}. This can be interpreted as a reduction of the mosaicity-tilt or an increased domain size. This is commonly observed for higher T_{Sub} due to an increased diffusion length of the atoms at the surface during growth.

Apart from the intense diffuse peaks, two very narrow Bragg peaks are observed for each sample. These peaks indicate the existence of long-range structural correlations as they are observed in unconventional mosaic crystals whose individual mosaic blocks can scatter X-rays coherently with respect to each other.[DLRHT11] The slightly deviating angles relative to the broad peak and the dashed line indicate a small misalignment to the substrate planes, likely a result of the small unintentional miscut of the substrate. The FWHM is resolution limited by the

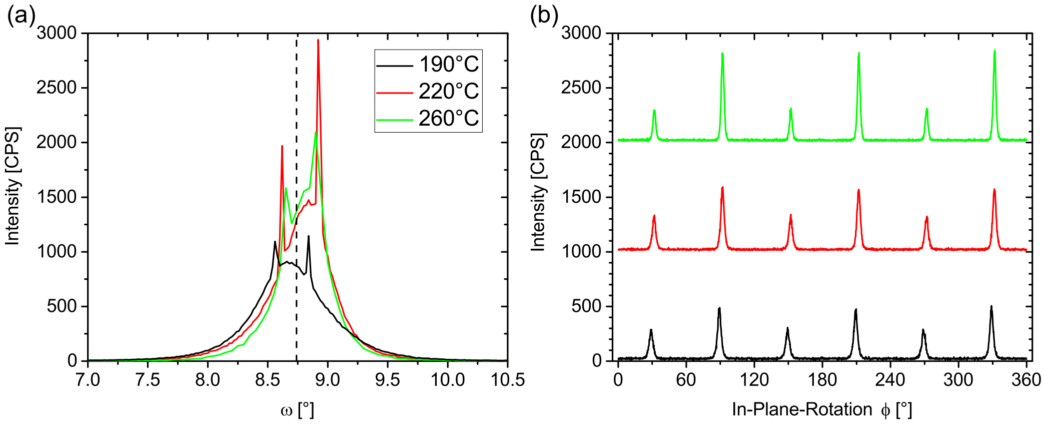

Fig. 5.3: (a) Rocking curve scans of the 006 reflection of the three samples grown at 190°C (black), 220°C (red) and 260°C (green). The dashed line represents the angle parallel to the (111) substrate planes. (b) shows the in-plane rotation diffractogram of the {015} peaks of the same three samples offset by 1000 CPS for clarity.

instrument and will be analyzed in greater detail on a more suitable sample later in this chapter.

In Fig. 5.3 (b) in-plane rotation scans of the {015} peaks of the same samples are shown with an offset for clarity. The FWHM of these peaks is decreasing with increasing T_{Sub} from 3.7°, 3.5° to 2.6°. While the reduced value at 260°C seems to indicate an improved crystalline quality with a smaller mosaicity-twist, it can not be ruled out that the cause are fluctuations between samples which are regularly observed in such layers.

The observation of six peaks at 60° intervals for all three samples indicate twinning in the layers, since the threefold rotational symmetry of Bi_2Te_3 is expected to cause only three peaks at 120° intervals in the absence of twinning. The three {015} peaks aligned with the Si(004) planes of the substrate have a higher intensity, proving that one twin is favored by the substrate, while the other is partially suppressed. In [KBP+15] the authors suggest that the stacking order of the substrate is transferred vertically to the layer despite the Te passivation layer in between. Another possible explanation would be that the information about the stacking order is passed laterally at step edges from the substrate to the layer as it happens on rough InP substrates.[TSL+14] The degree of twinning can be quantified by the ratio of the integrated peak intensities of the minority twin to the majority twin, e.g. at 100% both twins are equally present. At 190°C and 220°C suppressed twinning of 54% and 55% is observed, while at 260°C the twinning is reduced further to 38%. This reduction at higher T_{Sub} is probably caused by the larger diffusion length of the atoms, which allows them to settle on the energetically preferred site of the favored twin.

In Fig. 5.4 2×2 µm^2 AFM images of the surface of the three samples are shown, while 5×5 µm^2 images were used to calculate the RMS roughness of the surfaces. At 190°C (Fig. 5.4(a)) there are elongated protrusions visible. These flakes are thin slabs of misoriented QLs, which grow under a steep angle from the surface to about 20 nm height. Underneath these flakes, there is a layer structure consisting of islands of about 100-200 nm side length. The flakes are typical for low growth temperatures and lead to a very high RMS roughness of 7.1 nm. At 220°C (Fig. 5.4(b)) no flakes are detected anymore and the islands show a typical triangular form with spiral growth. The island size has increased to about 500 nm side length and terraces of about 40 nm width are observed. Steps of about 1 nm height, consistent with the height of a QL step of $c/3$, separate these terraces. The RMS roughness has decreased significantly to 1.4 nm due to the absence of flakes. Triangles pointing in opposing directions show domains of opposite twinning [TSL$^+$14] consistent with the observation of twinning in the XRD in-plane rotation scans. At 260°C (Fig. 5.4(c)) the islands have merged to a closed layer with an increased terrace width of about 300 nm. Some holes of about 15 nm depths have formed, though, permeating about 1/3 of the layer and increasing the RMS roughness significantly to 2.3 nm. Overall, an increase of T_{Sub} leads to a significant increase of the island and terrace size as expected for longer diffusion lengths.

Additional samples were grown with reduced growth rates and higher T_{Sub} to further enhance the diffusion length and possibly the twin suppression. Sample 1 was grown at 260°C at half the previous Bi flux resulting in half the growth rate. In the absence of desorption, the growth rate is directly proportional to the flux. The growth time was increased to 6.5 hours maintaining a thickness of 35 nm. At 300°C, desorption prevents the nucleation and growth of Bi_2Te_3 at this low Bi flux. Thus, for the growth of sample 2 at 300°C a 1.5 times higher Bi flux was chosen to compensate for the desorption. This results in a similar growth rate as sample 1 with 26 nm grown over 4 hours. For the growth of sample 3 at 300°C a low initial Bi flux, similar to sample 1, was ramped to the 1.5 times higher flux of sample 2 over 3 hours. After half an hour of this slow nucleation process, RHEED shows full Bi_2Te_3 coverage of the Si substrate. After another 3 hours with constant flux the layer thickness reached 46 nm.

In the following, these three samples as well as the sample grown at 260°C of the previous series are analyzed. Comparing the two samples grown at 260°C reveals the influence of the growth rate, while comparing sample 1 and 2 shows the im-

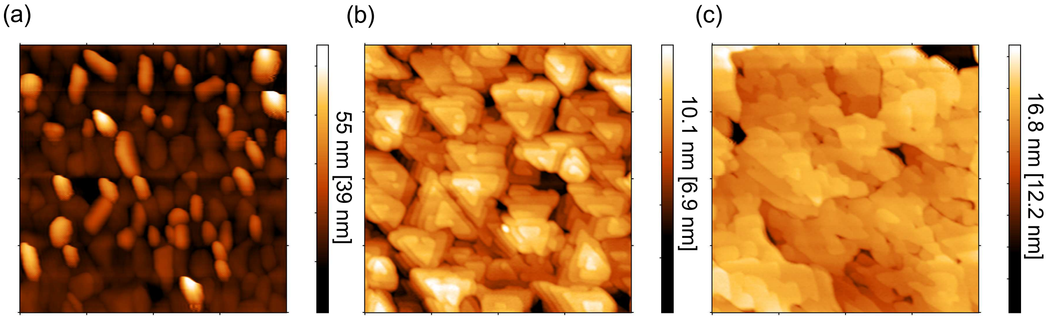

Fig. 5.4: 2×2 µm^2 AFM images showing the surface of the layers grown (a) at 190°C, (b) 220°C and (c) 260°C.

pact of a higher T_{Sub} when the growth rate is kept constant by compensating for the desorption. The consequences of extremely slow nucleation can be observed in sample 3.

In Fig. 5.5 (a) the rocking curve scans of the 006 reflection are shown for the four samples. All 4 samples exhibit broad diffuse peaks with additional small sharp peaks. Comparing the reference sample grown at 260°C and sample 1, a small increase of the FWHM from 0.45° to 0.55° is observed, indicating a slight increase in mosaicity-tilt or decrease in domain size. The expected enhanced surface migration length at lower growth rates did not lead to an improved quality. This could be caused by the adsorption of more contaminants during the longer growth time. Given that thicker layers often tend to have a lower FWHM, the reduced layer thickness of sample 1 may also play a role. Sample 2 exhibits a significantly reduced FWHM of 0.34° compared to sample 1 due to the increased T_{Sub}. This continues the trend observed in the previous T_{Sub} series grown at higher growth rates. Sample 3 shows a slightly higher FWHM of 0.45° than sample 2. The very slow nucleation process seems to have a negative impact on the crystalline quality, possibly due to the accumulation of contaminants on the exposed sample surface before the nucleation starts.

Fig. 5.5 (b) shows the in-plane rotation scans of the reference layer and sample 1, 2 and 3. The FWHM averaged over the 6 peaks is 2.8°, 2.9°, 3.1° and 2.8° respectively. In contrast to the apparently improved quality for higher T_{Sub} observed in the previous series, increasing T_{Sub} further to 300°C leads to no significant change. Overall, the FWHM are very similar, the differences do not exceed typical fluctuations between individual samples. Neither the change in T_{Sub} nor in the initial or continuous growth rate results in an improved quality regarding mosaicity-twist.

The in-plane rotation scans provide further information about the twinning in the layers. The quantification of the twinning yields 38%, 46%, 32% and 50% for the

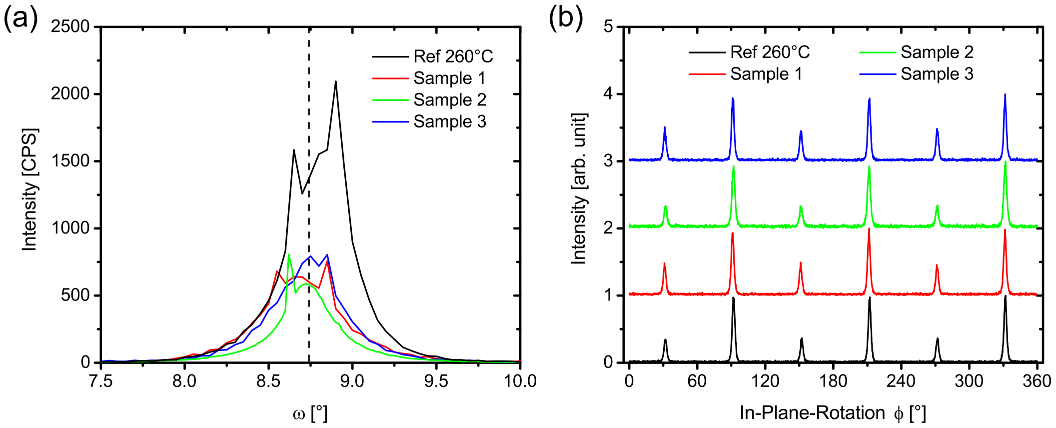

Fig. 5.5: (a) Rocking curve scans of the 006 reflection of the reference sample grown at 260°C, sample 1 grown at half the growth rate, sample 2 grown at 300°C at the same growth rate as sample 1 and sample 3 with a Bi flux slowly increasing above the nucleation limit during growth. The dashed line represents the angle parallel to the (111) substrate planes. (b) shows an in-plane rotation diffractogram of the {015} peaks of the same 4 samples with a normalized intensity and an offset of 1 for clarity.

4 layers, respectively. Reducing the continuous or initial growth rate seems to lead to significantly more twinning defects. This is in contrast to [KBP+15] reporting improved twin suppression for lower growth rates at 300°C. This discrepancy may be caused by differences in the substrate surface like unintentional miscuts and the surface roughness, which is known to influence twinning. The comparison between sample 1 and 2 shows the influence of T_{Sub} on the twinning defects. At the higher T_{Sub} of 300°C a significant reduction of twinning is observed, continuing the trend of the previous T_{Sub} series.

Now the $5{\times}5\,\mu m^2$ AFM images of the 4 samples shown in Fig. 5.6 are studied. In (a) the previously discussed surface of the Ref 260°C sample is shown as a reference. In (b) the surface of sample 1 grown at half the growth rate is shown. The morphology seems similar to the reference, the RMS roughness of 2.6 nm is comparable to 2.3 nm of the reference. There are no signs of an enhanced migration length as it was suggested in [KBP+15] for lower growth rates. In Fig. 5.6 (c), sample 2 grown at 300°C at the same growth rate shows larger terraces and some triangular edges typical for Bi_2Te_3. Deep holes seem to permeate the whole 26 nm thick layer causing an increased RMS roughness of 3.5 nm. The increased terrace size as well as the larger holes continue the previously observed trend for increasing T_{Sub}. While the larger terrace size is likely the result of an increased migration length, the deeper holes may be caused by the desorption of material at 300°C or the formation of pits and clusters on the Si surface at 300°C as observed

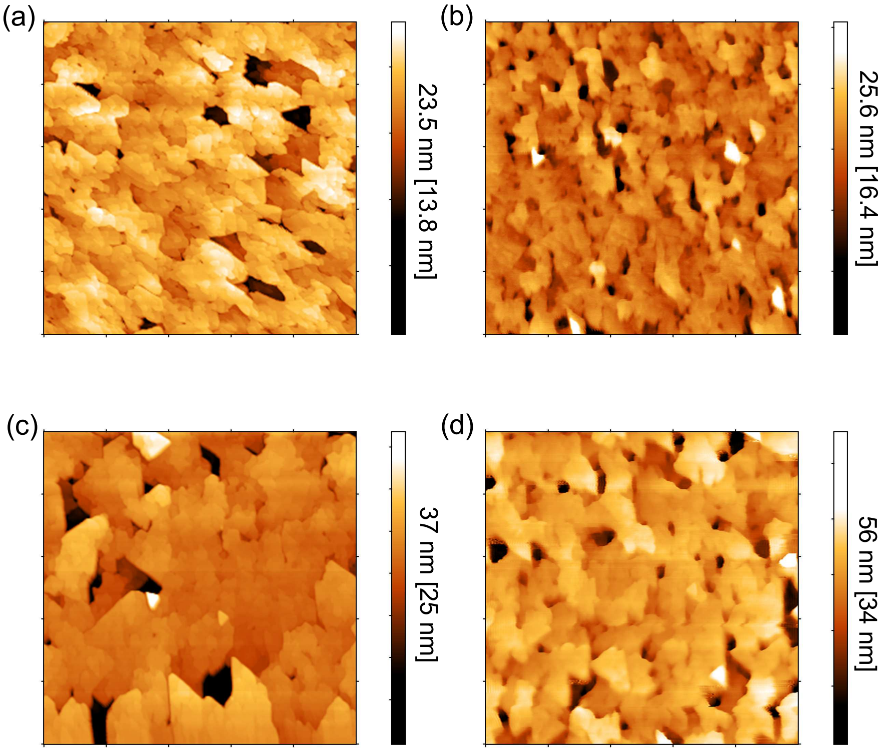

Fig. 5.6: 5×5 µm^2 AFM images showing the surface of (a) the reference sample grown at 260°C, (b) sample 1 grown at 260°C and half the growth rate, (c) sample 2 grown at 300°C at the same growth rate as sample 1 and (d) sample 3 with the Bi flux slowly increasing above the nucleation limit.

in [HFM$^+$01]. Sample 3 shown in Fig. 5.6 (d) exhibits less interconnected islands, likely due to twinning defects. Deeper holes are present due to the higher layer thickness increasing the RMS roughness further to 6.0 nm.

In summary, an elevated substrate temperature T_{Sub} above 260°C during growth is found to cause desorption of Bi atoms resulting in thinner layers. At only 190°C, the layers are slightly thinner as well, since some of the Bi_2Te_3 is not incorporated into the layer, but forms misoriented flakes instead. Increasing T_{Sub} from 190°C to 260°C reduces the mosaicity-tilt from 0.67° to 0.45° and the twinning from 54% to 38%, likely due to the increased surface migration length. Increasing T_{Sub} further to 300°C necessitates an increased flux to compensate for desorption. This results in further improvement of the mosaicity-tilt to 0.34° and even less twinning of 32%. Enhancing the surface migration length further by reducing the growth rate by 1/2 reduces the quality, though. Similarly, the slow increase of the Bi flux above the nucleation limit results in higher levels of twinning and more mosaicity-tilt. The cause of this deterioration may be the increased contamination before and during the slower growth process. The mosaicity-twist fluctuates around 3° between the samples with no clear influence from T_{Sub} or the growth rate. AFM images of the surface show a strong increase of the island size with increasing T_{Sub} from 150 nm to more than 1 µm as well as larger terraces between the QL steps. For $T_{Sub} = 260°C$ or above, consistent with the onset of desorption, deep holes appear increasing the RMS roughness dramatically.

5.1.2 Influence of substrate type and preparation

In the following, the influence of the substrate on the structural properties of about 26 nm thick Bi_2Te_3 layers grown at $T_{Sub} = 300°C$ is studied in detail. Different substrate types and miscut angles are employed and the roughness and surface reconstruction is tuned by annealing sequences.

Previously, the layers were grown on Si(111) substrates, which were dipped in 50% HF solution immediately before loading them into the MBE system. The H-passivated substrates were then heated to the specified T_{Sub} before initializing growth, without an annealing or outgassing step beforehand. After opening the cell shutters, the H passivation may be replaced by a Te passivation immediately. [TSD+17] Sample 2 from the previous series is used as a reference sample employing this standard preparation. Alternatively, several pre-growth annealing sequences of the HF etched substrates were tested: Annealing at 700°C for 10 min, 3 h or at 750°C until the 7×7 reconstruction was confirmed in RHEED. Annealing at 700°C causes desorption of the hydrogen passivation. Thus, a Te flush was necessary prior to growth to saturate the Si dangling bonds and enable the van der Waals epitaxy. Annealing at 750°C leads to the formation of the 7×7 reconstruction of the Si(111) surface after which the sample is cooled down to T_{Sub} before performing a Te flush. Furthermore, the sample with an unintentional miscut of about 1° of the first series was included to study the effect of such a miscut. This sample was grown at a 1.5 times higher growth rate, though, resulting in a 1.5 times higher thickness of 38 nm. Finally, a Fe:InP(111)B substrate with a rough surface was prepared with an HF dip and no annealing. Prior to growth a spotty RHEED pattern indicated a rough surface of this substrate.

In Fig. 5.7 the rocking curve XRD scans of the 006 reflection of the samples

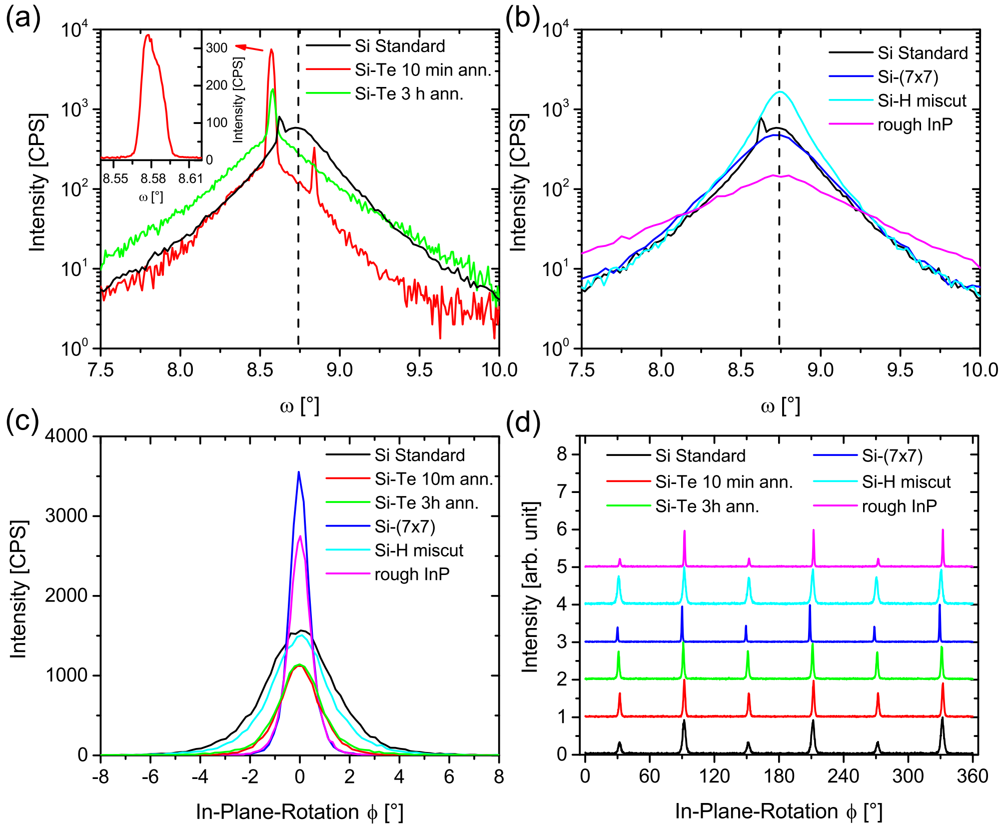

Fig. 5.7: (a) and (b) show XRD rocking curve scans of the 006 reflection of about 30 nm thick Bi_2Te_3 layers grown on different substrates. Details about substrate type and preparation are indicated in the legend. The dashed lines indicate the angle parallel to the (111) substrate planes. The inset in (a) shows an additional high-resolution scan of the narrow peak component observed for the 10 min annealing preparation. (c) shows the in-plane rotation diffractogram of the {015} planes with the peak maximum fixed to zero. (d) shows the full 360° in-plane rotation diffractograms with a normalized intensity and an offset of 1 for clarity.

are shown in logarithmic plots and are separated in two groups, the presumably smoother substrates are shown in (a) and the rougher substrates in (b) with the standard preparation sample shown in both as a reference. This reference sample exhibits mainly a broad diffuse peak with a FWHM of 0.34° positioned on the dashed line, indicating parallel alignment to the substrate planes. A small sharp Bragg peak tilted 0.1° to the substrate planes is also present.

Annealing the substrate for 10 mins at 700°C significantly enhances the sharp Bragg peak of the layer, while the intensity of the broad diffuse peak is decreasing correspondingly. This shows a massively improved long-range-order with either very large domains or structural coherence between the domains. The FWHM of the broad diffuse peak increased slightly to 0.5°, possibly a consequence of the lowered intensity. The FWHM of the sharp peak is limited by the resolution of the employed detector and apertures. A more accurate measurement with a high resolution triple-bounce analyzer and smaller slits is shown in the inset of Fig. 5.7 (a). The FWHM was found to be 0.018° (65") and is still resolution limited, indicating a strongly ordered crystal. The maximum of the broad diffuse peak shifted by 0.17° to the position of the sharp Bragg peak, which indicates misalignment to the substrate planes. Total reflection measurements show that the surface of the substrate instead of its planes is parallel to the (00n) layer planes. The alignment parallel to the substrate planes typically causes the crystal to separate in antiphase domains vertically displaced towards each other due to the surface steps of the substrate. Alignment parallel to the surface prevents this displacement leading to the observed enhanced long-range-order. The mechanism by which the annealing causes this alignment is not entirely clear. It is known, though, that the details of the annealing sequence and the miscut angle and direction influence the regularity of the steps, their height, step bunching, the density of kinks in the steps as well as the surface reconstruction.[LPV$^+$98] It is likely, that the unintentional miscut of our substrates is not aligned to a specific crystallographic direction causing many kinks along the steps. The annealing for 10 mins may form a more regular pattern of steps, possibly with fewer kinks along the steps, facilitating the growth parallel to the surface plane.

Annealing for an increased duration of 3 h weakens the sharp peak and strengthens the diffuse peak, which shows an unchanged FWHM of 0.5°. The partial loss of long-range-order may be due to the formation of bunched steps like triple steps breaking the regularity of the single stepped surface and causing disorder. The extended annealing duration could also increase the contamination of the surface. The XRD scan in Fig. 5.7 (b) shows that annealing at a higher temperature of 750°, which results in the 7×7 reconstruction, causes the sharp peak to vanish. The diffuse peak maintains a FWHM of 0.5°. XRR scans show that the substrate is miscut about 0.6° in the ψ-axis perpendicular to the ω-axis. In this case, rocking curve scans along the ω-axis are not suitable to determine if the layer planes are aligned to the substrate planes or surface plane. AFM images show a step bunched surface with an angle matching the 0.6° miscut, though. This shows that the layer planes are aligned to the substrate planes causing vertical displacements of the QLs at the step edges which destroys the long-range order.

Next, the sample grown on the 1° miscut substrate without prior annealing is studied. The layer planes are aligned to the substrate (111) planes and no sharp

Bragg peak is observed in rocking curve scans. The FWHM of 0.24° of the peak reflects the improved quality, possibly due to the 1.5 times higher growth rate. The larger miscut angle and the lack of annealing probably cause an irregular step pattern with bunched steps, which can explain the absence of long-range-order as well as the parallel orientation of the layer planes to the substrate planes. The layer grown on rough InP(111) exhibits the highest FWHM of 0.8° due to the large roughness of the surface. The substrate features no relevant miscut and the layer planes are aligned with the substrate planes.

Now the mosaicity-twist as well as twinning are analyzed based on the in-plane rotation ϕ scans shown in Fig. 5.7 (c) and (d), respectively. The standard preparation shows the largest mosaicity-twist of 3.2° and 32% twinning. Annealing the substrate at 700°C reduces the mosaicity-twist to 1.8-1.9°, irrespective of the annealing duration. The source of the high mosaicity-twist for the standard preparation sample may be the kinks and irregular steps on the substrate surface, which can be reduced by the annealing sequence. Annealing also seems to increase the twinning to 65% and 80% for 10 mins and 3 h, respectively. On rough, non-miscut InP(111) annealing was reported to increase twinning due to the reduction of steps on the surface, which can transfer stacking information laterally to the layer.[TSL$^+$14] While annealing a miscut surface will not result in a surface without steps, the observed alignment parallel to the substrate surface plane avoids lateral bonds between substrate and layer at the steps, hindering the transfer of stacking information. The Si(111)7×7 reconstruction formed at 750°C seems to reduce the mosaicity-twist even further to 0.9°. This could be related to the significant reduction of kinks along steps caused by the large unit cell of the 7×7 reconstruction.[LPV$^+$98] Long steps without kinks may act as a reference for the orientation of the layer reducing the rotational disorder. Twinning is reduced to 42%, which may indicate the formation of additional surface steps.

The miscut sample shows a slightly reduced mosaicity-twist of 2.6° compared to the non-vicinal sample with standard preparation. The small difference may be caused by fluctuations between samples or the different growth rate. The miscut does not seem to have a significant influence. The twinning is significantly increased to 78%, though. This may seem surprising considering that a miscut typically leads to more steps on the surface, but a higher miscut can also lead to the formation of triple steps lowering the amount of steps present.[WWG$^+$92] High resolution images of the surface directly after annealing would be necessary to clarify the mechanism behind the increased twinning.

The layer on the rough InP(111) substrate shows a narrow peak with a FWHM of

1.0° as it is commonly observed on InP due to a reduced lattice mismatch.[STK+13] Twinning is strongly reduced to 28%, consistent with previous observations, presumably due to many steps on the surface.[TSL+14]

The surfaces of the layers on different substrates were also measured by AFM shown as 5×5 μm^2 images in Fig. 5.8. The previous standard preparation (Fig. 5.6(c)) yields a mostly closed layer with small terraces separated by QL steps and no separation in individual islands. Some deep holes permeating the layer down to the substrate lead to an increased RMS roughness of 3.5 nm, though. The layer on 10 mins annealed substrate (Fig. 5.8(a)) shows a different topography with about 2 μm big islands with large atomically flat terraces up to about 1 μm. An additional 10×10 μm^2 image was provided in (Fig. 5.8(f)). Some trenches and pits are present, but significantly reduced compared to the standard preparation sample. This leads to a much lower RMS roughness of 2.0 nm for the 10×10 μm^2 image and 1.3 nm for the 5×5 μm^2 image, which contains no deep hole down to the substrate. The large interconnected islands reflect the strong long-range-order observed as sharp Bragg peak in XRD in the absence of displacements at surface steps. The layer grown on a substrate annealed for 3 h (Fig. 5.8(b)) shows smooth, interconnected areas separated by deep trenches down to the substrate. These trenches proceed from the top to the bottom of the image, causing a large RMS roughness of 8.3 nm. No terraced islands are visible but individual terraces of about 300 nm width. It is possible that the trenches are caused by step bunching of the Si substrate during the longer annealing. The separated areas can still partially grow together since the parallel alignment of the layer planes to the surface plane avoids displacement at steps.

The 7×7 reconstructed substrate (Fig. 5.8(c)) shows a strongly step bunched layer surface with deep trenches causing a high RMS roughness of 7.7 nm. Triangular structures are visible pointing either in an upward or downward direction perpendicular to the step edge, consistent with the twinning observed in the in-plane rotation scan. In contrast to the 700°C annealed samples, every 700 nm a vertical offset of about 2-15 nm is seen between the two sides of a trench. The accumulated offset of 50 nm over the 5 μm of the image fits well to the observed substrate miscut of 0.6°. This indicates that the layer planes are parallel to the substrate planes and not to the surface plane. The layer on a 1° miscut substrate (Fig. 5.8(d)) shows similar step bunching with an accumulated height offset of 90 nm along 5 μm corresponding to the larger miscut. The RMS roughness of 6.8 nm is comparable. In contrast to the previous sample, where the high annealing temperature has likely resulted in step bunching, here the larger miscut angle is a probable cause. A

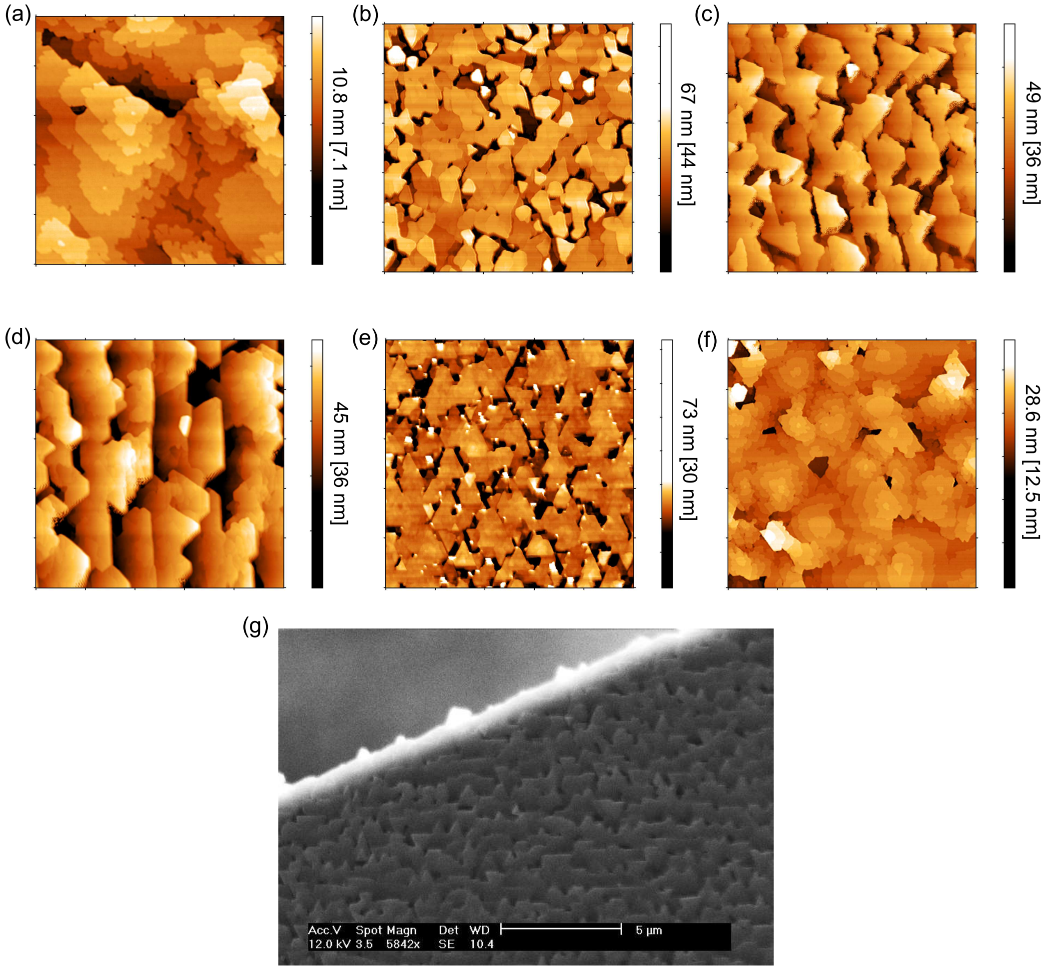

Fig. 5.8: $5\times5\ \mu m^2$ AFM images showing the surface of about 26 nm thick Bi_2Te_3 layers grown (a) on 10 min at 700°C annealed Si, (b) 3 h at 700°C annealed Si, (c) 750°C annealed 7×7 reconstructed Si, (d) 1° miscut Si substrate (layer is about 38 nm thick) and (e) rough InP substrate. (f) shows a larger $10\times10\ \mu m^2$ AFM image of the 10 min at 700°C annealed Si and (g) shows a large area SEM image of the layer on the 1° miscut Si substrate.

larger scale SEM image shown in Fig. 5.8 (g) reveals many jagged edges along the steps. The SEM image furthermore proves that the unusual surface structure with large triangles is not a result of a tip artifact. Finally, the surface of the layer on rough InP (Fig. 5.8(e)) shows deep trenches as well, but no preferential direction since the substrate has no miscut. A large majority of triangular domains point in the upward direction reflecting the strong twin suppression observed in the XRD in-plane rotation scan. The domain size is limited to about 500 nm, probably due to the large roughness of the surface, and only few QL steps are visible on the surface.

In conclusion, either long-range order or twin suppression can be enhanced by employing specific substrates. Layers grown on 700°C annealed Si substrates are oriented parallel to the surface plane, slightly misaligned to the (111) planes, due to a small unintentional miscut. The annealing at 700°C seems to induce this alignment, likely due to the formation of a regular single step pattern. The alignment to the surface plane helps to avoid vertical displacement at the steps and enhances long-range order observed as very narrow Bragg peak in the rocking curve scan. Likewise, AFM images show large islands with more than 1 μm side length. On the other hand, the layer planes do not connect to the substrate steps anymore, which typically transfer stacking information to the layer and suppress twinning. As a result, the annealing of substrates at 700°C leads to increased twinning.

Annealing the substrate at 750°, until the 7×7 reconstruction forms, results in different layer properties. The layer planes align to the Si(111) planes, which leads to a step bunched surface corresponding to a slight unintentional miscut of the substrate. This alignment causes the loss of long-range order due to coherence breaking at substrate steps. The mosaicity-twist has improved to 0.9°, which may be due to the reduction of kinks along the steps caused by the 7×7 reconstruction. A suppression of twinning defects is observed, likely due to the transfer of stacking information at step edges possible for this alignment.

Similarly, a 1° miscut substrate, which was not annealed, had the layer planes aligned to the Si(111) planes, which prevents long-range order. The higher miscut likely resulted in an irregular bunched step pattern, preventing the alignment of the layer planes to the surface plane. Consequently, the layer surface morphology shows step bunching corresponding to the miscut angle. In contrast to the layers on 7×7 reconstructed substrates, an increased mosaicity-twist and a high degree of twinning is observed.

Finally, a rough Fe:InP(111):B wafer was used as a substrate. The high roughness leads to small domains and a high mosaicity-tilt, but also strongly suppressed twinning of 28% due to many steps on the surface. The mosaicity-twist is only 1.0° due to the small lattice mismatch between layer and substrate.

These results show that long-range order and large domains are best realized on 10 mins at 700°C annealed substrates, likely due to a regular step pattern, favoring alignment of the layer to the surface plane. On rough Fe:InP(111):B substrates strong twin suppression can be realized due to a rough surface with many steps, which seem, however, to break the long-range order.

5.2 Analysis of Sb_2Te_3 films

Sb_2Te_3 is a topological insulator with a band gap of 0.28 eV hosting topological surface states with the Dirac point within the gap.[TSS+03] Sb_2Te_3 is also a natural p-type conductor, with the Fermi energy within the valence band. This is due to the formation of Sb_{Te} antisite defects, which act as electron acceptors.[JSC+12] The Fermi energy can be shifted up into the band gap to realize a fully insulating bulk by suppressing or compensating the p-type defects. One way to do this is by mixing the p-type Sb_2Te_3 with n-type Bi_2Te_3, whose more ionic bonds help suppress the Sb_{Te} antisite defects.[SHSS88, HvK86] Additionally, it has been shown that Sb_2Te_3 doped with transition metals exhibits ferromagnetism with large coercive fields and high Curie temperatures.[DHLcvU02, ZCU06] These properties allow the magnetically doped alloy of Sb_2Te_3 and Bi_2Te_3 to host the QAHE.[CZF+13]
In this chapter, pure Sb_2Te_3 is studied to better understand its growth properties and its potential influence on the growth of the mixed alloy.

The Sb_2Te_3 layers are grown by MBE on Si(111) substrates, which were dipped in 50% HF solution prior to growth to remove the oxide and create an H passivated surface. Thermal effusion cells are used to provide an Sb BEP of 3.6×10^{-7} mbar at a cell temperature of $T_{Sb} = 429°C$ and a Te BEP of 1.3×10^{-6} mbar at $T_{Te} = 360°C$, similar to the Bi_2Te_3 growth. These BEPs were offered for one hour of growth time. The constant group-VI (Te) to group-V (Sb) BEP ratio of about 4 is significantly decreased compared to Bi_2Te_3 due to the much higher Sb BEP necessary to reach similar growth rates. This may be caused by high desorption rates and the lower conversion factor from BEP to atomic flux of Sb. Furthermore, such a low Te overpressure is known to prevent Te_{Sb} antisite defects enhancing the quality of the layer.[JSC+12]

It is expected that the Sb flux at these cell temperatures contains mainly Sb_4 molecules. Growth may require a pairwise dissociation process similar to As_4, where two As_4 molecules dissociate and half of the As atoms get incorporated into the layer, while the rest leaves the surface.[JB93, JF75, TNA+97] This could lead to a larger migration length since the molecules have to interact to dissociate or a small migration length due to the relatively high mass of the molecules.

Fig. 5.9 shows a wide range $2\theta - \theta$ XRD scan of a representative 44 nm Sb_2Te_3 sample. All $00\underline{3n}$ reflections with $n \in \mathbb{N}$ are present as well as the Si 111 and 222 reflections from the substrate, confirming the nearly parallel alignment of the respective layer and substrate planes.

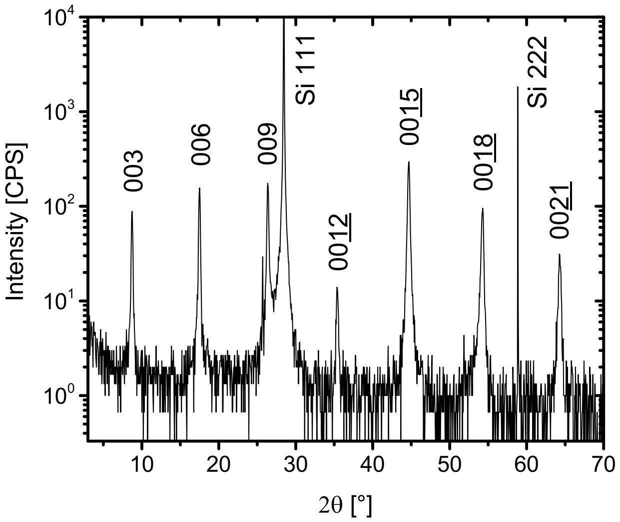

Fig. 5.9: Representative $2\theta - \theta$ XRD scan of a 44 nm thick Sb_2Te_3 sample grown on a Si(111) substrate.

The out-of-plane and in-plane lattice constants c and a were determined by XRD measurements of the 006 and 015 reflections using equation 4.6. The averaged values over all layers for c and a are 30.38 Å and 4.274 Å with standard deviations of 0.02 Å and 0.002 Å, respectively. There is no dependence on employed growth parameters in the studied range. These results are close to the published values of MBE grown layers $c = 30.43$ Å and $a = 4.28$ Å from [LKK+16] and $a = 4.26$ Å from [WZW+10]. Slight deviations can be caused by differing point defect concentrations depending on growth conditions.

During growth, RHEED showed a streaky pattern with additional rings, indicating polycrystalline contributions. In XRD, which in contrast to RHEED is not a surface sensitive technique, no additional peaks of randomly orientated domains were observed, though. This may indicate that some polycrystalline parts formed on top of the layer. Additionally, streaks originating from the substrate were visible during the whole growth. The layers do not seem to cover the substrate completely despite significant material deposition.

Next, the individual samples and their properties are discussed in dependence of the employed growth parameters. A series of four samples was grown at T_{Sub}=200°C, 215°C, 230°C and 245°C. At T_{Sub}=245°C no growth was observed in RHEED. Furthermore, two samples were grown at 230°C at half and double the Sb and Te fluxes with the growth time adjusted to keep the amount of offered material constant. Lastly, a sample grown at 200°C was post-growth annealed under Te atmosphere at 245°C for 30 mins after growth.

First, the surface of the samples is investigated by analyzing $4 \times 4\,\mu m^2$ AFM images shown in Fig. 5.10. Instead of closed layers, high islands are observed on the surface causing a very high RMS roughness above 10 nm for all samples. Scanning such islands deteriorates the tip quality quickly causing broadening of small islands and visible tip convolution artifacts after the first image. The general topography and the height of the islands can still be analyzed, though.

The sample grown at 200°C (Fig. 5.10 (a)) shows many small islands of about 20 nm height and 200 nm diameter on top of larger, flat islands of about 500 nm diameter. The small islands could be randomly oriented domains causing the rings observed in RHEED. A higher T_{Sub} of 215°C (Fig. 5.10 (b)) results in a similar surface morphology with small islands on top of large flat islands. The apparent increase in island size and the lower islands density is likely a result of a broader AFM tip causing tip convolution artifacts. At 230°C (Fig. 5.10 (c)), flat, mostly hexagonal islands with a diameter of 200-1000 nm and a height of about 20 nm are observed, covering about half of the substrate surface. The hexagonal form of the islands suggests growth in additional lateral directions compared to the typically triangular Bi_2Te_3 and Bi_2Se_3. The surface of the islands is partially atomically flat, likely due to a high migration length, which could be caused by the previously suggested two particle dissociation process. The observed islands seem similar to the larger islands covered by smaller islands at lower T_{Sub}. The lower surface coverage is consistent with RHEED showing substrate streaks even after growth. The growth of separated islands is probably caused by a low sticking coefficient of Sb on Si leading to only few nucleation sites. A higher Sb sticking coefficient on Sb_2Te_3 enables the growth of large islands around a nucleation site. Such properties were already observed for Sb_2Te_3 on graphene.[JSC+12]

A quantitative analysis of the desorption behavior in dependence of the substrate temperature analog to Bi_2Te_3 was not possible here, due to the layers not being closed. The large roughness prevented XRR measurements of the layer thickness and an estimate of the deposited material volume based on the height of the islands and the surface coverage would be inaccurate. Compared to Bi_2Te_3, which showed no desorption at 260°C, Sb_2Te_3 desorbs at much lower T_{Sub} with no observable growth at 245°C. Furthermore, a constant growth rate can not describe the entire growth due to the differing Sb sticking coefficients on Si and Sb_2Te_3. Thus, the desorption rate changes depending on the surface coverage with Sb_2Te_3 and will decrease with increasing island size during growth.

The sample grown at 230°C with half of the fluxes and double the growth time

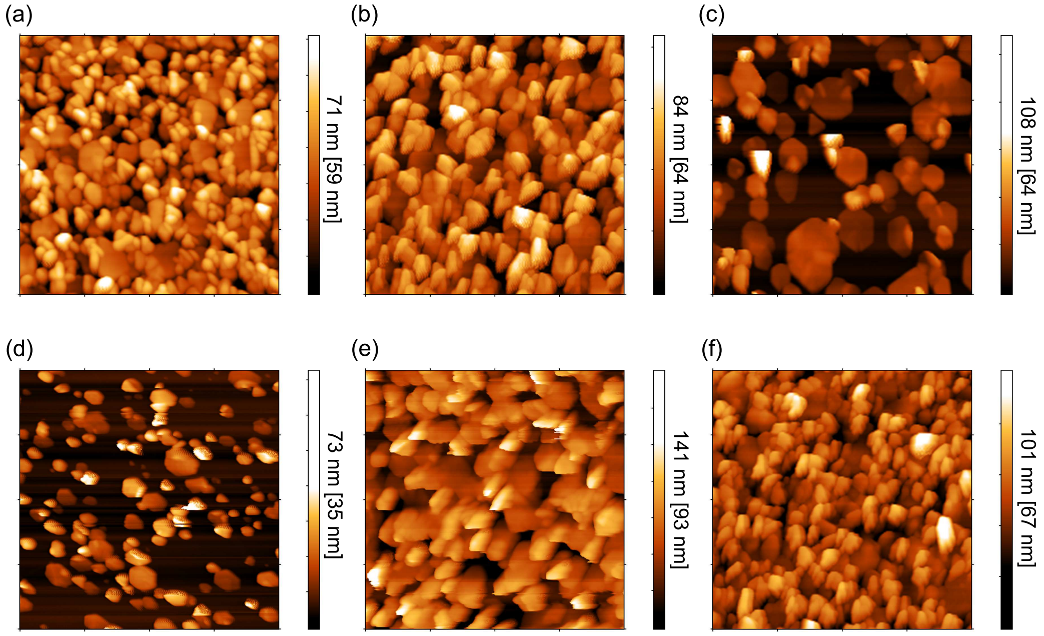

Fig. 5.10: 4×4 µm^2 AFM images showing the surface of the layers grown at (a) 200°C, (b) 215°C and (c) 230°C. Samples grown at 230°C with (d) half and (e) double the BEPs and (f) a sample grown at 200°C and annealed at 245°C for 30 mins are shown respectively.

(Fig. 5.10 (d)) shows more and smaller islands of similar height compared to the sample grown with standard fluxes. Overall the deposited material volume is clearly reduced. Doubling the fluxes while reducing the growth time by 1/2 produces more and higher islands covering nearly the entire substrate (Fig. 5.10 (e)). The amount of material offered was kept constant, but spread over a shorter time frame. This apparently increases material adsorption and reduced desorption. The observed behavior is qualitatively similar to the results for Bi_2Te_3 at 300°C in the last chapter. A simple explanation is that for longer growth times the sample stays longer at elevated temperatures, which causes more desorption. For Sb_2Te_3, a two-particle incorporation process would also introduce an overproportional, quadratic relation between incorporated Sb atoms and offered flux since the probability of Sb_4 to interact with another Sb_4 molecule depends on the flux as well.[JF75]

The annealed sample grown at 200°C (Fig. 5.10 (f)) shows a surface similar to the not annealed sample (Fig. 5.10 (a)) with slightly broader islands, likely caused by tip convolution artifacts. The average crystallite height determined by Scherrer analysis of the width of the 006 diffraction peaks using equation 4.7 increases from 31 nm for the not annealed sample to 44 nm for the annealed sample. During the annealing only Te overpressure was supplied to avoid desorption and no additional material deposition is expected. It is likely that the increased crystallite height is due to the merging of crystallites or the redistribution of material from the smaller islands on the top to the larger islands at the bottom.

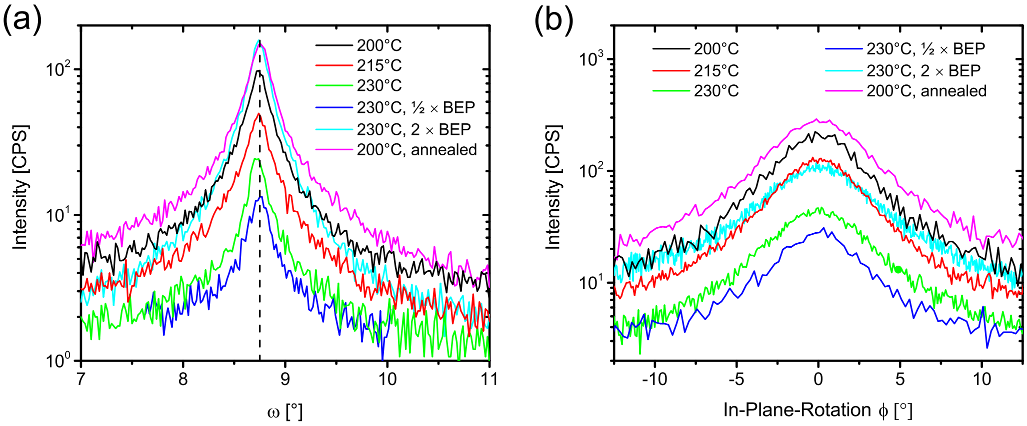

Fig. 5.11: (a) Rocking curve scans of the Sb_2Te_3 samples grown as indicated in the legend. The dashed line represents the angle parallel to the (111) substrate planes. (b) shows the in-plane rotation diffractogram of a (015) plane of the same samples with the maximum shifted to zero.

In Fig. 5.11 (a), XRD rocking curve scans of the Sb_2Te_3 samples are shown. The dashed line indicates the angle parallel to the (111) substrate planes. All Sb_2Te_3 samples have (00n) layer planes well oriented to the (111) substrate planes and show similar FWHM. A broad diffuse peak and no sharp Bragg peak is observed. The formation of individual islands observed in AFM likely reduces coherent x-ray diffraction between the domains suppressing long-range order. The FWHM of samples grown at 230°C were 0.26°, 0.24° and 0.25° for half, standard and doubled fluxes, respectively. For the annealed and not annealed samples grown at 200°C a slightly larger FWHM of 0.29° is observed in both cases. Growth at 215°C yields 0.32°. The slight reduction of the FWHM at 230°C is likely due to a larger migration length, which can decrease the mosaicity-tilt and increase the lateral crystallite size. Neither the growth rate nor annealing seem to influence the mosaicity-tilt. Overall, Sb_2Te_3 shows significantly reduced FWHM compared to 0.5° of the diffuse peak of Bi_2Te_3 at 220°C, indicating larger crystallites or less mosaicity-tilt.

Fig. 5.11 (b) shows in-plane rotation scans of the (015) peak of the samples. The FWHM fluctuate around $(6.0 \pm 0.5)°$ independently of growth parameters. This reflects an increase in mosaicity-twist compared to Bi_2Te_3 by about a factor of 2.

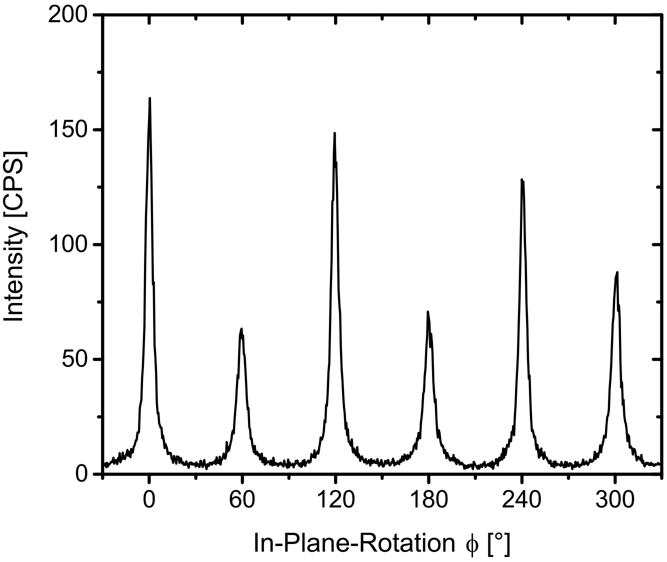

Fig. 5.12: Representative 360° in-plane rotation diffractogram of the {015} planes of an Sb_2Te_3 sample grown at 215°C.

Fig. 5.12 shows a representative 360° in-plane rotation scan of the {015} peaks of the sample grown at 215°C. The twinning, quantified as the integrated intensity ratio of minority twins to majority twins, is slightly suppressed to 67%. All the Sb_2Te_3 samples show similar results independent of growth conditions. The rather low twin suppression, high mosaicity-twist as well as the independence on growth conditions differ from the observations on Bi_2Te_3. A possible explanation is the deterioration of the interface to the substrate due to Sb interdiffusion and formation of Te-rich Sb_xTe_y phases at the interface decoupling the layer from the substrate as observed in [LKK+16].

In conclusion, the nucleation of Sb_2Te_3 on Si was found to be challenging and only possible for substrate temperatures of 230°C or lower and high Sb fluxes. AFM images show large separated islands just partially covering the substrate surface. This suggests a lack of nucleation sites due to a low sticking coefficient of Sb on Si and a higher sticking coefficient on Sb_2Te_3, similar to previous observations on graphene.[JSC+12]

Polycrystalline contributions were observed in RHEED, possibly due to randomly oriented smaller islands on the layer surface. No narrow coherent peak indicating long-range order was observed in XRD, but a significantly smaller mosaicity-tilt of 0.25° compared to Bi_2Te_3. All samples show a large mosaicity-twist of around 6° and partially suppressed twinning of around 67%. This relatively high rota-

tional disorder may result from a decoupling of the layer from the substrate. Such decoupling could be caused by the formation of Te rich Sb_xTe_y phases, due to the difficult nucleation as it was observed in [LKK+16].
Homogeneous nucleation was previously achieved on graphene by depositing few QLs at low temperatures before continuing growth at high temperatures.[JSC+12] Such a low temperature step will decrease the quality of the subsequent layer considerably, though. Given that in the previous chapter Bi_2Te_3 showed no difficulties nucleating on Si, alloying Sb_2Te_3 with Bi_2Te_3 might also lead to efficient nucleation as small clusters of Bi_2Te_3 can act as nucleation site for the $(Bi,Sb)_2Te_3$ layer.

6 Epitaxy and characterization of $(V,Bi,Sb)_2Te_3$ films

After studying Bi_2Te_3 and Sb_2Te_3 in the previous chapter, the focus of this chapter is on the mixed alloy $(V,Bi,Sb)_2Te_3$. Parts of this chapter are published in [WSG$^+$17]. By combining the n-type Bi_2Te_3 and the p-type Sb_2Te_3 charged point defects can be compensated and the Fermi energy shifted into the bulk gap to realize a fully insulating bulk.[ZCZ$^+$11] The higher bond polarity of Bi also reduces the point defects of Sb_2Te_3 significantly.[SHSS88] Doping the layers with Vanadium atoms can introduce ferromagnetism into the layer. Thin films of this alloy have the potential to host the QAHE, but perfect quantization is observed only in layers with specific thickness, composition and optimized growth conditions.[GSW$^+$15, CZK$^+$15b, CZK$^+$15a, GFS$^+$17a] Precisely controlled MBE growth and well optimized layers are thus necessary to realize the QAHE.

While the Bi/Sb ratio is mainly used to control the Fermi level, the substrate temperature has various influences. Low substrate temperatures should reduce Te vacancies, Bi_{Te} and Sb_{Te} antisite defects and lead to homogeneous V incorporation without V-rich clusters.

In this chapter, the nucleation of the mixed alloy will be analyzed to determine if the addition of Bi or V to Sb_2Te_3 can facilitate the nucleation on the Si substrate. In the subchapters 6.1 and 6.2, the structural and magnetotransport properties of the layers are investigated depending on the substrate temperature during growth and the Sb content. The influence of the Vanadium content will be studied in detail in chapter 8.

If not noted differently, all $(V,Bi,Sb)_2Te_3$ layers were grown directly on HF dipped Si(111) wafers without annealing prior to growth. Layers for magneto-transport measurements were always capped *in-situ* at about $T_{Sub} = 20°C$ with a partially crystalline 10 nm thick Te layer before defining a Hall bar by optical lithography. All layers show a streaky RHEED pattern during growth suggesting smooth layers

and XRD scans show parallel alignment of the (00n) planes of the $(V,Bi,Sb)_2Te_3$ layers to the (111) substrate planes without additional phases.
The layer thickness was determined by XRR measurements. For layers above 40 nm thickness, EDX measurements were used to determine the V content directly and serve as a calibration for thinner layers. For thin samples grown with the same V flux (source temperature) the V content can be deduced by accounting for a possibly different growth rate. The Sb content of the layers was determined based on XRD measurements of the in-plane lattice constant a as described in subchapter 6.2.

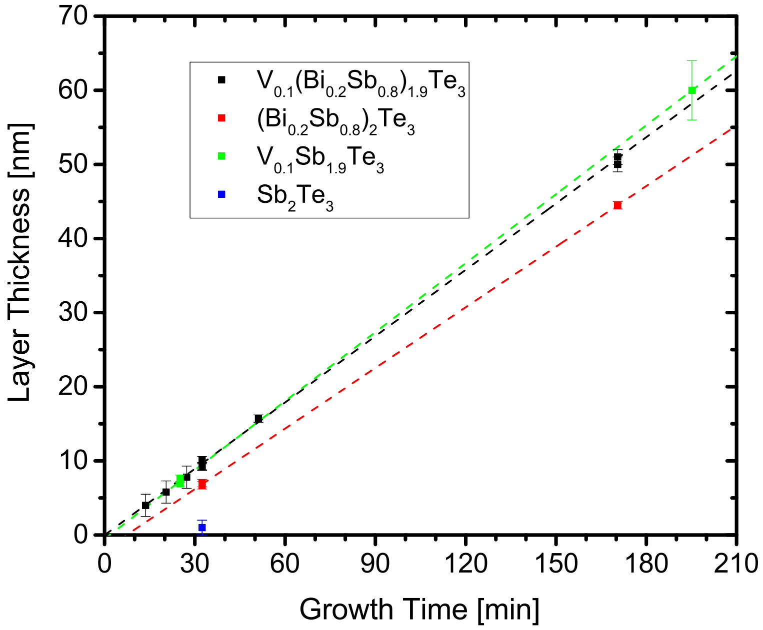

Fig. 6.1: The resulting layer thickness for different growth times distinguished between compounds by color. The individual samples of each compound are grown with the same fluxes. Linear fits shown as dashed lines reveal deviations from the expected direct proportionality as offset on the x-axis.

Fig. 6.1 shows the thickness of layers of four different compounds grown for different growth times. All layers were grown at $T_{Sub} = 190°C$. The samples of each individual compound were grown with the same fluxes, thus direct proportionality between layer thickness and growth time is expected. Deviations can occur due to a lower sticking coefficient on the substrate resulting in a delayed nucleation process. In chapter 5.2, it was observed that Sb_2Te_3 does not nucleate at elevated substrate temperatures and low fluxes. Here, an about 5× lower Sb and Te flux was employed at a slightly lower substrate temperature of 190°C. No nucleation was observed in RHEED after 32 mins of deposition. Small amounts of Sb_2Te_3 below a layer thickness of 2 nm can not be ruled out, though. For $(Bi_{0.2}Sb_{0.8})_2Te_3$ layers nucleation is possible, but seems to be delayed. The x-axis intercept suggests that desorption during the initial nucleation process delays the growth by about 7 mins. For $V_{0.1}(Bi_{0.2}Sb_{0.8})_{1.9}Te_3$ layers grown with the same growth conditions but with additional V, no such deviations are observed. This indicates that V and Bi together provide enough nucleation centers for Sb_2Te_3, enabling efficient nucleation with negligible desorption. $V_{0.1}Sb_{1.9}Te_3$ was grown with slightly increased Sb flux to compensate for the missing Bi. The high roughness of the thicker layer lead to a significant error for the layer thickness. While the linear fit suggests nucleation without desorption, a delay of up to 6 mins is possible within the error.

Comparing the $(Bi_{0.2}Sb_{0.8})_2Te_3$ and $V_{0.1}Sb_{1.9}Te_3$ layers, the Bi concentration in the former was 4× the V concentration of the latter, but it took longer to nucleate. Thus, V seems to be significantly more efficient in preventing desorption of Sb during the nucleation than Bi.

These results confirm that Sb_2Te_3 has a lower sticking coefficient on Si than on Sb_2Te_3. No Sb_2Te_3 growth is observed for low fluxes at 190°C. For such growth conditions it is apparently necessary to add Bi or V to enable the nucleation on Si. For $(Bi_{0.2}Sb_{0.8})_2Te_3$ a delayed nucleation is observed, which may result in an Sb deficiency at the interface. With the addition of both V and Bi, efficient nucleation without desorption was observed, which results in a well controlled layer thickness and homogeneous composition of $(V,Bi,Sb)_2Te_3$ layers at 190°C.

6.1 Influence of the substrate temperature

Having established that $(V,Bi,Sb)_2Te_3$ layers grow with a constant growth rate without delay during the nucleation at $T_{Sub} = 190°\mathrm{C}$, the T_{Sub} dependence of this growth rate can be studied in detail.

In Fig. 6.2 the growth rate (black rectangles) and the Sb content x (red circles) of thin $V_z(Bi_{1-x}Sb_x)_{2-z}Te_3$ layers below 18 nm thickness is shown as a function of T_{Sub} for standard growth conditions (full symbols) and for doubled Bi, Sb and Te BEPs (open symbols). For the standard conditions, cell temperatures of $T_{Bi} = 587°\mathrm{C}$, $T_{Sb} = 377°\mathrm{C}$, $T_{Te} = 319°\mathrm{C}$ and $T_V = 1400°\mathrm{C}$ were

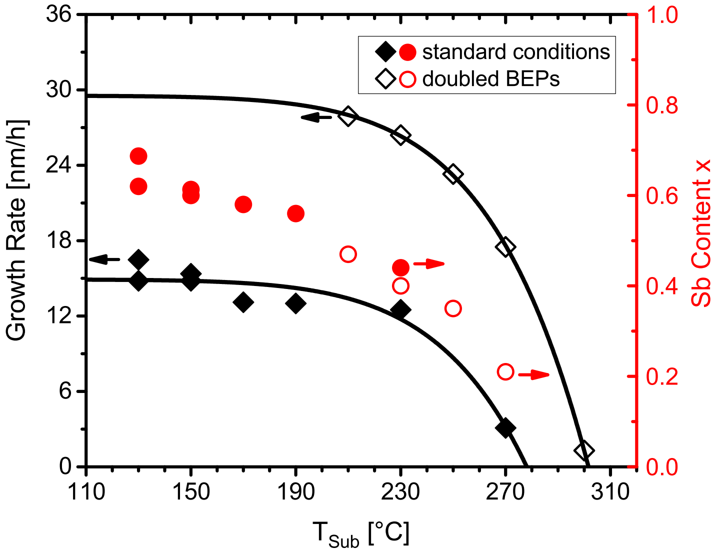

Fig. 6.2: The growth rate (black) of $(V,Bi,Sb)_2Te_3$ layers and their Sb content x (red) in dependence of the substrate temperature T_{Sub} for standard conditions (full symbols) and doubled BEPs (empty symbols).[WSG+17] (© 2017 American Physical Society)

used and resulted in $BEP_{Bi} = 1.4 \times 10^{-8}$ mbar, $BEP_{Sb} = 3.2 \times 10^{-8}$ mbar and $BEP_{Te} = 2.7 \times 10^{-7}$ mbar. For the low Vanadium flux, the BEP can not be measured. The group-VI to group-V BEP ratio of about 6 was chosen similar to the previous Sb_2Te_3 growth.

For standard conditions, the growth rate (full black symbols) is nearly constant for T_{Sub} up to 190°C. The extrapolation for the doubled BEPs to lower T_{Sub} shows a constant, approximately doubled growth rate. This demonstrates the direct proportionality between flux and growth rate and the absence of thermal desorption of Sb and Bi in this regime.

The direct proportionality of growth rate and fluxes is maintained up to 230°C, where doubled fluxes still result in a doubled growth rate and samples with $\frac{1}{2}\times$ and $\frac{1}{4}\times$ the flux also follow the direct proportionality (not shown here). For T_{Sub} above 190°C, the Sb content x as well as the growth rate is decreasing, though. This suggests that with increasing temperature first primarily Sb is desorbing followed by Bi desorption until at 300°C both Bi and Sb desorb completely and only a thin, pure V_xTe_y layer is left, as confirmed by EDX measurements. Above 230°C, the growth rate is no longer proportional to the flux but decreases significantly more for lower fluxes. At 300°C an additional doubling of the fluxes is necessary to enable the growth of $(V,Bi,Sb)_2Te_3$ (not shown).

Using equation 4.1, the molecular Sb/Bi flux ratio can be calculated from the measured BEPs, cell temperatures and the masses and ionization efficiency of the assumed Bi_2 and Sb_4 molecular fluxes. Multiplying the molecular flux ratio with the ratio of adsorbed atoms per molecule yields the atomic flux ratio. The Sb/Bi content ratio agrees to within ±15% with the calculated Sb/Bi atomic flux ratio, assuming an Sb_4 dissociation process which leads to the adsorption of only half the offered Sb, as observed for As_4.[WDSW82, JB93, JF75] This supports that such a dissociation process is indeed occurring and explains why only half the offered Sb seems to incorporate even at reduced temperatures.

Thermal desorption should be avoided since controlling the composition and thickness of layers is difficult without the growth rate being direct proportional to the individual fluxes. Additionally, in the desorption regime small differences in T_{Sub} caused by different substrate holders lead to variations between nominally equivalent samples reducing reproducibility.

It should be noted, that the given T_{Sub} was monitored by a thermocouple on the backside of a PBN diffusor plate on which the 2-in. substrates were clamped. The effective temperature at the surface may be increased for example due to heat radiation from the 1400°C hot Vanadium cell.

For the optimization of layers for the QAHE, $T_{Sub} = 190°C$ was chosen as well as standard flux conditions to avoid thermal desorption while maintaining acceptable structural quality. This T_{Sub} allows systematic variations in composition to study the requirements for realizing the QAHE. Before varying the composition in chapter 6.2, the influence of the substrate temperature on the properties of the layers is studied in detail.

The surface morphology of a series of four 50 nm thick $V_{0.1}(Bi_{0.2}Sb_{0.8})_{1.9}Te_3$ samples grown at 190°C, 200°C, 210°C and 220°C as well as three about 9 nm thick samples of similar composition grown at 150°C, 190°C and 220°C is analyzed. EDX measurements of the 50 nm series with varied T_{Sub} show no sign of desorption, while the thinner layers show a small reduction of the Sb and Te signal at $T_{Sub} = 220°C$ of about 5%. The influence of this small change in composition on the surface morphology is negligible, it can thus be assumed that the observed differences are purely due to the influence of the substrate temperature.

Fig. 6.3 (a) and (b) shows $5\times5\,\mu m^2$ AFM surface images of the 50 nm thick $V_{0.1}(Bi_{0.2}Sb_{0.8})_{1.9}Te_3$ samples grown at $T_{Sub} = 190°C$ and $T_{Sub} = 220°C$, respectively. The first sample shows the typical triangular islands with a side length of about 150 nm, while the increased substrate temperature of the second sample causes a significant increase in island size, lower island heights and thus a reduction of the RMS roughness from 2.0 nm to 1.2 nm. The side length of the islands is

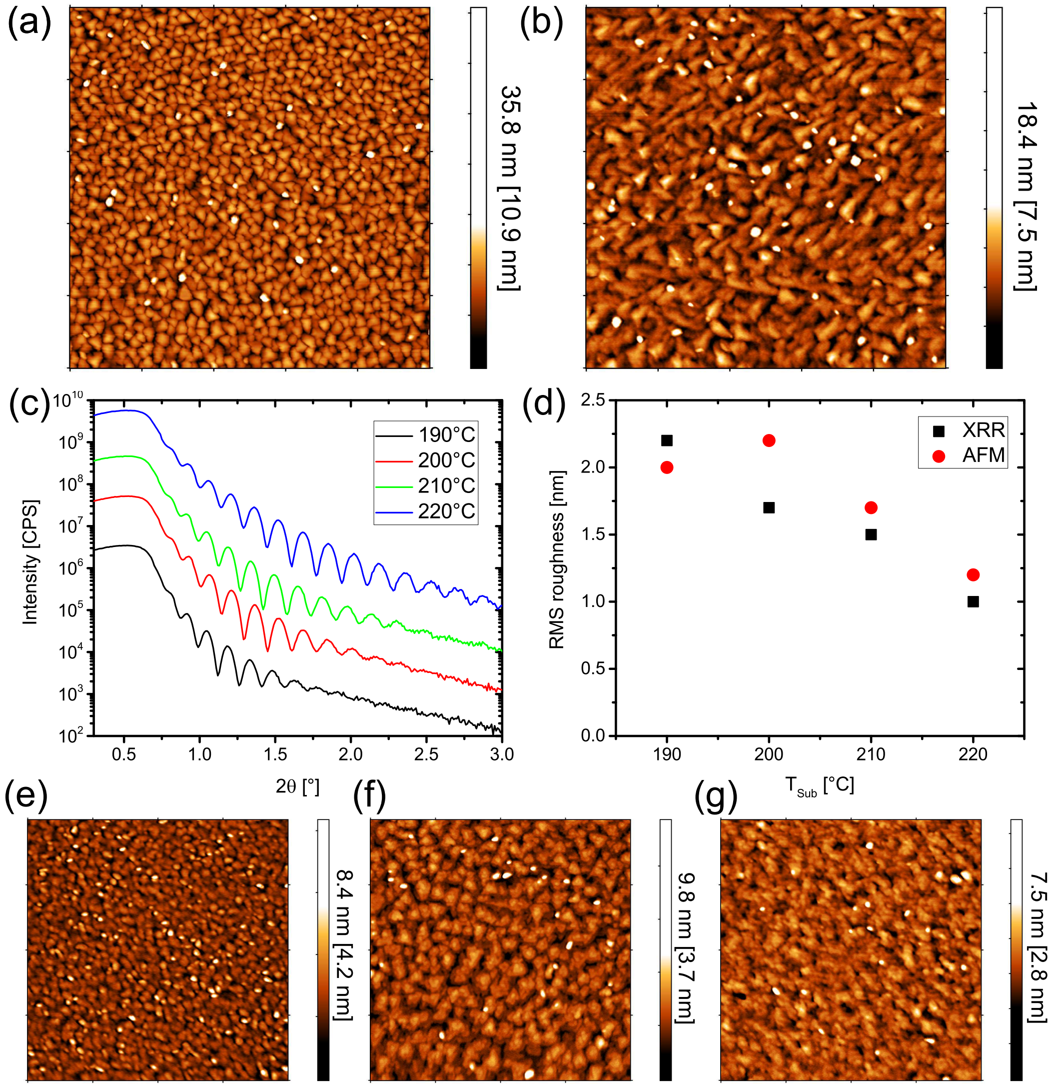

Fig. 6.3: 5×5 µm^2 AFM surface images of 50 nm thick V$_{0.1}$(Bi$_{0.2}$Sb$_{0.8}$)$_{1.9}$Te$_3$ samples grown at (a) T_{Sub} = 190°C and (b) T_{Sub} = 220°C. (c) XRR scans of the samples grown between 190°C and 220°C (offset by a factor of 10 each). (d) RMS surface roughness determined by XRR and AFM. 2×2 µm^2 AFM images of about 9 nm thick V$_{0.1}$(Bi$_{0.2}$Sb$_{0.8}$)$_{1.9}$Te$_3$ samples grown at (e) 150°C, (f) 190°C and (g) 220°C.

elongated to about 400 nm along one of two directions, which are 60° rotated toward each other. The samples grown at 200°C and 210°C show a similar trend. An unintentional miscut of about 0.6° was observed for the substrates likely causing jagged step edges alternating between two 60° rotated crystallographic directions. At elevated substrate temperatures the adatoms on the surface likely have enough energy to migrate longer distances along such step edges until an island is reached, where it is incorporated and elongates the island along the step edge. At lower substrate temperatures additional smaller islands will nucleate instead.

The RMS roughness determined by AFM of all four layers is shown in Fig. 6.3 (d) in red. XRR scans probing sample properties over a macroscopic scale of a few millimeters are shown in Fig. 6.3 (c). The higher the substrate temperature the more fringes are visible, indicating a smoothening of the surfaces. The RMS roughness quantified by fitting a simulation model to the experimental data is displayed in Fig. 6.3 (d) in black. Both techniques, AFM and XRR, give similar results and show a significant reduction of the RMS roughness for increased T_{Sub}, likely due to the increased migration length of the adatoms during growth.
Three thinner samples of about 9 nm thickness with the same composition were grown at substrate temperatures of 150°C, 190°C and 220°C. The resulting $2\times2\ \mu m^2$ AFM images are shown in Fig. 6.3 (e), (f) and (g), respectively. The determined RMS roughnesses are 0.7 nm, 0.6 nm and 0.5 nm, following the observed trend of decreasing roughness with increasing T_{Sub}. The island size is also increasing from about 70 nm side length at 150°C to about 150 nm side length at 190°C. At 220°C the islands are strongly interconnected, individual islands can no longer be distinguished. The observed trends of increasing island size and reduced roughness for higher substrate temperatures are consistent with results from the literature on pure $(Bi,Sb)_2Te_3$ [LES⁺15] and Cr-doped $(Bi,Sb)_2Te_3$ layers [TSD⁺17].

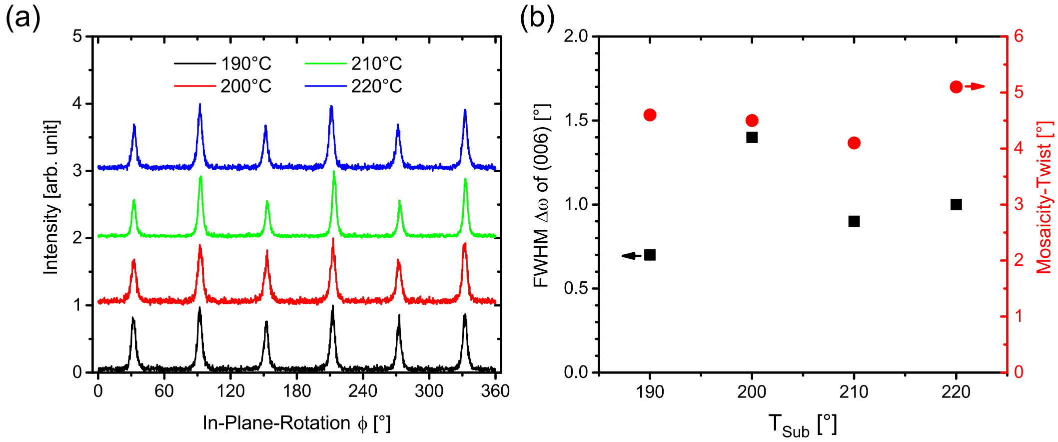

Fig. 6.4: (a) Normalized in-plane rotation diffractogram for $V_{0.1}(Bi_{0.2}Sb_{0.8})_{1.9}Te_3$ layers grown at varying T_{Sub} (offset by 1 each for clarity). (b) Rocking curve FWHM of the 006 reflection and in-plane rotation FWHM of the 015 reflection against T_{Sub}.

The influence of the substrate temperature on the crystalline quality is studied by XRD measurements of the 50 nm thick layers. In Fig. 6.4 (a) normalized 360° in-plane rotation diffractograms of the {015} planes are shown. The twinning, quantified by the ratio between the integrated peak intensities of the minority twin and the majority twin, amounts to 81%, 76%, 56% and 64% for T_{Sub} of 190°C, 200°C, 210°C and 220°C, respectively. A trend of reduced twinning with higher T_{Sub} is thus observed, with a small increase at 220°C likely due to fluctuations between individual samples.

At 200°C, the twinning is comparable to the 67% twinning in pure Sb_2Te_3, which did not exhibit further twin suppression at higher T_{Sub}, though. Bi_2Te_3 showed lower twinning at higher T_{Sub} with twinning as low as 32% at 300°C, which is likely caused by an enhanced migration length of the adatoms. At higher temperatures desorption of Sb and accumulation of Bi at the interface to the substrate may further reduce the twinning and lead to a behavior more similar to Bi_2Te_3.

The mosaicity-twist was determined from the FWHM of the peaks of the 015 reflection in the in-plane rotation scans and is shown in red in Fig. 6.4 (b). It fluctuates slightly about ±0.5° around 4.6° and shows no trend with the substrate temperature. The FWHM of the 006 reflection in rocking curve scans shown in black is a convolution of the mosaicity-tilt and broadening due to the finite lateral domain size. No trend is observed for the rocking curve FWHM of the (006) peak, which fluctuates strongly by ±0.4° around 1.0°. While no clear trends with T_{Sub} are observed, it can not be ruled out that the strong fluctuations hide the influence of the substrate temperature. In the literature, small improvements of the mosaicity-tilt with increased T_{Sub} were observed in $(Bi,Sb)_2Te_3$ [LES+15] and improved mosaicity-twist in Cr-doped $(Bi,Sb)_2Te_3$ [TSD+17].

Compared to the pure Sb_2Te_3 and Bi_2Te_3, the mosaicity-twist is in between the previously measured values and the rocking curve FWHM is significantly broader than for pure Bi_2Te_3 and Sb_2Te_3. The island size observed in AFM, and therefore the maximum lateral crystallite size, did not change significantly compared to the binary materials, which suggests that the broadening of the rocking curve FWHM is due to V doping increasing the mosaicity-tilt. This will be confirmed in the later chapter 8, in which the influence of V is studied in detail.

The average value of c and a is 30.40 Å and 4.288 Å with standard deviations of 0.01 Å and 0.002 Å, respectively. This fits to the expected values for this composition of the layers and the low deviations confirm the high reproducibility of the layers.

Before studying the influence of T_{Sub} on the lattice constant c, other influences on c have to be investigated first. The lattice constant c of above 50 nm thick $(V,Bi)_2Te_3$ layers of 30.33 Å and $(V,Sb)_2Te_3$ layers of 30.34 Å shows little difference. This is consistent with results from [SKS62], which shows a constant lattice constant c for alloys in the whole range from Bi_2Te_3 to Sb_2Te_3. The previously

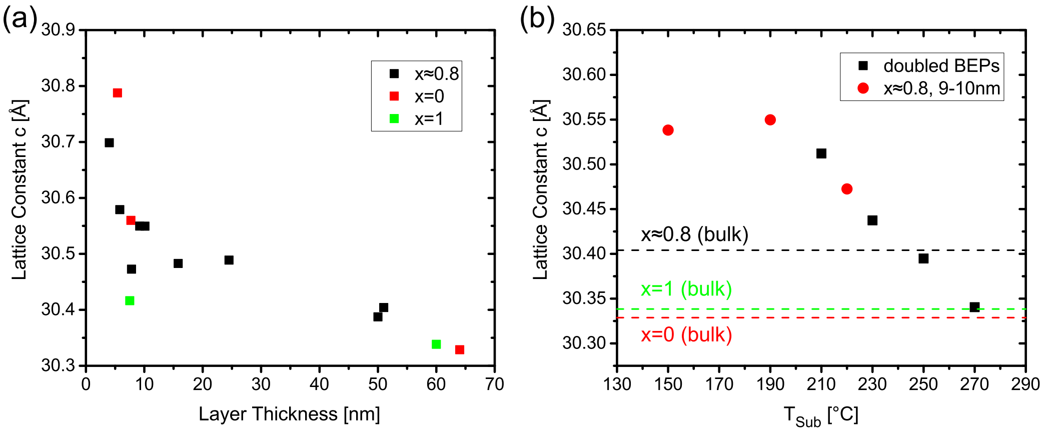

Fig. 6.5: (a) Lattice constant c of $V_{0.1}(Bi_{1-x}Sb_x)_{1.9}Te_3$ layers grown at T_{Sub} = 190°C depending on layer thickness for the Sb contents $x = 0$ (red), $x = 1$ (green) and $x \approx 0.8$ (black). (b) Lattice constant c as function of T_{Sub} for two sets of $(V,Bi,Sb)_2Te_3$ samples, Bi-rich doubled BEPs (black) and Sb-rich standard conditions (red).[WSG$^+$17] (© 2017 American Physical Society)

studied mixed $V_{0.1}(Bi_{0.2}Sb_{0.8})_{1.9}Te_3$ alloy shows an increased lattice constant of $c = 30.40$ Å, though, and thus deviates from Vegard's law and the results from [SKS62]. Various other samples with and without V show such a behavior. The deviation can be caused by point defect concentrations changing with composition and may be more pronounced at specific growth conditions. Due to the deviation from Vegard's law, c depends slightly on the composition, despite similar values for the two ternary compounds. Changing T_{Sub} can thus influence c due to desorption of Sb.

In Fig. 6.5 (a) the dependence of the lattice constant c on the layer thickness is shown for layers grown at 190°C for different Sb content $x = 0$ (red), 1 (green) and $x \approx 0.8$ (black). All compositions show consistently a significant increase of c up to about 0.4 Å for reduced layer thicknesses. It should be noted, that the lattice constant c was determined from the position of the 006 reflection, assuming a homogeneous lattice constant throughout the layer. It is possible that inhomogeneities at the interface, like other phases, a strained QL, an additional Te layer or absorbates may cause an apparent shift of the peak position due to a low intensity shoulder, which does not reflect the lattice constant of the whole layer. Thinner layers would become more sensitive to these inhomogeneities, which would explain the apparent change of c with decreasing layer thickness.

In Fig. 6.5 (b) the lattice constant c is shown against T_{Sub}. Only $(V,Bi,Sb)_2Te_3$ layers with a thickness between 9-18 nm are used to limit differences due to the previously discussed influence of the thickness. The samples with doubled BEPs used for the desorption curve are plotted in black and the samples used for the AFM analysis of thin layers are shown in red. A significant increase of the lattice constant c with decreasing T_{Sub} is observed until a saturation seems to be reached below 190°C. Both sets of samples seem to fit well together.

The increased lattice constant c is difficult to explain unambiguously due to the many potential influences. Higher T_{Sub} causes preferential Sb desorption and therefore increased Bi and V content as well as a decreased layer thickness, all of which can influence the lattice constant. The different growth conditions and compositions also influence point defect concentrations, which can modify the lattice constant as well. Remarkably, all the previously studied thicker Bi$_2$Te$_3$, Sb$_2$Te$_3$ and (V,Bi,Sb)$_2$Te$_3$ layers showed no influence of T_{Sub} on c, though. This may indicate that changes in point defect concentrations are not the cause. At a high T_{Sub} of about 270°C, the lattice constant of the thin Bi-rich (V,Bi,Sb)$_2$Te$_3$ layer is consistent with the value of the 64 nm thick (V,Bi)$_2$Te$_3$ sample. It seems that only thinner layers below 50 nm grown at reduced T_{Sub} show an increased lattice constant c, which increases further with decreasing thickness and T_{Sub}. The previously suggested inhomogeneities at the interface may form primarily at lower T_{Sub}, which would explain the observed behavior.

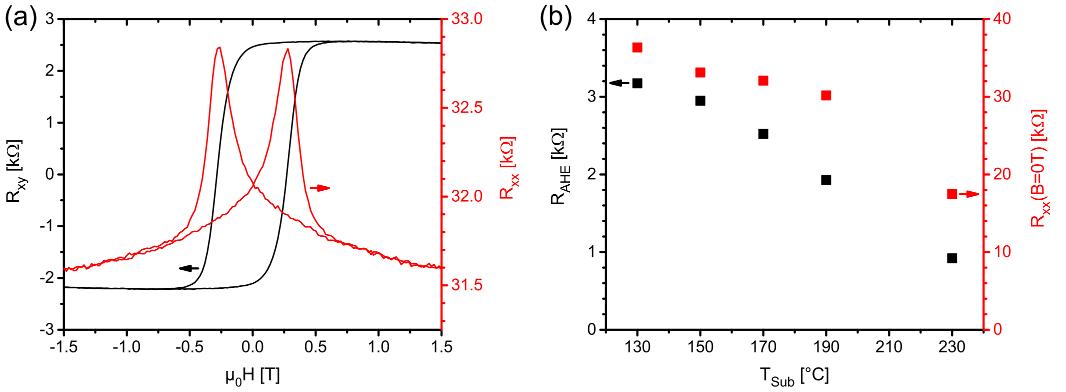

Fig. 6.6: (a) Hall resistance R_{xy} and longitudinal resistance R_{xx} of a sample grown at $T_{Sub} = 170$°C as a function of external magnetic field measured at the optimal gate voltage $V_G = 2.5\,\mathrm{V}$ and $T = 4\,\mathrm{K}$. (b) Anomalous Hall resistance R_{AHE} and longitudinal resistance R_{xx} at $H = 0$ of (V,Bi,Sb)$_2$Te$_3$ samples grown at differing T_{Sub} measured at applied optimal gate voltage and $T = 4\,\mathrm{K}$.

Lastly, the magneto-transport properties of (V,Bi,Sb)$_2$Te$_3$ layers are studied in dependence on T_{Sub}. Hall bars were patterned by optical lithography for a set of samples protected by a Te capping layer. The layers were about 9 nm thick and grown under standard conditions with the Sb content $x \approx 0.6$ and the V content $z \approx 0.1$. Substrate temperatures of 130°C, 150°C, 170°C, 190°C and 230°C were employed during growth. The Hall resistance R_{xy} and the longitudinal resistance R_{xx} were measured at $T = 4\,\mathrm{K}$ while sweeping an external magnetic field. Individual gate voltages V_G were applied to tune the Fermi level and increase R_{xy}. A maximum in R_{xy} was reached within the available range of V_G for all samples.

In Fig. 6.6 (a) a representative measurement of the layer grown at 170°C is shown with R_{xy} in black and R_{xx} in red with an applied $V_G = 2.5\,\mathrm{V}$ at $T = 4\,\mathrm{K}$. A hysteresis loop with an anomalous Hall contribution to R_{xy} is observed, indicating ferromagnetism due to V doping in the layers. Magnetic switching events are observed at a coercive field of 0.28 T for all samples. An anomalous Hall resistance R_{AHE} was extracted by extrapolating R_{xy} from high fields to zero and averaging over both sweep directions. The Hall slope at high fields indicate primarily n-type conduction. Fig. 6.6 (b) shows R_{AHE} (black) and R_{xx} at $H = 0$ (red) decreasing monotonically with increasing T_{Sub}.

Higher T_{Sub} can change many layer properties which potentially affect transport properties, like carrier mobility and carrier concentrations. The crystalline quality, domain sizes, homogeneity of magnetic doping and point defect concentrations directly depend on T_{Sub}. Changes in the composition and layer thickness due to desorption also influence these properties. A possible explanation for the reduced resistance is that Sb desorption causes less group-V on Te antisite defects, which act as electron acceptors. The electron concentration in the primarily n-type samples would thus increase further, resulting in a reduced resistance. The electron concentration could also be increased due to T_{Sub} directly affecting different point defect concentrations. These explanations are consistent with the observation in [SWM+18], that annealing $(\mathrm{Bi,Sb})_2\mathrm{Te}_3$ increases the electron concentration. It is also possible, that crystallographic disorder at lower T_{Sub} reduces the electron mobility leading to an increased resistance.

To summarize this chapter, it was shown that substrate temperatures above 190°C result in desorption of primarily Sb, reducing the thickness of the layers and increasing Bi and V concentrations. $T_{Sub} = 190°\mathrm{C}$ was established as a suitable growth temperature for well controlled growth, avoiding desorption without reducing the crystalline quality unnecessarily at lower temperatures.

AFM images of the surface of around 50 nm thick as well as about 9 nm thick layers

reveal a systematic increase of the island size with increasing substrate temperature as well as decreasing roughness. Consistent XRR data shows a smoothening of the layers as well.
Furthermore, XRD measurements of the thicker layers showed a trend of reduced twinning with increased substrate temperature, likely due to an increased migration length of the adatoms. The mosaicity-tilt and -twist seems to remain constant with relatively large fluctuations. The out-of-plane lattice constant c of layers below 50 nm thickness was shown to be sensitive to variations of the substrate temperature. The lower the thickness and the lower the substrate temperature the more the lattice constant c seems to increase. This apparent increase may be a result of inhomogeneities at the interface to the substrate, which may form especially at lower temperatures.
Finally, magneto-transport measurements reveal a decreasing anomalous Hall and longitudinal resistance with increasing substrate temperature. This may be due to an increasing electron carrier concentration caused by desorption of Sb. These results show that ferromagnetism and the anomalous Hall effect were successfully realized by doping the layers with V, but the resulting anomalous Hall resistance in these layers of $V_{0.1}(Bi_{0.4}Sb_{0.6})_{1.9}Te_3$ is far from the quantized value of the von Klitzing constant.

6.2 Influence of the Sb content

In this chapter, the influence of the Sb content of $(V,Bi,Sb)_2Te_3$ layers on structural and magneto-transport properties will be investigated. The main goal in this chapter is the realization of the QAHE. A necessary requirement for the observation of the QAHE is the tuning of the Fermi level into the band gap of the topological surface states caused by the magnetization.[CZF⁺13] This can be done by changing the Sb content of the layer and applying a gate voltage.[JSC⁺12] Previous results in the literature have shown that a specific Sb content is necessary to observe the QAHE.[CZK⁺15c]
The stable growth conditions developed in the last chapter are used to grow samples with differing Sb content x, while keeping layer thickness and V content nearly constant. The resulting structural changes will be investigated for $x = 0$, $x = 1$ and $x \approx 0.8$, which can host the QAHE. The in-plane lattice constant a is typically highly sensitive to the Sb content, which may enable the deduction of the

Sb content by XRD measurement even for thin layers. Finally, a series of about 9 nm thick samples with differing Sb content is examined in magneto-transport measurements to optimize the Sb content in regard to a high anomalous Hall resistance.

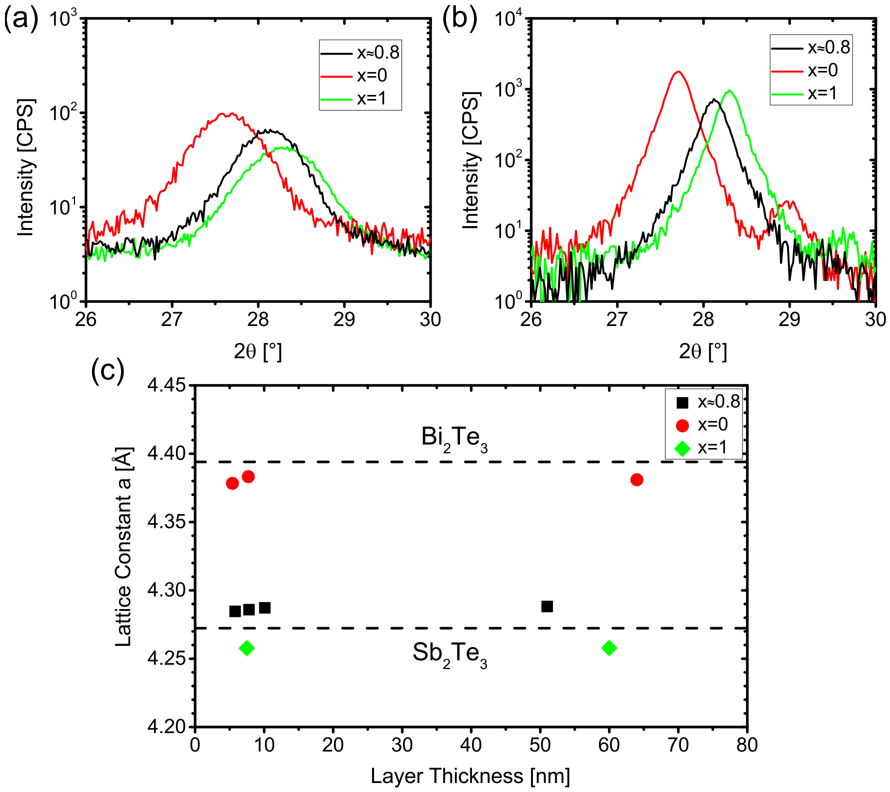

Fig. 6.7: $2\theta - \theta$ XRD scans of the 015 reflection of (a) about 9 nm thick and (b) 50-65 nm thick $V_{0.1}(Bi_{1-x}Sb_x)_{1.9}Te_3$ layers with $x = 0$ (red), $x = 1$ (green) and $x \approx 0.8$ (black). (c) Resulting in-plane lattice constant a for different layer thicknesses.

Fig. 6.7 (a) shows $2\theta - \theta$ XRD scans of the asymmetric 015 reflection of about 9 nm thick $V_{0.1}(Bi_{1-x}Sb_x)_{1.9}Te_3$ layers with $x = 0$ (red), $x = 1$ (green) and $x \approx 0.8$ (black). The peak position is used to calculate d_{015}. The in-plane lattice constant a is calculated by equation 4.6 with the known d_{015} and the lattice constant c determined from the 006 reflection. The alignment of ω and ψ for the $2\theta - \theta$ scan of the 006 reflection is done using the Si(111) substrate planes, which are typically parallel to the layer planes for these samples. For the asymmetric 015 reflection, ω and ψ are not aligned to the sample, while ϕ is aligned to the Si(004) planes whose rotational angle is transferred to the 015 planes of the layer. Given that c is nearly constant for different x, the change of a with Sb is reflected in the shift of the peak position of the 015 reflection. Even for thin layers the intensity and the shift of the peak position are sufficient to reliably determine a with an error of about ±0.005 Å. Even small differences in the Sb content thus create detectable shifts in a.

In Fig. 6.7 (b), scans of 50-65 nm thick layers of similar compositions as the thin layers show consistent peak positions. The extracted lattice constant a is plotted in Fig. 6.7 (c) against the layer thickness. In contrast to the lattice constant c, a does not seem to depend on the layer thickness. Strong chemical bonds within a QL may define a more rigorously compared to weak van der Waals bonds between QLs out-of-plane. These van der Waals bonds allow for more flexibility and can host intercalates within the gap. V doping seems to reduce a slightly, similar to the observed reduction of c, causing the discrepancy between the previously observed lattice constants for Bi$_2$Te$_3$ and Sb$_2$Te$_3$ (shown as dashed lines) and their V doped counterparts.

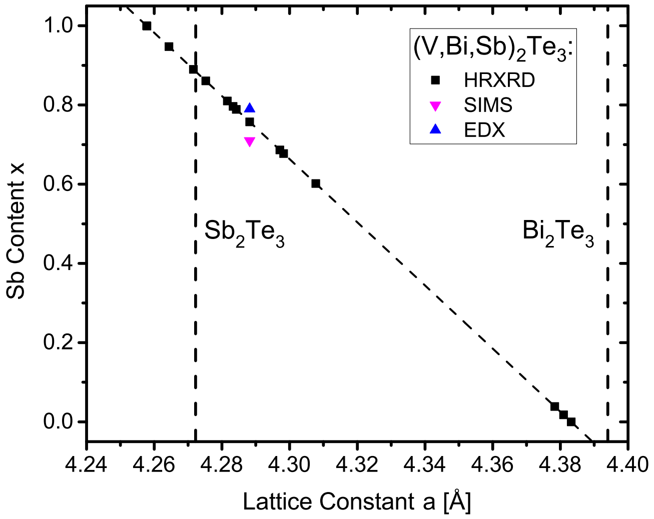

Fig. 6.8: Mapping of the measured lattice constant a to the Sb content x along the dashed diagonal line for a variety of layers of different thickness. Results of SIMS and EDX measurements of a 51 nm thick (V,Bi,Sb)$_2$Te$_3$ layer are shown as magenta and blue triangles, respectively. Additional dashed lines show the lattice constants of pure Sb$_2$Te$_3$ and Bi$_2$Te$_3$ as comparison.

The sensitivity of the lattice constant a on the substrate temperature is difficult to study in the mixed compounds since higher temperatures cause desorption and a change in composition, which also influences a. The binary compounds Sb$_2$Te$_3$ and Bi$_2$Te$_3$ never showed an influence of the substrate temperature on a. Thus a seems to be rather insensitive to the layer thickness and the substrate temperature, but sensitive to the Sb content x, which allow the determination of the latter.

Assuming a linear relation between a and x (Vegard's law), it is possible to deduce x from the measured a. The validity of Vegard's law was shown in [SKS62] for undoped layers. Thin $V_{0.1}Bi_{1.9}Te_3$ ($a = 4.383\,\text{Å}$) and $V_{0.1}Sb_{1.9}Te_3$ ($a = 4.258\,\text{Å}$) layers are used as calibration samples keeping parameters like thickness, substrate temperature and V content close to the layers to characterize. For layers with deviating V content, it is possible to subtract the influence of V using the results of chapter 8. To estimate the error of this method, the Sb content of the 51 nm thick $(V,Bi,Sb)_2Te_3$ layer was determined additionally by EDX and secondary ion mass spectrometry (SIMS) measurements. In Fig. 6.8 the calculation of x from a is illustrated and the slightly deviating results of the EDX ($x = 0.79$) and SIMS measurement ($x = 0.71$) from the XRD result ($x = 0.76$) are shown. The additional methods thus agree within ±0.05 with the XRD result, which can be used as an estimate of the error. Besides possible deviations from Vegard's law in the V doped layers, systematic errors can be caused by small misalignments of the instrument, the limited instrumental resolution and the measurement geometry used for asymmetric reflections which illuminates a large asymmetric area of the sample. Empirical tests show that errors due to misalignment in ω and ψ are well within the estimated error of 5%. Furthermore, such systematic errors are expected to affect the calibration samples similarly which limits their influence on the determination of the Sb content. Multiple measurements of the same sample after individual alignment typically yield highly reproducible results with deviations below ±0.01. The estimated error of 5% is mostly systematic and affects all layers similarly, which makes it possible to distinguish differences in x of about 0.02 even for thin layers.

Next, the influence of x on structural properties is investigated. Samples with a thickness of 9 nm and 50-65 nm with $x = 0$, $x = 1$ and $x \approx 0.8$ are studied.

In Fig. 6.9 (a), (b) and (c) $2{\times}2\,\mu\text{m}^2$ AFM images of the thicker layers with $x = 1$, $x \approx 0.8$ and $x = 0$ are shown, respectively. In contrast to the Sb_2Te_3 layers in previous chapters (see Fig. 5.10), the $V_{0.1}Sb_{1.9}Te_3$ layer shows a closed surface with triangular islands. $5{\times}5\,\mu\text{m}^2$ AFM images are used to determine the RMS roughness, which reduces from 3.2 nm to 2.0 nm with the addition of Bi ($x \approx 0.8$). Bi seems to decrease the height of the islands and increase their size slightly. The $V_{0.1}Bi_{1.9}Te_3$ layer exhibits much larger, flatter and more interconnected islands, without the typical triangular form resulting in a reduced RMS roughness of 1.0 nm.

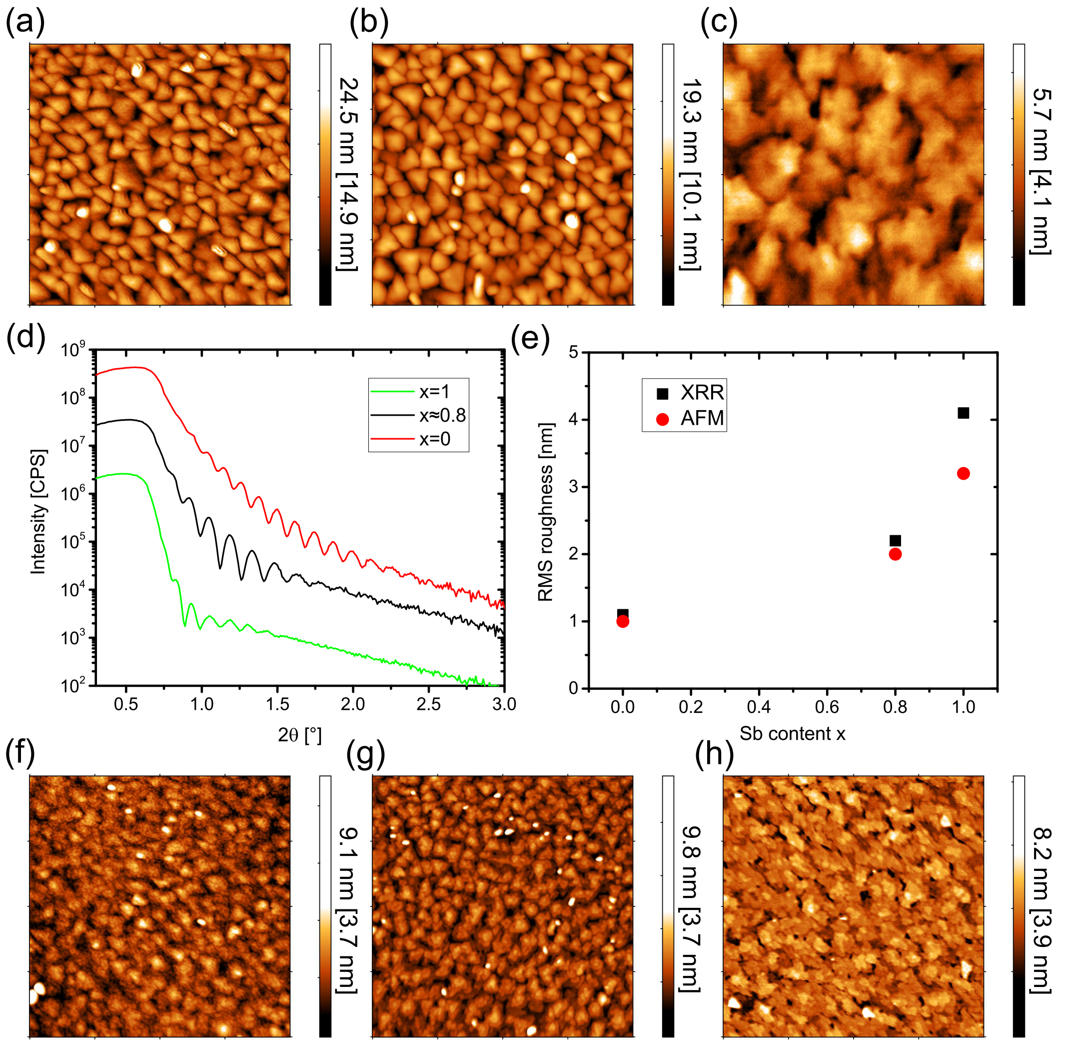

Fig. 6.9: 2×2 µm^2 AFM images of 50-65 nm thick V$_{0.1}$(Bi$_{1-x}$Sb$_x$)$_{1.9}$Te$_3$ layers with (a) $x = 1$, (b) $x \approx 0.8$ and (c) $x = 0$. (d) XRR scans of the same layers (offset by a factor of 10 each). (e) RMS surface roughness determined by XRR and AFM. 2×2 µm^2 AFM images of about 9 nm thick layers with (f) $x = 1$, (g) $x \approx 0.8$ and (h) $x = 0$.

In Fig. 6.9 (d), XRR scans of the same layers show progressively more fringes with increasing Bi content in the layer. In Fig. 6.9 (e) the extracted RMS roughness values from the XRR scans are shown in black and from the AFM images in red. Both techniques show consistently a significant reduction of the surface roughness with increasing Bi content. The reason could be the improved nucleation with more nucleation sites due to the Bi alloying leading to a more homogeneous growth. Other explanations include a higher reactivity or mobility of the adsorbed Bi at the surface, both could lead to a smoother surface.

In Fig. 6.9 (f), (g) and (h), 2×2 µm^2 AFM images of the thinner layers with $x = 1$, $x \approx 0.8$ and $x = 0$ are shown, respectively. Similar to the thicker layers, the addition of Bi seems to lead to bigger, more interconnected islands, while the RMS roughness stays nearly constant at 0.8 nm ($x = 1$), 0.6 nm ($x \approx 0.8$) and 0.7 nm ($x = 0$).

The layers were further characterized by XRD measurements. All samples show a rocking curve FWHM of the 006 reflection of about 0.9° with no clear trend with the composition or thickness. Similarly, the mosaicity-twist amounts to 4-5° for all layers without any trends. Neither $V_{0.1}Bi_{1.9}Te_3$ nor $V_{0.1}Sb_{1.9}Te_3$ shows improvements compared to the previously observed twinning of 81% in the mixed compound at 190°C.

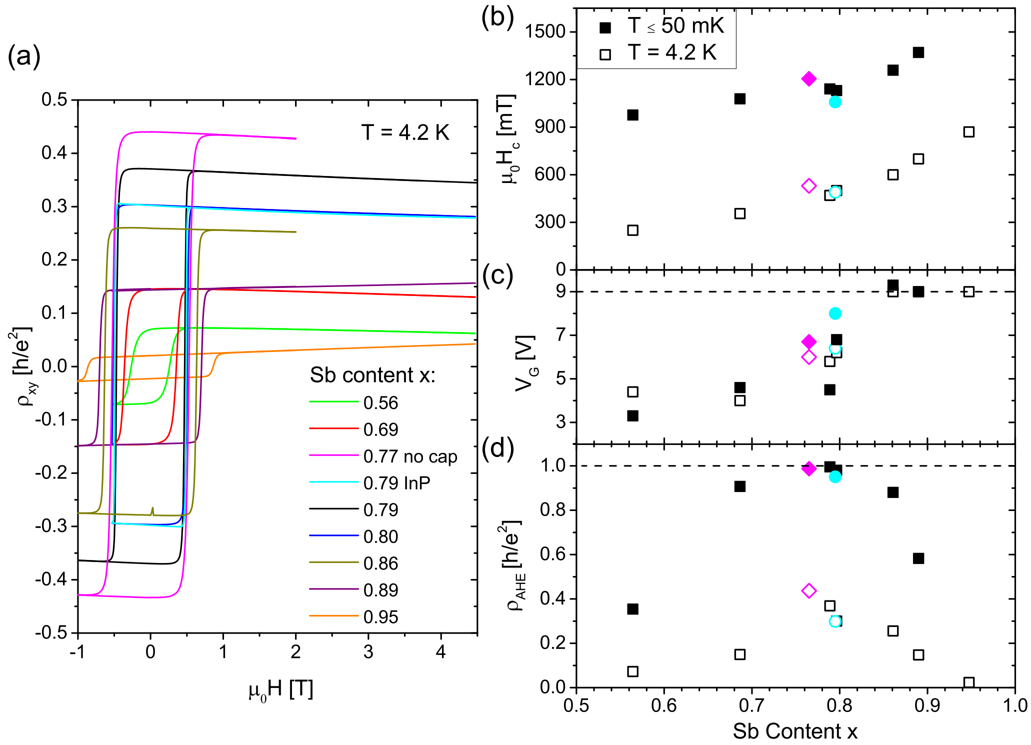

Fig. 6.10: (a) Hall resistivity ρ_{xy} at 4.2 K with applied gate voltage V_G for different Sb content x against the applied external magnetic field. (b) coercive field $\mu_0 H_c$, (c) the individually applied V_G for maximal Hall resistivity up to the limit of 9 V and (d) the anomalous Hall resistivity ρ_{AHE} at V_G against the Sb content x of individual layers. Measurements at 4.2 K are shown as empty symbols and below 50 mK as full symbols. A layer without Te cap is marked as magenta diagonal box and a layer on InP substrate as cyan circle.[WSG+17] (© 2017 American Physical Society)

Finally, magneto-transport measurements were conducted on an additional set of about 9 nm thick $V_{0.1}(Bi_{1-x}Sb_x)_{1.9}Te_3$ layers with x varied between 0.56 and 0.95. One sample without Te cap and one sample on an InP substrate are included in the data, but will be discussed in detail in the next chapter. In Fig. 6.10 (a) the Hall resistivity ρ_{xy} is shown for increasing and decreasing external magnetic fields applied perpendicular to the surface. The measurements were conducted at 4.2 K with an individually applied gate voltage V_G shown in (c) as empty symbols.

The sign of the slope at high magnetic fields indicates the dominant carrier type. For x up to 0.86 the slope is negative corresponding to primarily n-type conduction. For $x = 0.86$ a negative slope is observed for positive V_G and for a negative $V_G = -6\,\mathrm{V}$ the sign of the slope reverses. For x above 0.86 all layers showed a positive slope indicating primarily p-type conduction. Such a behavior is expected, since Bi_2Te_3 is known to be n-type due to intrinsic point defects like Te_{Bi} antisites and Sb_2Te_3 p-type due to Sb vacancies and Sb_{Te} antisites. By mixing these materials it is apparently possible to suppress and compensate the defects such that the tuned gate voltage is enough to switch the dominant carrier type at $x = 0.86$. The Fermi level is thus deep in the bulk band gap, probably close to the Dirac point.

It is likely that multiple carrier types are present in the samples close to the charge neutral point due to carrier-density inhomogeneities and asymmetric gating of the top and bottom surfaces. The presence of multiple carriers, which can have significantly different mobilities, and a possible influence of the magnetic doping on the slope prevent the quantitative determination of carrier concentrations. The position of the charge neutral point can thus only be estimated to be around $x = 0.86$. Close to this Sb content, at $x = 0.77$, the maximum of the anomalous Hall resistivity of $\rho_{AHE} = 0.44\,h/e^2$ is observed. The lowered ρ_{AHE} at deviating Sb content is probably due to additional bulk conductance caused by remaining non-localized carriers. The highest observed ρ_{AHE} is still significantly lower than the von Klitzing constant, which suggests that even close to the charge neutral point $T = 4.2\,\mathrm{K}$ is not low enough to suppress parasitic bulk conductance completely. An additional detailed study was thus conducted at even lower temperatures below 50 mK in dilution refrigerators.

The resulting coercive field values at mK temperatures as well as at 4.2 K are shown in Fig. 6.10 (b) as full and empty symbols, respectively. A trend to higher fields with increasing Sb content is observed at both temperatures. Apparently, the Sb content influences the magnetic properties, which may be due to e.g. the double exchange interaction depending on the position of the Fermi level.[PBS+16] Lowering the temperature also increases the coercive field considerably.

Fig. 6.10 (c) shows the gate voltage V_G applied to maximize ρ_{AHE}. For a higher x, V_G tends to be higher as well, until at $x > 0.86$ the breakdown voltage of the gate of 9 V is reached. This trend is probably linked to the compensation of increasing p-type defects by the positive voltage. V_G seems mostly unaffected by the measurement temperature. In Fig. 6.10 (d) ρ_{AHE} shows a maximum around $x = 0.79$ for both measurement temperatures. The measurements necessary for the optimization of x can thus be conducted at 4.2 K. The measurements at mK show a significant increase of ρ_{AHE} and the QAHE is observed in layers with x in a narrow range of $0.76 - 0.79$. At $x = 0.86$ the maximum of ρ_{AHE} is still reached within the gate voltage range, but ρ_{AHE} is not fully quantized anymore. The decreasing ρ_{AHE} with increasing x is thus not due to the limitation in gate voltage. A possible explanation is that high gate voltages shift the Fermi level at the top of the layer significantly more than at the bottom leading to an inhomogeneous potential which is not fully inside the energy gap anymore.

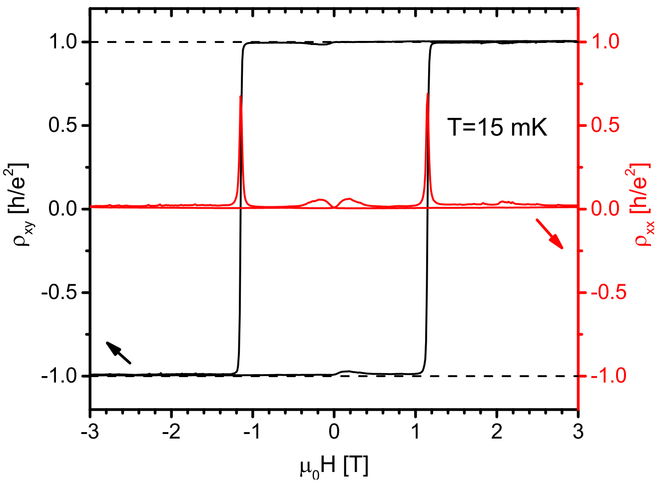

Fig. 6.11: Hall resistivity ρ_{xy} and longitudinal resistivity ρ_{xx} of the capped $V_{0.1}(Bi_{0.21}Sb_{0.79})_{1.9}Te_3$ layer on Si as a function of external magnetic field measured at $T = 15$ mK with applied $V_G = 4.5$ V.

The layer with $x = 0.79$ grown on a Si substrate was further investigated. Fig. 6.11 shows ρ_{xy} and ρ_{xx} while sweeping the external magnetic field at 15 mK with an applied $V_G = 4.5$ V. ρ_{xy} reaches the von Klitzing constant h/e^2 and ρ_{xx} vanishes completely after the reversal of the magnetization. A very small deviation is likely due to current leakage through the impedance of the instrument and cryostat leads to the voltage probes. A high precision measurement is presented in the next chapter, confirming perfect quantization. The QAHE was thus successfully realized by lowering the measurement temperature below 50 mK, optimizing the Sb content to $x = 0.79$ and applying a gate voltage. These steps are necessary to shift the Fermi level into the magnetic gap and localize all bulk carriers.

In conclusion, it was established that the in-plane lattice constant a can be used to deduce the Sb content x even in thin $V_z(Bi_{1-x}Sb_x)_{2-z}Te_3$ layers of about 9 nm thickness required for the QAHE. The surface morphology of 50-65 nm and about 9 nm thick layers with an Sb content $x = 0$, $x \approx 0.8$ and $x = 1$ is studied by AFM and XRR measurements. The RMS roughness of the thicker layers reduces significantly with decreasing Sb content by up to a factor of 4. Both the thicker and thinner layers show much larger and more interconnected islands in layers without Sb. XRD measurements show no influence of the Sb content on the mosaicity-tilt and -twist.

A set of about 9 nm thick $V_{0.1}(Bi_{1-x}Sb_x)_{1.9}Te_3$ layers with an Sb content ranging from $x = 0.56$ to 0.95 was studied in magneto-transport. A higher Sb content in the layers seems to increase the coercive field. This may indicate that the ferromagnetic exchange interaction depends on the carrier concentrations. At 4.2 K a change of the sign of the Hall slopes places the charge neutral point around $x = 0.86$. The maximum in ρ_{AHE} of $0.44\,h/e^2$ is observed close to the charge neutral point at $x = 0.76$. The anomalous Hall resistivity increases significantly for measurement temperatures below 50 mK, reaching the von Klitzing constant for a narrow range of x between 0.76 and 0.79. Simultaneously, ρ_{xx} is vanishing after the switching of the magnetization.

Likely, the optimization of the Sb content and the applied gate voltage shifted the Fermi level into the magnetic gap as required for the QAHE. The Sb content and the low observation temperature necessary for the realization of the QAHE are consistent with results from the literature.[CZK$^+$15b, CZK$^+$15a]

7 Study of the quantum anomalous Hall state

The successful realization of the QAHE in the last chapter enables a detailed investigation of its electronic and magnetic properties and their dependence on the substrate type, capping layer and layer thickness.

Standard magneto-transport and superconducting quantum interference device-based magnetometer (SQUID) measurements were conducted by the quantum transport group of EP3 (Würzburg) and in collaboration with the Physikalisch-Technische Bundesanstalt high-precision measurements with metrological accuracy and detailed error analysis became possible. Furthermore, resonant photoemission spectroscopy was conducted by the EP7 (Würzburg) in a close collaboration to investigate the electronic states of Vanadium. The various results summarized in this chapter were published in international journals.[WSG+17, GSW+15, GFS+17a, GFP+18, PBS+16]

7.1 Electronic and magnetic properties

In this chapter, the electronic and magnetic properties of layers exhibiting the QAHE are investigated in detail.

High-precision measurements of the Hall resistivity of a 9 nm thick magnetic TI layer of $V_{0.1}(Bi_{0.21}Sb_{0.79})_{1.9}Te_3$ exhibiting the QAHE were conducted in collaboration with the Physikalisch-Technische Bundesanstalt. The layer was capped with a 10 nm thick Te capping layer and a Hall bar was patterned by optical lithography. The measurements were performed with a cryogenic current comparator bridge at zero magnetic field and 20 mK in a dilution refrigerator.

One challenge for high-precision measurements is that high currents are favorable

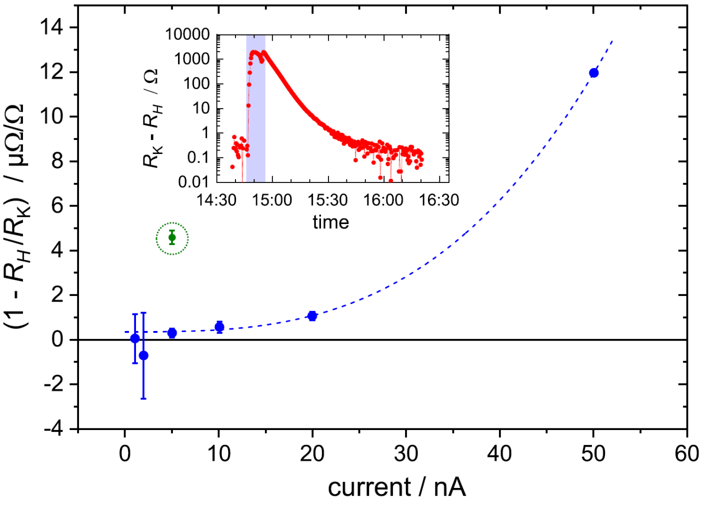

Fig. 7.1: Relative deviation of the Hall resistance R_H from the von Klitzing constant R_K as a function of current at 20 mK and no external magnetic field (2 T for the green point). A fit of the form $a + bI^c$ is shown as blue dashed line. The inset shows the absolute deviation of the Hall resistance during the change of the field (gray area) and afterwards over time.[GFP$^+$18]

to reach high accuracy, but lead to an increased electron temperature causing a deviation from the von Klitzing constant R_K. The relative deviation of the measured Hall resistivity from R_K is shown in Fig. 7.1 for currents between 1 nA−50 nA. At 5 and 10 nA the weighted average of several measurements was plotted, while all other points represent single measurements. The green circled point was taken at 2 T, before sweeping the magnetic field to zero for the other measurements. In the inset, the deviation from R_K is shown during this sweep (shaded area) and the time for stabilization. The observed deviation likely results from heating effects caused by the sweep. The data points in the main diagram were fitted using the form $a + bI^c$, which results in $a = (0.35 \pm 0.10) \times 10^{-6}$. With additional corrections for geometrical contributions from a non-vanishing longitudinal resistivity and additional uncertainty considerations, the analysis yields a relative deviation from R_K of $(0.17 \pm 0.25) \times 10^{-6}$. Despite using low currents, a very small uncertainty could be obtained with excellent agreement with R_K. For further information on the uncertainty budget and measurement details see [GFP$^+$18].

This result was reported as the smallest, most precise value at the date of publication, proving the high stability of the QAHE in the provided samples. Comparable result were later published in [FRY$^+$18]. This is a big step toward a zero-field resistance standard, which combined with a Josephson voltage forms the ultimate electrical standard yielding voltage, current and resistance from one reference instrument.[GFP$^+$18]

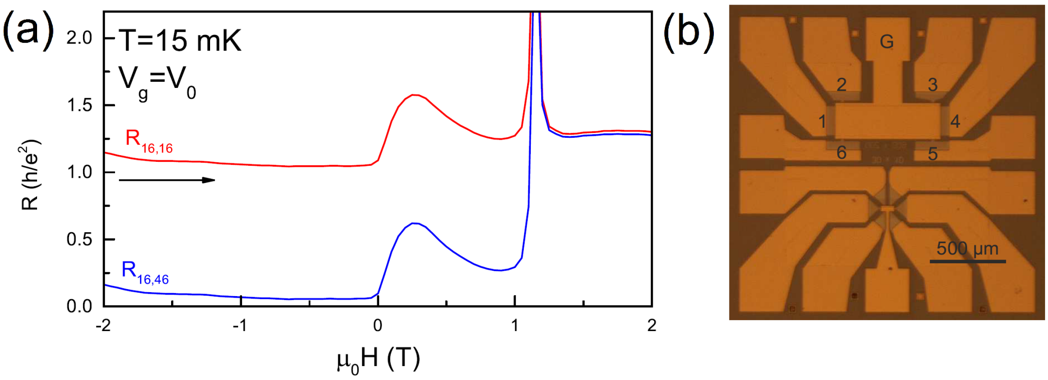

Fig. 7.2: (a) Non-local measurement of the voltage between contact 1 and 6 as well as contact 4 and 6 divided by the current flowing between contact 1 and 6 denoted as $R_{16,16}$ (red) and $R_{16,46}$ (blue), respectively. The contacts and the gate are labeled on the optical photograph of the Hall bar in (b).[GSW$^+$15] (© 2015 American Physical Society)

Furthermore, non-local measurements were conducted at 15 mK to confirm edge state transport in the provided layers. The results of such a measurement are shown in Fig. 7.2 (a) with an optical photograph of the Hall bar with labeled contacts in (b). $R_{ab,cd}$ is defined as the voltage between contact c and d divided by the current flowing between contact a and b. In Fig. 7.2 the voltage of the red and blue curve are measured between contact 1 and 6 and between 4 and 6, respectively. For both curves the current is passed between contact 1 and 6 in either a clockwise direction for positive magnetic fields or counterclockwise manner for negative magnetic fields. For the red curve the measured value is close to the von Klitzing constant for both magnetization directions after the magnetic switching. The blue curve shows a value close to the von Klitzing constant only for the clockwise current at positive fields. A value close to zero is observed for the counter clockwise current at negative fields, since no current is passing through contact 4 and the potential difference U_{46} is zero. This is consistent with the result predicted by the Landau-Büttiker formalism [Büt86] and confirms transport through edge states along the edge of the sample. The deviations from the von Klitzing constant and zero are likely caused by contact resistances.

Next, the magnetic properties of the layers are investigated. SQUID measurements yield a Curie temperature of $T_C = 26\,\mathrm{K}$, significantly above the observation temperature of the QAHE. A detailed analysis of several features in transport measurements indicate instabilities in the magnetic phase even at 15 mK. The first such feature is a bump in the longitudinal and Hall resistivity after sweeping through zero external magnetic field as seen in Fig. 6.11 in the previous chapter, the non-local measurements in Fig. 7.2 and in Fig. 7.8. The feature is present in both sweep directions showing a hysteretic nature. It seems to appear whenever H is swept through zero, although this value should hold no special meaning given that the effective magnetic field B consists of the external magnetic field $\mu_0 H$ and the magnetization $\mu_0 M$. Over time it partially relaxes back towards the quantized values. The feature shows furthermore a temperature dependence and vanishes above about 1 K. Such a behavior indicates a superparamagnetic origin of the observed feature.

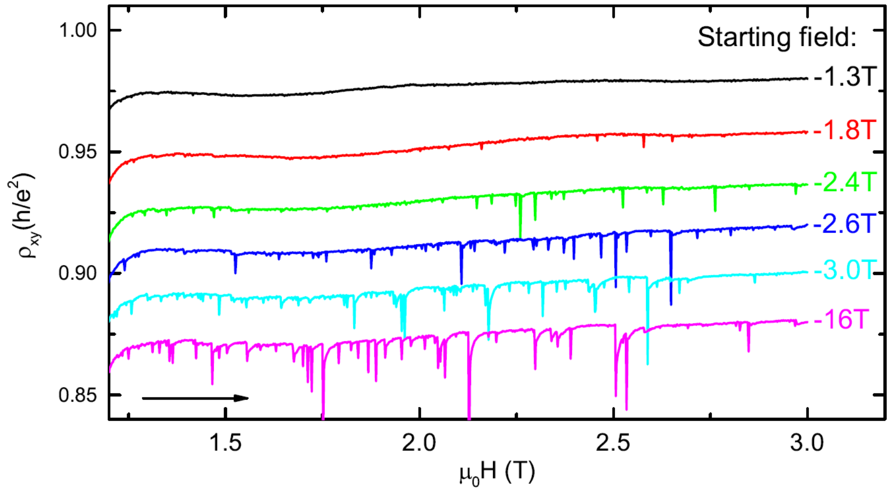

Fig. 7.3: Hall resistivity ρ_{xy} while sweeping the external magnetic field from a negative starting field to beyond the coercive field $\mu_0 H_C = 1.2\,\mathrm{T}$. Curves for different starting fields are offset for clarity.[GSW+15] (© 2015 American Physical Society)

Another peculiar feature are spikes in the Hall resistivity observed only after the switching of the magnetization above H_c. The spikes are not visible if the magnetic field is allowed to settle in a short period of time before acquiring a measurement point (as in Fig. 6.11), but show up if a continuous sweep of the magnetic field is used (black curve in Fig. 7.8).

Fig. 7.3 shows that the amplitude of the spikes depend on how far the samples are magnetized in the opposite direction before sweeping the magnetic field beyond the coercive field. For a low starting field of -1.3 T, barely beyond the coercive field, no spikes are observed and the higher the starting field the more spikes with higher amplitudes become visible. A likely explanation is that small parts of the sample suddenly change magnetization causing the spikes. For small starting fields these unstable magnetic parts are still in a stable configuration for positive magnetization.

Additionally, a peculiar behavior was observed when warming up the sample. The Hall resistivity ρ_{xy} decreases from quantization in sudden jumps, which seem to be correlated with changes in the warming rate, when the heater power was changed. This again suggests an unstable magnetic state influenced by a change in temperature. More details can be found in [GSW$^+$15].

These results show that despite the perfect quantization achieved in these layers, superparamagnetic contributions are present in the nominally ferromagnetic magnetic phase.

To further investigate the origin of the ferromagnetic phase and the electronic structure of the magnetic TI layers, element-specific resonant photoemission spectroscopy (resPES) was used to probe the valence band for the V 3d impurity states, which may provide a mechanism of ferromagnetic coupling in the bulk insulating state. The measurements and analysis was performed by the group of EP7 (Würzburg) using PETRA III at the electron synchrotron DESY.

Probed samples comprise $V_z(Bi_{0.2}Sb_{0.8})_{2-z}Te_3$ layers with $z = 0.1$, which show quantization, $z = 0.2$ for an increased signal and $z = 0.0$ as reference. The layers were capped with a 200 nm thick amorphous Se layer to avoid contamination during the transport. All measurements were conducted at room temperature. Further details of the measurement technique and a detailed analysis can be found in [PBS$^+$16].

First, X-ray absorption spectroscopy was used to determine the energy of the V $L_{2,3}$ absorption edges, which was utilized in resPES to enhance the resonant V $2p \rightarrow 3d$ transition. The difference spectrum between on- and off-resonance shown in Fig. 7.4 (upper panel) for the layer with $z = 0.2$ can be interpreted as the element-specific V 3d states. A peak is observed at about 0.3 eV below E_F with finite intensity at E_F. This peak is attributed to the formation of an impurity band near the valence band maximum. As a control experiment, the undoped reference sample was probed in the same way and shows no difference between on- and off-resonance.

The lower panel of Fig. 7.4 shows *ab initio* calculations of the spin-polarized DOS with the V 3d states as full lines in the ferromagnetic state, as dashed lines in the paramagnetic state and the host and impurity states together as shaded area. The calculated DOS is in good agreement with the experimental results and suggests

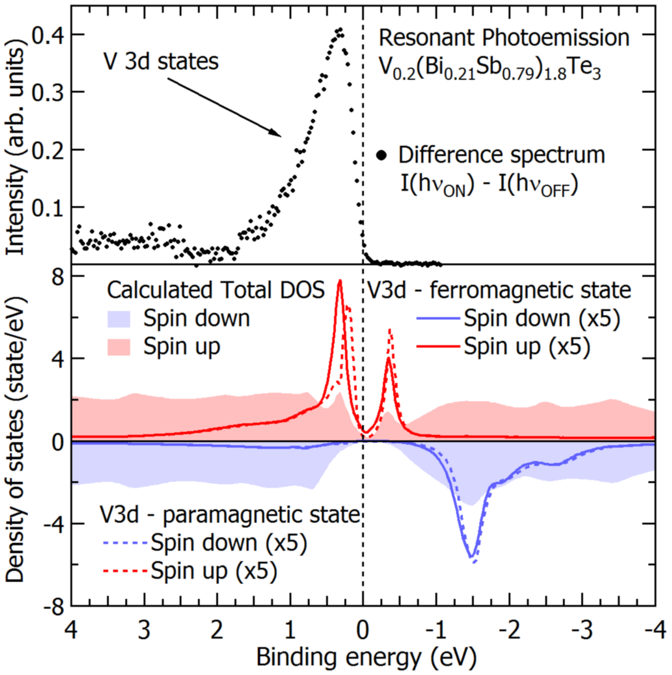

Fig. 7.4: The upper panel shows the measured resPES difference spectrum which is sensitive to the V 3*d* states of (V,Bi,Sb)$_2$Te$_3$. The lower panel shows the total calculated spin-resolved DOS (shaded areas) and the exchange-split V 3*d* impurity states (magnified by ×5) in ferromagnetic (solid line) and paramagnetic (dashed line) states. The measured resPES peak is attributed to the calculated V spin-up band just below the Fermi level.[PBS+16] (© 2016 American Physical Society)

that the observed intensity is from the occupied spin up states.

The electronic structure suggests that not only the previously discussed Van Vleck mechanism [LCW+15, CZK+15b, CZF+13, YZZ+10a] could mediate the ferromagnetism in the magnetic TI layers, but double exchange interaction enhanced by the finite density of states at E_F, possibly coexisting with a superexchange interaction, is a possible candidate as well.

In conclusion, high precision measurements with metrological accuracy confirm perfect quantization of the magnetic TI layers. Non-local measurements show clear evidence of edge state transport. Several anomalies in transport measurements indicate superparamagnetic contributions to the nominally ferromagnetic phase in which the QAHE is observed. The electronic structure of the V 3*d* states measured by resPES is found to fulfill all requirements for double exchange and superexchange interaction as mechanisms to mediate ferromagnetism between the Vanadium atoms.

7.2 Influence of capping layer and substrate

In this chapter, the structural properties of layers on different substrates and their impact on the observation of the QAHE will be investigated.

Additional to the previously used Si(111)-H, better lattice matched semi-insulating Fe:InP(111)B is used as substrate. Prior to growth, these substrates were annealed at 640°C in Te atmosphere, until a spotty RHEED pattern changed to sharp lines indicating a smoothening of the surface. Layers were grown under the same growth conditions as the quantized layers on Si(111) resulting in the same composition. It is known, that the substrate type can influences e.g. the roughness and rotational order of the layers significantly and can lead to individual band-bending effects at the interface.[STK+13, TSB+12]

Not only the substrate, but also the capping layer may have an impact on the QAHE. Various capping layers like the crystalline Te and AlO_x were used in the literature.[CZK+15b, BFK+15] It was claimed that capping layers would influence or even hinder the observation of the QAHE.[PSA+15] Utilizing the highly reproducible growth conditions developed in previous chapters, such claims can be checked simply by comparing nominally identical layers with and without a capping layer. The studied uncapped layer (sample A) was under ambient conditions for several months before processing, which provided sufficient time for a possible layer degradation.

Fig. 7.5 (a) shows a representative $2\theta - \theta$ XRD scan of a $V_{0.1}(Bi_{0.21}Sb_{0.79})_{1.9}Te_3$

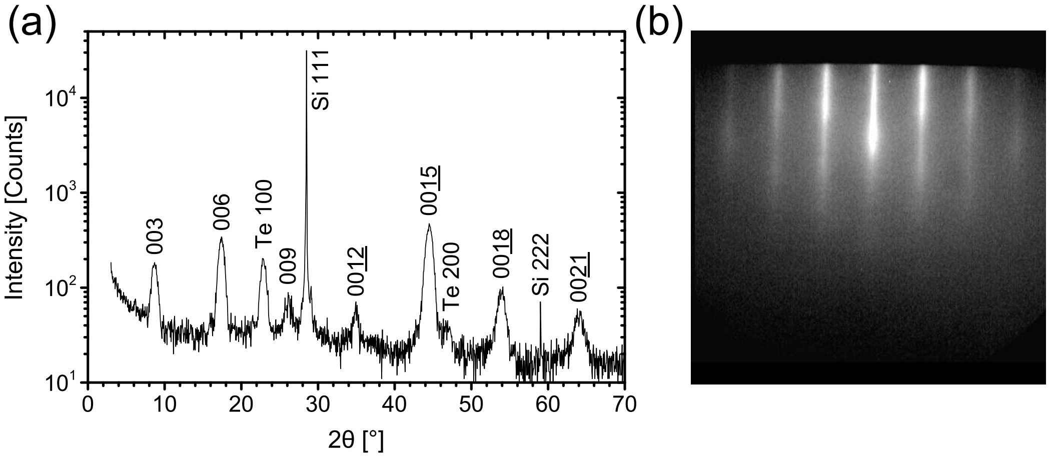

Fig. 7.5: (a) $2\theta - \theta$ diffractogram of a 9 nm thick $V_{0.1}(Bi_{0.21}Sb_{0.79})_{1.9}Te_3$ layer with 10 nm Te capping layer on Si(111) (sample B) (b) RHEED pattern from the surface of a representative layer.[WSG+17] (© 2017 American Physical Society)

layer grown on a Si(111) substrate with a thickness of 9 nm and capped with a 10 nm Te layer (sample B). The peaks are identified as the 003<u>n</u> reflections of the TI layer with additional peaks from the Si substrate and the Te capping layer. The occurrence of peaks originating from the layer, substrate and capping layer shows not only that the Te capping layer is at least partially crystalline, but also the parallel alignment of crystallographic planes in the full layer stack. The observed peaks from the layer are comparable to the layer peaks on InP (not shown).
Fig. 7.5 (b) shows a post-growth RHEED pattern representative for layers on Si(111). While the well-defined lines indicate rather smooth growth, layers on InP exhibit slightly sharper lines. This indicates a better layer quality on InP substrates.

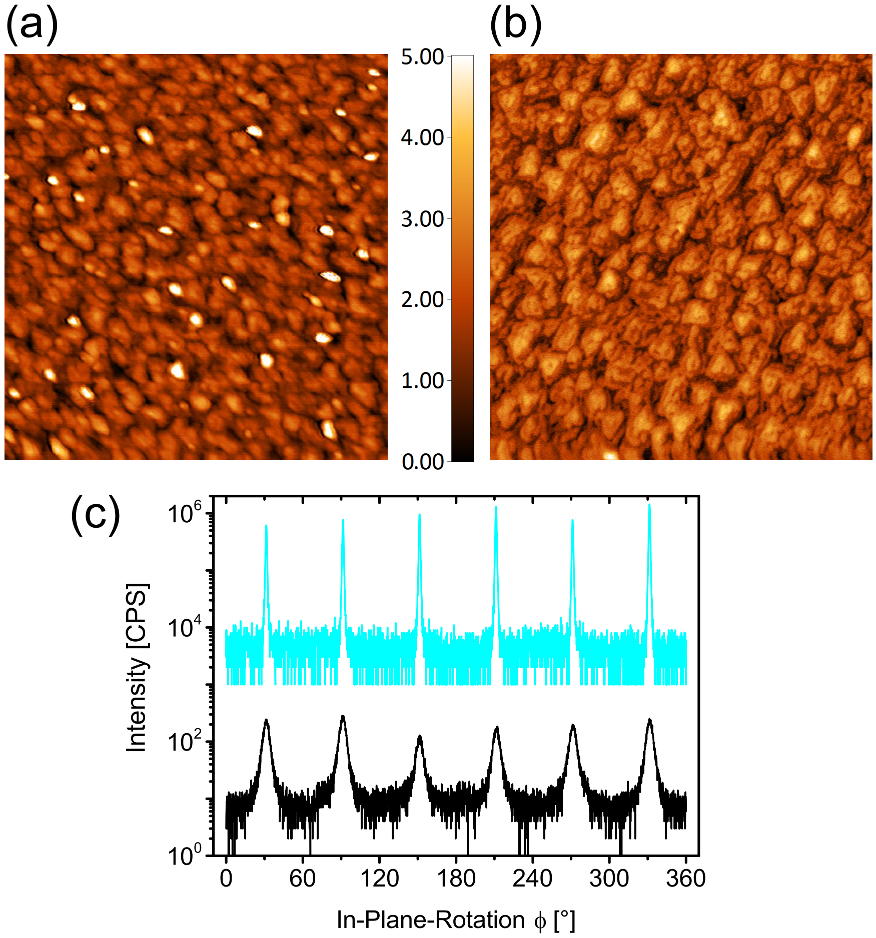

Fig. 7.6: (a) and (b) show 2×2 µm^2 AFM images with a 5 nm z scale of uncapped 10 nm thick $V_{0.1}(Bi_{0.21}Sb_{0.79})_{1.9}Te_3$ layers on Si(111) (sample A) and InP(111), respectively. (c) In-plane rotation diffractogram of the 015 reflections of a capped layer on Si (black, sample B) and a capped layer on InP (cyan, sample C).[WSG$^+$17] (© 2017 American Physical Society)

In Fig. 7.6 (a) and (b) $2\times2\,\mu\mathrm{m}^2$ AFM images of 10 nm thick $V_{0.1}(Bi_{0.21}Sb_{0.79})_{1.9}Te_3$ layers on Si(111) (sample A) and InP(111) are shown with a 5 nm z scale. The RMS roughness of both layers is 0.7 nm. Compared to the layer on Si(111) with an average island diameter of 100 nm, the layer on InP shows more interconnected islands with wider QL terraces and a larger average diameter of about 140 nm.

In Fig. 7.6 (c) in-plane rotation diffractograms of the 015 reflections of capped layers on Si (black, sample B) and InP (cyan, sample C) are presented. The appearance of six peaks of about equal intensity is a clear signature of twinning.[STK$^+$13] The FWHM of the peaks is 5.4° for the layer on Si and only 1.0° for the layer on InP. This shows a significantly improved in-plane orientation on InP, likely due to the smaller lattice mismatch.[TSB$^+$12] The rocking curve FWHM of the 006 reflection is similar for both substrates with 0.9° on Si and 0.8° on InP (not shown here).

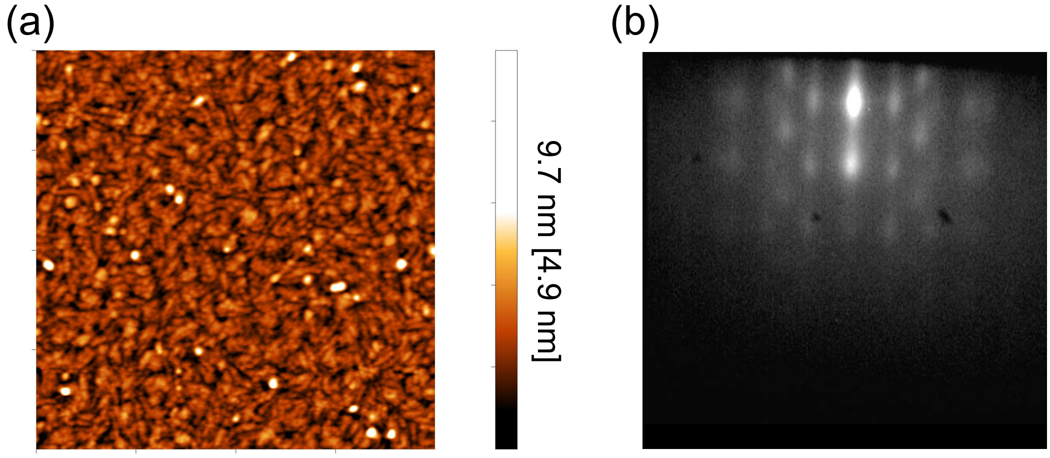

Fig. 7.7: (a) $2\times2\,\mu\mathrm{m}^2$ AFM image of an about 10 nm thick Te capping layer on a $(V,Bi,Sb)_2Te_3$ layer (b) RHEED pattern of the surface of a similar Te capping layer.

Next, the structural properties of the Te capping layers will be discussed. In Fig. 7.7 (a) a $2\times2\,\mu\mathrm{m}^2$ AFM image is shown with an about 5 nm z scale similar to the previous AFM images of the layers. The morphology features slightly smaller islands than the layers and a high number of thin elongated ridges. The RMS roughness of 0.7 nm is comparable to that of the layers and is probably inherited. Excluding outliers, the height difference between low and high points is about 5 nm. A 10 nm thick Te capping layer thus provides complete coverage of the layer.

Fig. 7.7 (b) shows a RHEED pattern of a capping layer similar to the observed pattern in [CZK$^+$15c]. The streaks with spots on top indicate a rough and at least partially crystalline capping layer, which is consistent with the observation of the Te 100 reflection in XRD. During the deposition of the first few monolayers of Te, the RHEED becomes diffuse before exhibiting the pattern. This suggests an amorphous Te layer at the interface. However, the observation of rotational alignment of 100 nm thick capping layers to the layer in in-plane rotation XRD scans (not shown here) proves that structural information is passed from the TI layer to the capping layer. It is thus more likely that the diffuse appearance in RHEED is caused by broadening of the streaks due to the rough interface, the low crystalline quality and the small amount of material.

Finally, the magneto-transport properties of the previously investigated capped layers on Si(111) (sample B) and InP(111) (sample C) as well as the uncapped layer on Si(111) (sample A) are compared. All samples were grown under the same growth conditions and show only minor differences in Sb content x between $0.76-0.79$.

Fig. 7.8 (a) shows the Hall resistivity ρ_{xy} and (b) the longitudinal resistivity ρ_{xx} against the external magnetic field, respectively. The capped and uncapped sample A and B on Si show perfect quantization in ρ_{xy} with vanishing ρ_{xx}. Sample C on InP shows a slight deviation of about 5% from the von Klitzing constant and a finite residual longitudinal resistivity ρ_{xx} of about $5.2\,\mathrm{k\Omega}$. The reason could be parasitic bulklike carriers, which remain delocalized in the more homogenous layer. Given that quantization is only observed within a narrow range of Sb content x, it can not be excluded that the deviation is caused by a slightly different x of the layer on InP, though.

The capping layer does not seem to influence the observation of the QAHE. However, results might differ depending on the chemicals used in the lithographic process, which can react with the bare layer. A noticeable difference for the uncapped layer is a higher ρ_{xx} peak at the reversal of the magnetization. In the next chapter it will be shown that this is characteristic for thinner layers. This may indicate that the uncapped layer is effectively thinner, possibly due to oxidization of the surface.

Overall the results show that the QAHE is rather robust against changes in substrate, crystalline quality and capping with small deviations observed on InP.

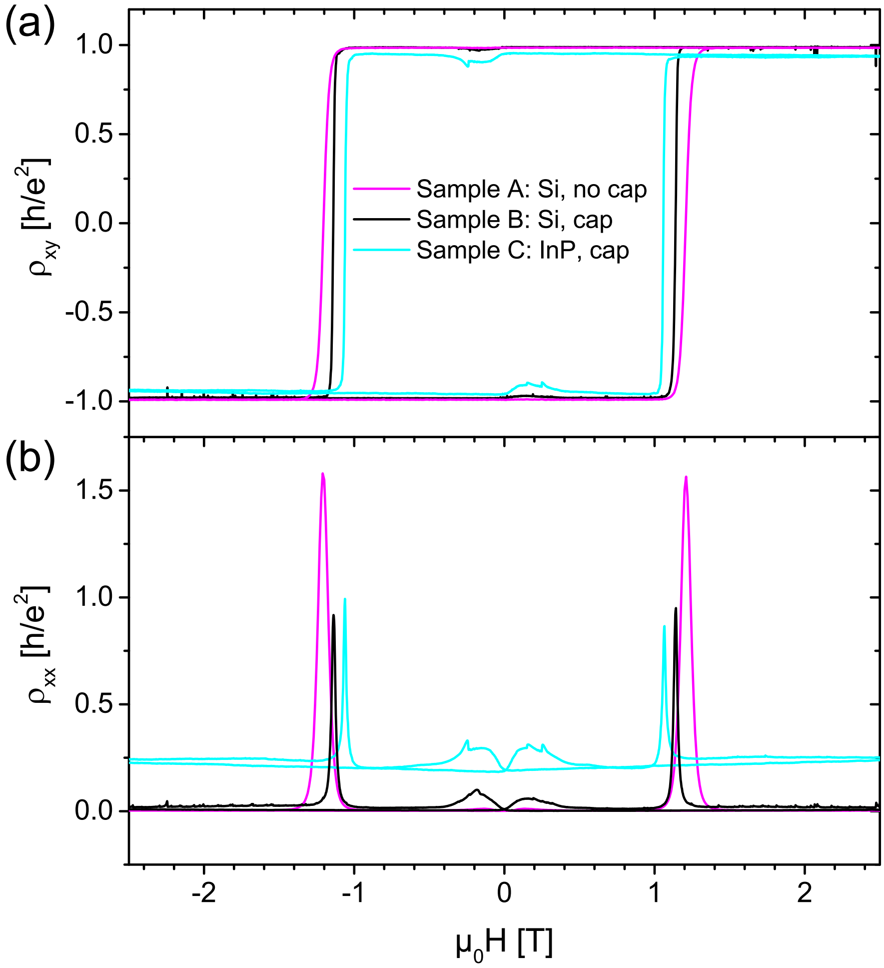

Fig. 7.8: (a) Hall resistivity ρ_{xy} and (b) longitudinal resistivity ρ_{xx} of an uncapped layer on Si (sample A, magenta), a capped layer on Si (sample B, black) and a capped layer on InP (sample C, cyan). The measurements were conducted with applied gate voltage at 50 mK and below.[WSG$^+$17] (© 2017 American Physical Society)

7.3 Quantum anomalous Hall effect in 2D and 3D layers

In the following, the influence of the layer thickness on the properties of the quantum anomalous Hall state is investigated. The stable growth conditions established in earlier chapters are used to reduce the thickness from 9 nm to 8 nm and 6 nm while keeping the composition nearly constant. The Sb content x determined by XRD varies only between $0.78 - 0.79$.

Previous similar studies observed the QAHE only between 3-5 nm layer thickness.

[FFW+16] The authors speculated that below these thicknesses the hybridization energy dominates the exchange energy, the layer becomes a trivial insulator or quantum spin Hall insulator. Above 5 nm thickness the gating could become less effective for the more distant bottom surface state, leading to a potential difference between the two surfaces states, which effectively closes the gap.[FFW+16] Lower intrinsic doping levels, which require smaller gate voltages, may enable the QAHE in thicker layers. Such layers above 6 nm thickness show no hybridization between top and bottom surface states and can be considered a 3D TI.[ZHC+10, LSY+10, LZY+10] Theoretical predictions for the QAHE exist not only for thinner 2D layers [YZZ+10b], but distinct theories also exist for such 3D TI layers [NN11, QHZ08]. The physics of this QAHE involve axion electrodynamics with an $\theta E \cdot B$ term added to the Maxwell equations, which makes the study of these thicker layers particularly interesting.

The observation of the QAHE in 9 nm thick layers in the previous chapter enables us to study such 3D layers. The magneto-transport measurements and analysis were performed by the magneto-transport group in EP3. The results were publishing in [GFS+17a] and shall be summarized in this chapter.

Fig. 7.9 (a) and (b) show the Hall resistivity ρ_{xy} and the longitudinal resistivity ρ_{xx} of $V_{0.1}(Bi_{1-x}Sb_x)_{1.9}Te_3$ layers plotted as a function of the external magnetic field. The chosen samples are five 9 nm layers with varying Sb content around $x = 0.79$ (full lines) as well as an 8 nm and 6 nm thick layer (dashed lines) with $x = 0.78$ and 0.79, respectively. The thicknesses were carefully determined by XRR measurements and are clearly distinguishable despite the small differences. At the magneto-transport measurement temperature of 25 mK, all layers can be tuned close to charge neutrality by applying a gate voltage and are thus dominated by edge state transport exhibiting $\rho_{xy}(H = 0) > 0.8\,h/e^2$. For thicker layers of e.g. 15 nm thickness with a similar composition a strongly reduced $\rho_{xy} < 0.2\,h/e^2$ is observed[GFS+17b], possibly due to less efficient gating or bulk conduction. Our thinner layers below 6 nm thickness typically become insulating at mK temperatures, conceivably due to the hybridization energy surpassing the exchange energy, which may push the layers into the trivial insulator phase.[FFW+16, LSY+10, LZY+10]

In Fig. 7.9 (b), layers with a thickness $d = 9$ nm (full lines) show a ρ_{xx} peak value close to or below h/e^2 at the coercive field, while the thinner 8 nm and 6 nm layers (dashed lines) exhibit peak values up to about $2.5\,h/e^2$, which increase with decreasing layer thickness.

The longitudinal conductivity σ_{xx} and the Hall conductivity σ_{xy} of the layers can

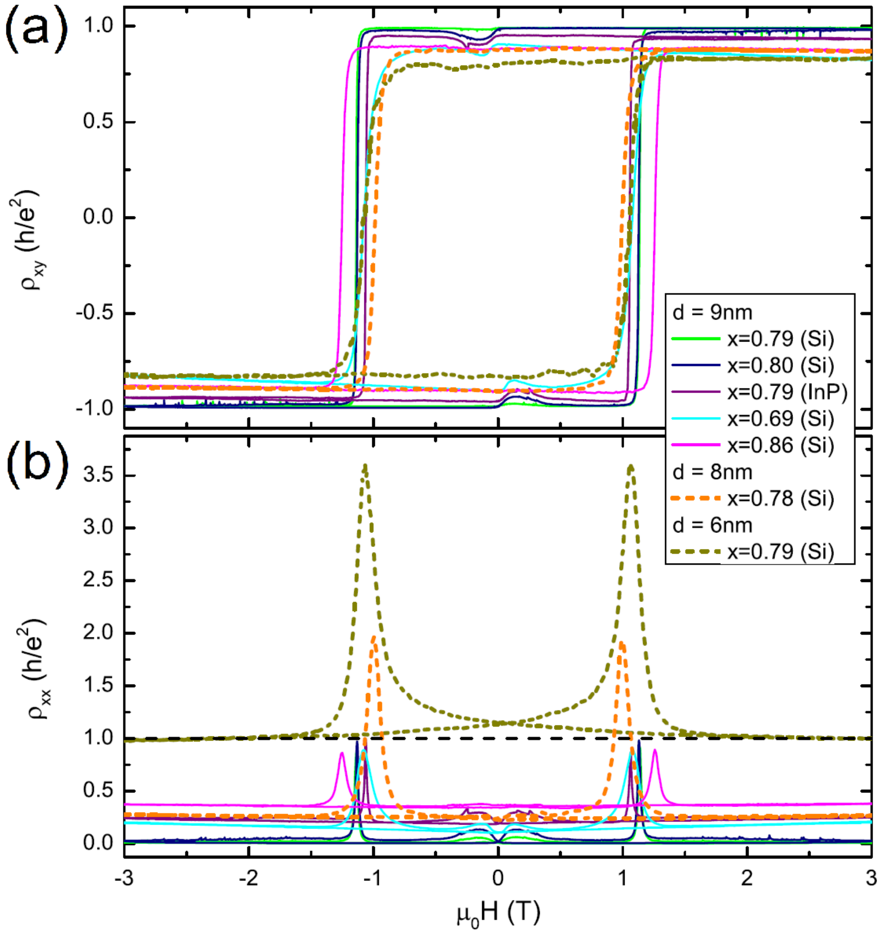

Fig. 7.9: (a) Hall resistivity ρ_{xy} and (b) longitudinal resistivity ρ_{xx} plotted as a function of the external magnetic field at 25 mK. The individual Sb content x, thickness d and substrate types of $V_{0.1}(Bi_{1-x}Sb_x)_{1.9}Te_3$ layers are indicated in the legend. The thicker layers with $d = 9$ nm are shown as solid lines while the thinner layers with $d = 8$ nm and $d = 6$ nm are shown as dashed lines.[GFS+17a] (© 2017 American Physical Society)

be calculated by equation 4.9. The behavior of these conductivities during the reversal of magnetization can be characterized using flow diagrams, which show σ_{xx} against σ_{xy} while the external magnetic field is used to reverse the magnetization. Fig. 7.10 shows a flow diagram of the measurements for the three layers with 6 nm, 8 nm and 9 nm thickness and x close to 0.79.

The scaling of the integer quantum Hall effect (IQHE) of a trivial 2D electron gas has the shape of two semicircles centered on $(\sigma_{xy}, \sigma_{xx}) = (\frac{1}{2}e^2/h, 0)$ and $(-\frac{1}{2}e^2/h, 0)$ shown as black dashed line.[Dol99] For the 6 nm thick layer, the observed scaling is qualitatively consistent with this IQHE scaling, as previously observed in other samples exhibiting the QAHE [CYT+14]. The predicted scaling for one topological surface state of a magnetic 3D TI follows a semicircle with

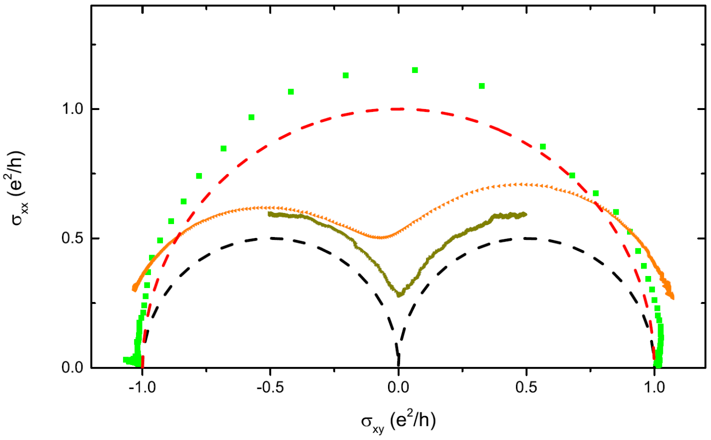

Fig. 7.10: Longitudinal conductivity σ_{xx} against the Hall conductivity σ_{xy} while sweeping the external magnetic field. Three layers with $d = 9\,\mathrm{nm}$, $8\,\mathrm{nm}$ and $6\,\mathrm{nm}$ and similar composition are shown in green, orange and dark yellow, respectively. The flow diagram of the IQHE is shown as black dashed line and two parallel conducting topological surface states as red dashed lines.[GFS+17a] (© 2017 American Physical Society)

the same radius $\frac{1}{2}e^2/h$ centered around $(0,0)$ due to the finite Berry phase.[NN11] For $9\,\mathrm{nm}$ thick layers a semicircle centered around $(0,0)$ with a radius of e^2/h is observed. This matches the flow diagram expected for the sum of two parallel conducting topological surface states (top and bottom) of a 3D TI shown as red dashed line. For the $8\,\mathrm{nm}$ thick layer a scaling behavior in between the two cases is observed with a dip at about $\sigma_{xy} = 0$.

The key difference of the IQHE and the axionic scaling of a 3D TI is the position of the center of the semicircles. The $6\,\mathrm{nm}$ and $8\,\mathrm{nm}$ thick layers are not perfectly quantized, likely due to the lack of optimization of the Sb content for such thinner layers causing some residual bulk conductance. However, both layers are in the QAHE regime and show a clear transition from axionic scaling expected for magnetic 3D TI layers to IQHE scaling expected for 2D layers.

As already mentioned, $9\,\mathrm{nm}$ thick uncapped layers show increased ρ_{xx} peak values, e.g. in Fig. 7.8, which leads to the dip at $\sigma_{xy} = 0$ in the flow diagrams. The longer the layer was kept in ambient conditions providing time for degradation, the more pronounced this dip becomes, until the scaling is consistent with IQHE scaling (full flow diagrams are shown in [GFS+17b]). This indicates that the top surface oxidizes, which reduces the effective thickness of the layer.

In conclusion, the study of flow diagrams of layers with different thicknesses shows that the QAHE in 6 nm thick layers exhibits integer quantum Hall scaling as expected for 2D TI layers as well as 2D electron gases. On the contrary, the observed scaling of 9 nm thick layers originates from the two topological surface states of a magnetic 3D TI, each contributing $\frac{1}{2}e^2/h$ to the Hall conductivity. This distinct scaling behavior of the 3D layers is consistent with that expected in the presence of axionic action characterizing the electrodynamic response of a magnetic 3D TI, i.e., an axion insulator.[GFS+17a]

8 Influence of the V content on the properties of (V,Bi,Sb)$_2$Te$_3$

After realizing the QAHE in (V,Bi,Sb)$_2$Te$_3$ layers, the influence of Vanadium doping on the structural, electronic and magnetic properties of such layers is investigated in detail in this chapter.

Previously published studies investigated the influence of V on Sb$_2$Te$_3$ [CZK$^+$15b, CZK$^+$15c, CZU05, DHLcvU02, MMC$^+$14, ZCU05] and (Bi,Sb)$_2$Te$_3$ [WSG$^+$17, RDD$^+$17] with inconsistent results. Claims range from increased to decreased lattice constants, from additional n-type over charge neutral to p-type doping caused by V and widely fluctuating magnetization values from 0.6 μ_B up to 2.6 μ_B per V ion. A value of 2.0 μ_B is predicted by theoretical calculations with an induced moment for the next-nearest Te neighbors of -0.27 μ_B.[ICP$^+$18] Consequently, there is no agreement on the valence or magnetic state of V, which was suggested to incorporate as V^{3+}, V^{4+} or V^{5+} ion.[CZK$^+$15b, MMC$^+$14, CZU05, DHLcvU02]

In order to investigate the influence of V systematically, a series of about 50 nm thick V$_z$(Bi$_{0.2}$Sb$_{0.8}$)$_{2-z}$Te$_3$ layers of varying V content z ($z = 5 \times$ [V at.%]) was grown by MBE. Growth conditions and Sb content x were kept similar to layers exhibiting the QAHE. While the thicker layers do not exhibit the QAHE, properties like the incorporation of V and the magnetization per V ion can be assumed to be independent of layer thickness and structural changes should be at least qualitatively consistent with thinner layers. Structural analysis was conducted using AFM, EDX and XRD measurements and an additional magnetic characterization with SQUID measurements was performed by the transport group in EP3. The increased thickness provides an improved signal-to-noise ratio for high accuracy EDX and XRD measurements.

The layers were grown on Si(111) substrates prepared by dipping them in a 50% HF solution prior to growth. The substrate was subsequently heated to the growth temperature $T_{Sub} = 190°\text{C}$ as employed for the layers exhibiting the QAHE to avoid desorption. A series of seven samples was grown only varying the temperature of the V cell. This results in the V content of the layers systematically increasing from 0.6 at.% up to 8.3 at.%, while the Sb content x was fixed at 0.8. An additional reference layer was grown with closed V cell shutter at a V cell temperature of 1525°C similar to the other layers. A growth rate of about 0.3 nm/min and a Te overpressure with a (Bi+Sb)/Te BEP ratio of 1/5 was chosen, as it was used for the quantized layers. The resulting layer thickness after 171 minutes of about 50 nm is sufficient to avoid the fluctuations in the lattice constant c observed in chapter 6.1 and achieve a high signal-to-noise ratio in the measurements. During the growth RHEED revealed sharp streaks indicating a smooth surface.

Fig. 8.1 (a) shows the EDX measurements performed under grazing incident with an angle of 10° between sample surface and electron beam. The intensity was normalized to the background to compare the peak heights. A significant increase of the peak intensities of Te and V is observed for increasing V cell temperatures, while the peak intensities of Bi and Sb stay about constant. The increasing peak intensity of Te indicates that Te bonding partners attach to the extra V, since excess Te desorbs at these substrate temperatures. To quantify the elemental composition of the layers, simulations at grazing incidence were fitted to the spectra. The V content in the layers was found to increase from 0.6 at.% up to 8.3 at.%. The atomic V incorporation rate is assumed to be equal to the atomic V flux reaching the sample, since the low vapor pressure of V should cause a sticking coefficient close to unity. The V flux can thus be calculated from the V content, the layer thickness and the unit cell volume or mass density. This V flux is plotted in the inset of Fig. 8.1 (a) against the V cell temperature. An exponential thermally activated behavior is observed, following a linear fit in the Arrhenius plot. The slope is furthermore consistent with the increase of V vapor pressure at specific temperatures given in [O'H03].

In Fig. 8.1 (b), the V, Bi, Sb and Te content of the different layers is plotted against the calculated V flux of the layers. The estimated error of the V content increases from ±0.2 at.% to ±0.4 at.% with increasing V content. The Te content is constant at an average 60.7 at.% with a low standard deviation of 0.1 at.%. The sum of Bi, Sb and V thus average to 39.3 at.%. Assuming a systematic error of about 1 at.%, this is consistent with a constant Te content of 60 at.% expected for $(V,Bi,Sb)_2Te_3$ layers with substitutional incorporation of V at group-V sites. At this point, the formation of a separate V_2Te_3 phase can not be ruled out, though. On the other hand, an incorporation of V at Te sites or interstitial sites, e.g. in the van der Waals gap, would cause a deviation of the Te content from 60 at.% at

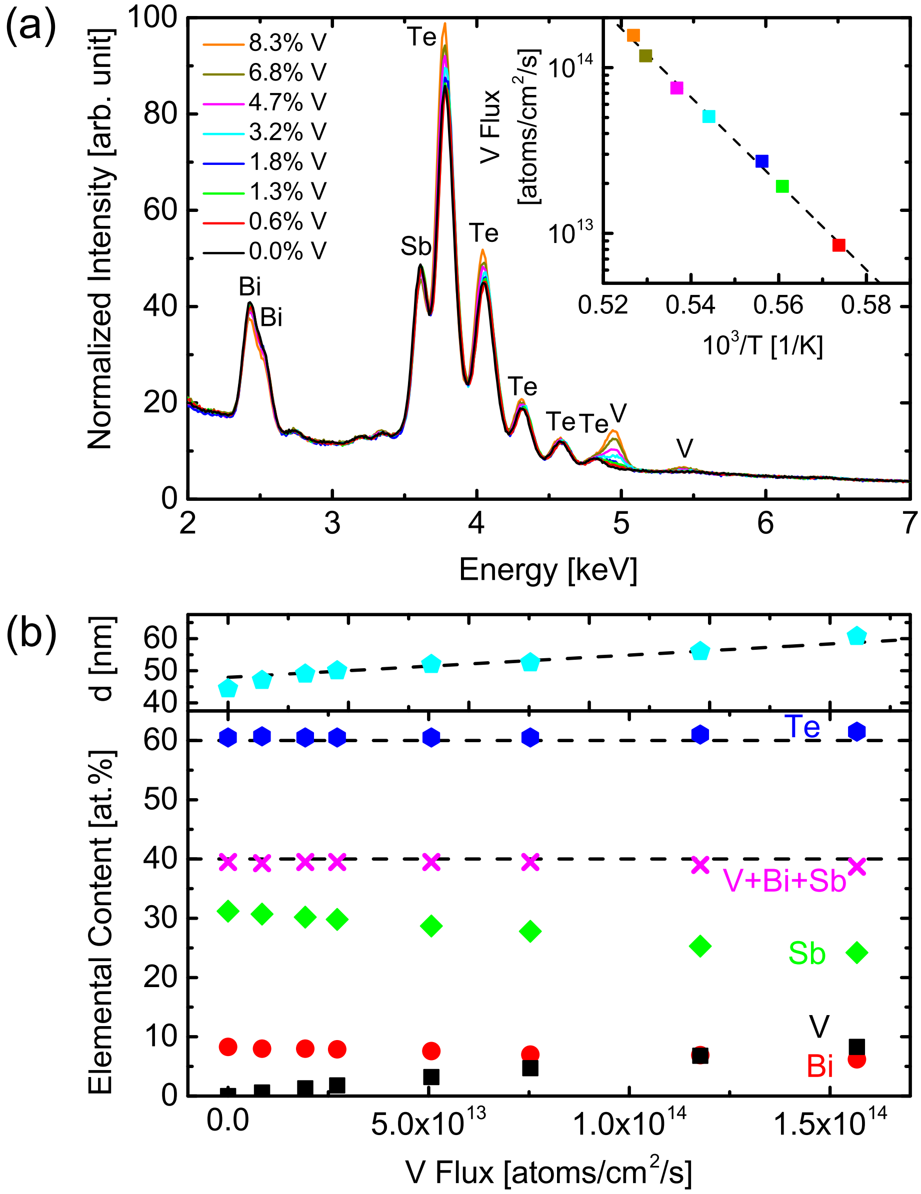

Fig. 8.1: (a) Normalized EDX measurements of about 50 nm thick $V_z(Bi_{0.2}Sb_{0.8})_{2-z}Te_3$ layers grown at V cell temperatures T. An Arrhenius plot of the V flux against $10^3/T$ is shown in the inset. (b) The V, Bi and Sb content as well as the thickness d of the layers determined by EDX and XRR against the V flux employed for the individual samples.

a higher V content.

The Sb content x is between 0.78−0.80 for all layers, similar to the layers exhibiting the QAHE. The influence of the Sb content x on structural and magnetic properties observed in the previous chapter 6.2 is regarded as constant for these layers. Thus, the influence of V can be isolated and studied.

The upper part of Fig. 8.1 (b) shows the layer thickness d as it increases with the offered V flux. The values were obtained by fitting the XRR scans shown in Fig. 8.2 (c). The expected increase in thickness for the measured V content values due to the additional V and Te bonding partners in a 2/3 ratio was calculated and plotted as a dashed line. The calculation included slight corrections for the changing unit cell volume observed in XRD. The thickness of the doped layers is in good agreement with the expected behavior. The undoped layer is about 3.6 nm thinner than expected, though. This is consistent with the results from chapter 6, which show material desorption for such layers without V, likely due to inefficient nucleation.

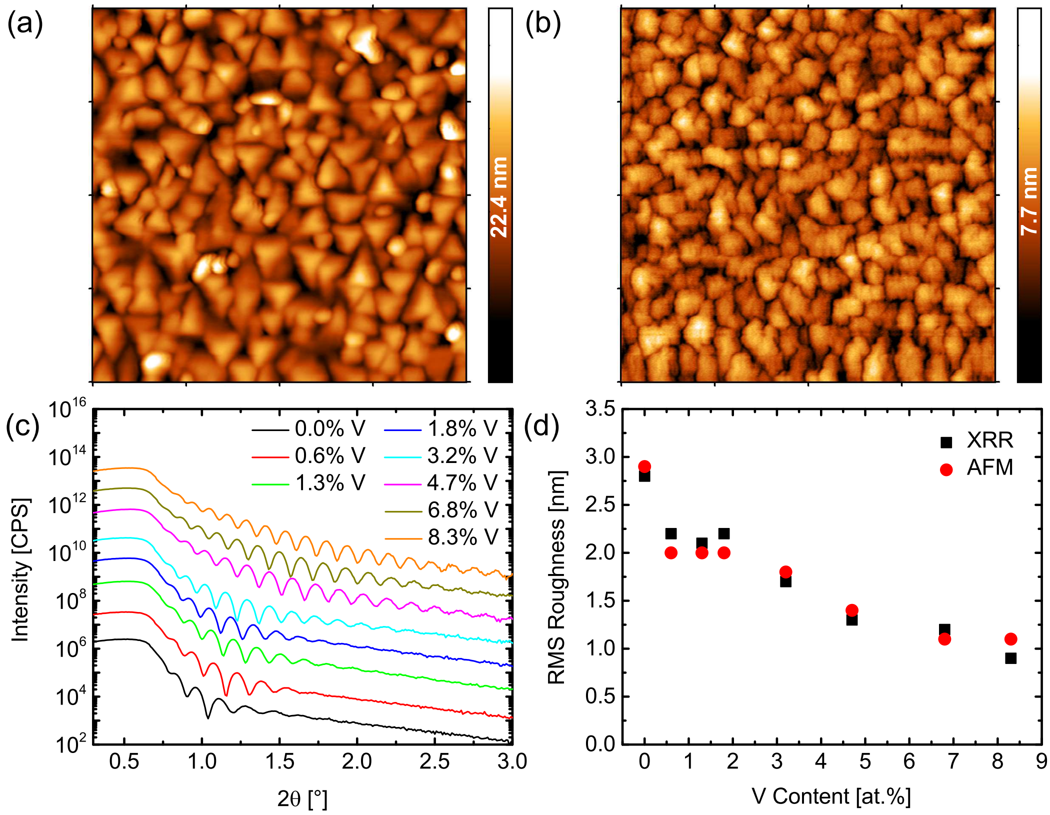

Fig. 8.2: (a) and (b) 2×2 µm^2 AFM images of the surface of an undoped 44 nm thick $(Bi_{0.21}Sb_{0.79})_2Te_3$ layer and a 59 nm thick, doped $V_{0.42}(Bi_{0.20}Sb_{0.80})_{1.58}Te_3$ layer (8.3 at.% V), respectively. (c) XRR scans of layers with increasing V content up to 8.3 at.% (offset for clarity). (d) RMS roughness determined by XRR (black) and AFM (red) depending on V content.

Next, the morphology of the layers is investigated by AFM and XRR measurements. Fig. 8.2 (a) and (b) show 2×2 µm^2 AFM images of an undoped layer and a highly doped layer with 8.3 at.% V, respectively. On the surface of the undoped layer triangular islands with a diameter of about 100 nm and a height of about 10 nm are observed. On the other hand, the surface of the highly doped layer exhibits irregularly shaped islands of similar diameter, but a reduced height of about 3 nm. The layers with increasing V content show a transition to lower island heights and exhibit the irregular teardrop shape above 4 at.% V. The islands seem to be elongated along the $[11\overline{2}]$ direction of the Si substrate, which may be the direction of a slight unintentional miscut of the substrates. The RMS roughness of the layers was determined from $5\times5\,\mu\mathrm{m}^2$ images to increase the accuracy and reduce local fluctuations. The determined values shown in Fig. 8.2 (d) in red decrease significantly from 2.9 nm to 1.1 nm with increasing V content. This reduction is connected to the lower height of the island.

In Fig. 8.2 (c), XRR scans of the layers show fringes up to progressively higher angles the more V is in the layers. This indicates a decreasing roughness as observed in the AFM measurements. The RMS roughness and layer thickness were quantified by fitting the curves and are plotted in Fig. 8.2 (d) in black and in the upper panel of Fig. 8.1 (b), respectively. The determined RMS roughness, averaged over a macroscopic area, is in good agreement with the more local values from the AFM images, supporting the observation that V doping leads to smoother layers. This behavior may be caused by the reactive V promoting growth at the side of QLs, additional nucleation centers at the growth start or increasing heat radiation from the V cell. The latter is unlikely given that an increased substrate temperature would not only cause a smoothening of the surface, but also Sb desorption, which is not observed in this case.

In the following, the influence of V on the crystal structure of the host material is investigated using XRD measurements. Fig. 8.3 (a) shows $2\theta-\theta$ XRD scans of a 44 nm thick layer without V (black) and a 59 nm thick, highly doped layer with 8.3 at.% V (orange). The appearance of $00\underline{3n}$ reflections of the layer together with the 111 and 222 reflections of the Si substrate confirm parallel orientation of the corresponding planes of the crystals. No additional peaks originating from a separated V-rich phases are detected up to 8.3 at.% V. In Fig. 8.3 (b) and (c) $2\theta-\theta$ XRD scans of the symmetric $00\underline{15}$ and asymmetric 015 reflections are shown, respectively. Using equations 4.6 and 4.3, the lattice constants c and a are determined from the positions of the peak maxima and plotted against the V content in Fig. 8.3 (d). For the undoped layer, the lattice constants are $c = (30.47 \pm 0.01)$ Å and $a = (4.301 \pm 0.005)$ Å. V doping causes an anisotropic linear reduction by -0.09% for c and -0.17% for a per at.% V, respectively. Such a linear behavior

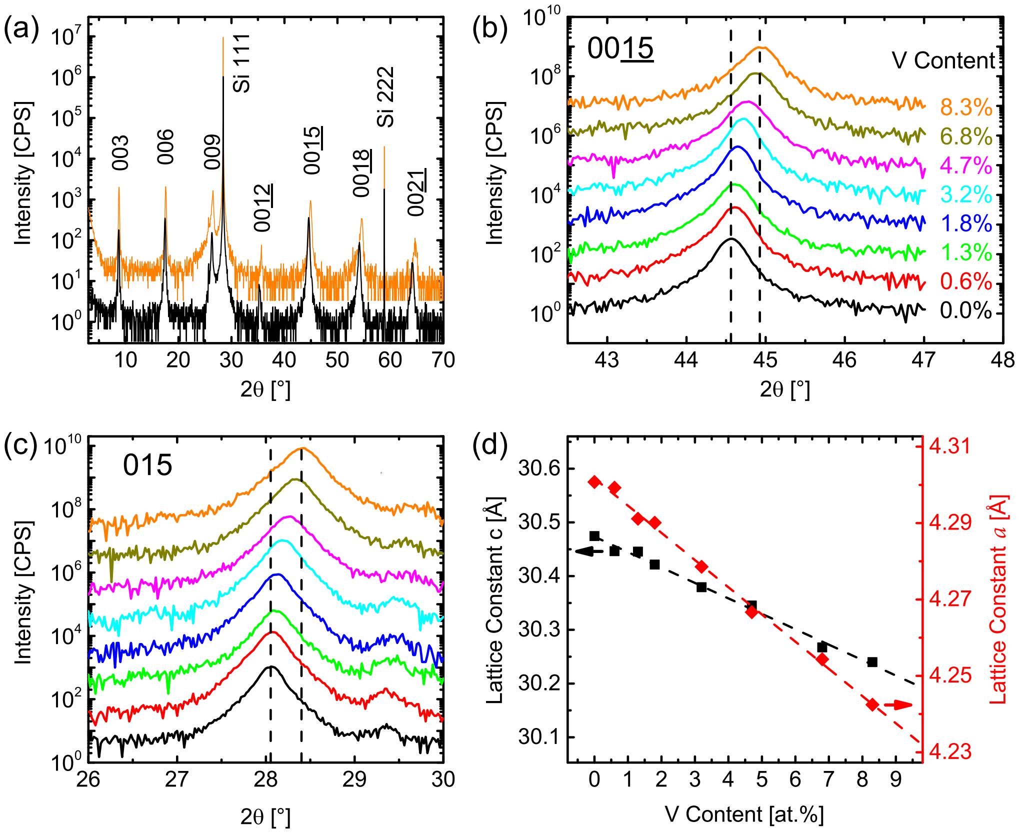

Fig. 8.3: (a) $2\theta - \theta$ XRD scans over a wide range of symmetric reflections, (b) focused on the symmetric 00<u>15</u> reflection and (c) on the asymmetric 015 reflection for layers of different V content as denoted in the color code (offset for clarity). (d) The resulting out-of-plane lattice constant c (black) and in-plane lattice constant a (red) depending on the V content of the layers.

consistent with Vegard's law is expected for substitutional incorporation of V on group-V sites and suggests rather homogeneous incorporation of V up to 8.3 at.%. Small V-rich clusters are still possible as long as they are small enough to merely affect the lattice constants of the host layer.

The observed decline of the lattice constants can be quantitatively compared to the expected reduction, assuming Bi or Sb is randomly replaced by V ions with their corresponding ionic radii. In a slightly simplified model, a van-der-Waals gap of 3.2 Å and an angle of 90° between the octahedral bonds within the QLs are assumed, neglecting slight distortions of the unit cell. For the crystal radii of Bi^{3+} and Sb^{3+} an averaged value of 0.9567 Å was used and for V^{2+}, V^{3+}, V^{4+}, V^{5+} and Te^{2-} 0.93 Å, 0.78 Å, 0.72 Å, 0.68 Å and 2.07 Å.[Sha76] For V^{3+} a decrease of c and a by -0.10% and -0.15% per at.% V is calculated. This fits well to the experimental result, reproducing even the anisotropy, which in the model results from the constant van-der-Waals gap. V^{4+} would reduce the lattice constant c by -0.13% and a by -0.20%. This is close enough to the experimental results that a mixture of V^{3+} and V^{4+} can not be ruled out. The contraction for V^{5+} by -0.16% for c and -0.23% for a and for V^{2+} by -0.02% for c and -0.02% for a does not agree with the experimental data. Additionally, if V would substitute the significantly larger Te^{2-} a much stronger contraction should occur. Intercalation of V in the van-der-Waals gap would result in a constant a and an increased c, possibly accompanied by the appearance of additional phases.[DHLcvU02]

The quantitative analysis of the contraction thus suggests substitutional incorporation of V^{3+} or a mixture of V^{3+} and V^{4+} at group-V sites. This is consistent with the observation of the 2/3 ratio between V and additional Te in EDX and the absence of XRD peaks of a separated V_2Te_3 phase.

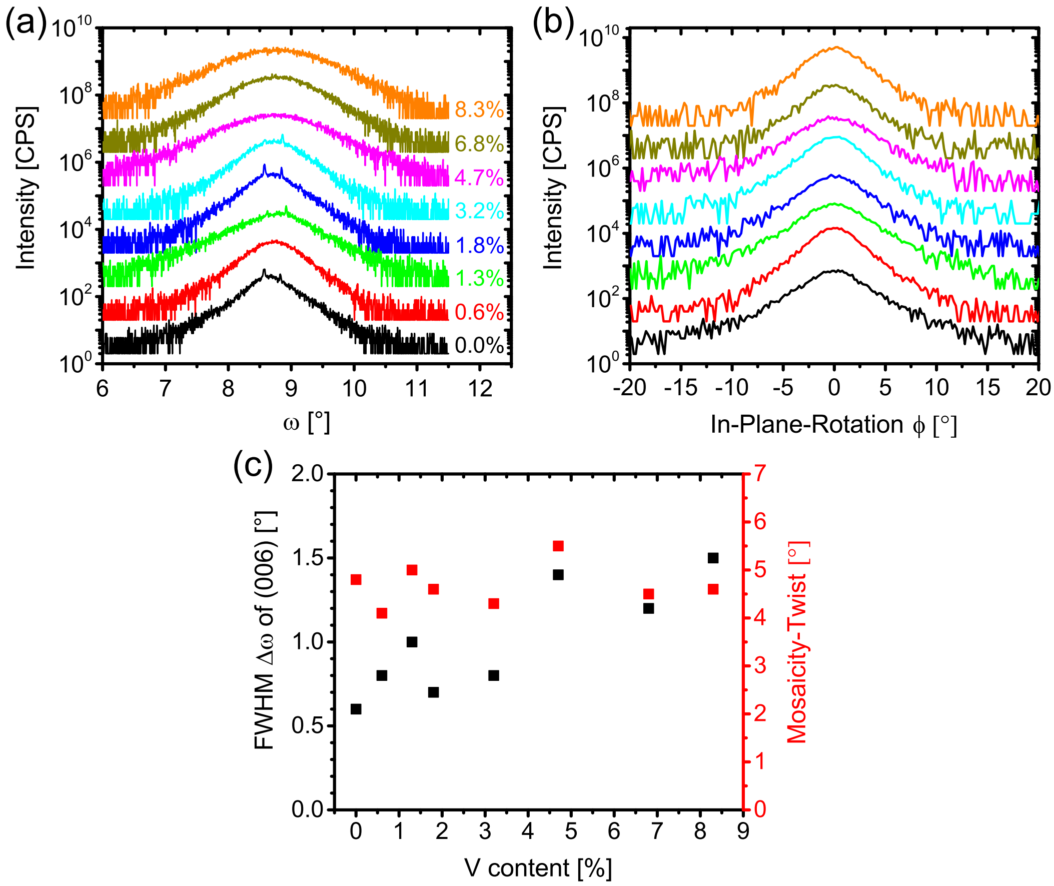

Fig. 8.4: (a) Rocking curve scans of the 006 reflection of about 50 nm thick $V_z(Bi_{0.2}Sb_{0.8})_{2-z}Te_3$ layers with the V content indicated in the legend (offset for clarity). (b) In-plane rotation diffractogram of a 015 peak with the maximum shifted to zero (offset for clarity). (c) Rocking curve FWHM and in-plane rotation FWHM against the V content.

Next, the influence of V on the crystalline quality of the layers is analyzed. Fig. 8.4 (a) shows rocking curve scans of the 006 reflection and (b) in-plane rotation diffractograms of a (015) plane with the color denoting the V content. The resulting FWHM are shown in Fig. 8.4 (c).

The FWHM of the rocking curve peak increases from $\Delta\omega = 0.6°$ up to 1.5° with increasing V content, while fluctuations of about ±0.3° are observed between individual samples. This trend indicates a deteriorating crystalline quality with increasing V doping. A Williamson-Hall like analysis is performed as outlined in [DLRHT11] to distinguish the cause of the broadening between increasing mosaicity-tilt and decreasing lateral crystallite size. The results (not shown) suggest that the mosaicity-tilt increases with V content and causes most of the broadening of the peak. On the other hand, the crystallite size is constant around 32 nm with a standard deviation of ±8 nm. The observed island size in AFM is consistently independent on the V content and three times larger than this crystallite size. This suggests that one island consists of several crystallites. The individual crystallites may be twin domains or vertically displaced domains like anti-phase domains, which can overgrow each other and form one coherent island on the surface.[STK$^+$13]

The in-plane rotation diffractogram exhibits six peaks as expected for twinned layers. The in-plane twist determined from the FWHM is constant around 4.8° with fluctuations of ±0.7° between individual samples. The main source of rotational disorder, the lattice mismatch between layer and substrate, changes little with V doping.[TSB$^+$12, STK$^+$13]

In the following, the magnetic properties of the layers are probed by SQUID measurements performed at 4.3 K. In Fig. 8.5 (a), the magnetization per V ion m is shown against the applied external magnetic field for some representative layers with a V content of 3.2 at.%, 4.7 at.% and 8.3 at.%. A linear contribution from diamagnetism of the substrate and holder was subtracted from the data.

A square shaped hysteresis loop is observed for layers with V content up to 4.7 at.%, indicating hard ferromagnetism with an out-of-plane easy axis. Higher V contents exhibit a deviating behavior shown for 8.3 at.%, which is possibly caused by superparamagnetic contributions.

In Fig. 8.5 (b), the saturation magnetization at 1 T is shown for the whole series. Between 1.3 at.% and 6.8 at.%, m is rather constant around 1.3 μ_B, while for 0.6 at.% and 8.3 at.% a lower value is observed. For very low V contents the average distance between V ions is much larger, which may lead to weaker magnetic coupling and less coherent alignment of the spins.

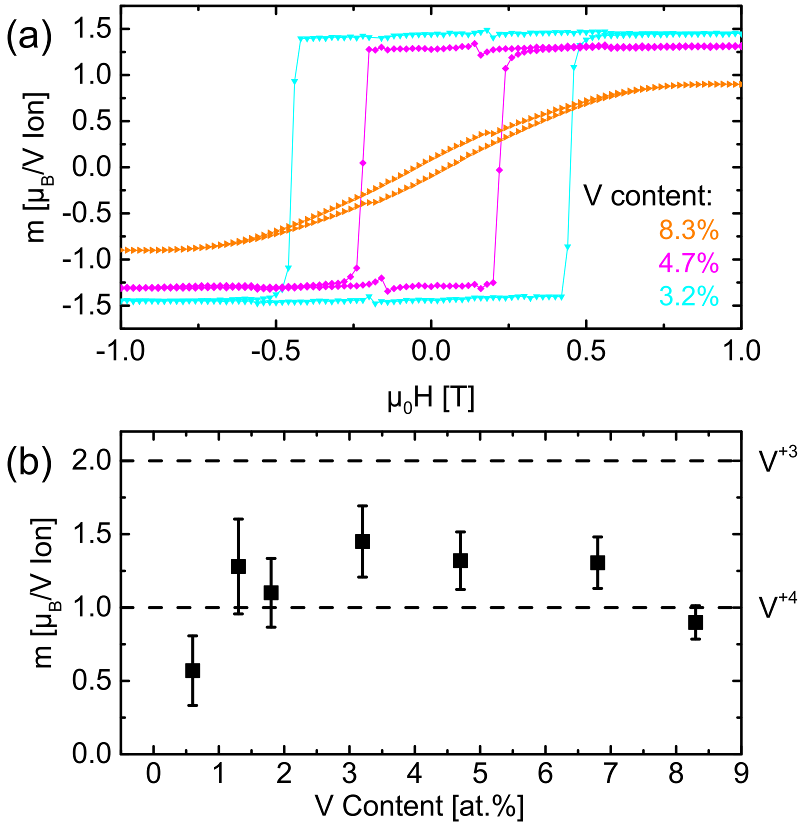

Fig. 8.5: (a) SQUID hysteresis loops of the magnetization per V ion m of layers with V content 3.2 at.%, 4.7 at.% and 8.3 at.% measured at 4.3 K. (b) Saturation magnetization at 1 T for layers with V content ranging from 0.6 at.% up to 8.3 at.%.

The observed value of $1.3\,\mu_B$ per V ion is between the expected values of $1\,\mu_B$ for V^{4+} and $2\,\mu_B$ for V^{3+}, assuming that each unpaired spin contributes $1\,\mu_B$ and the orbital contribution to the magnetic moment is negligible.[Aha00] This suggests a mixture between the two configurations in our system. Given the magnetic inhomogeneities observed in chapter 7.1, it is possible that not all V ions are ferromagnetically coupled and the spins are only partially aligned, in which case a pure V^{3+} configuration fits as well. Both possibilities are consistent with the results from the analysis of the lattice contraction.

Finally, two additional layers with even high V contents were grown to study the appearance of V-rich phases. Given that the V cell is already employed close to the maximum operation temperature, increasing the V content further is only possible by reducing the Bi and Sb flux while increasing the growth duration. For both additional layers the Bi and Sb flux was reduced by about 50% and the duration doubled. For the second layer the substrate temperature was increased to 230°, which causes Sb desorption and thus increases the V content further. Fur-

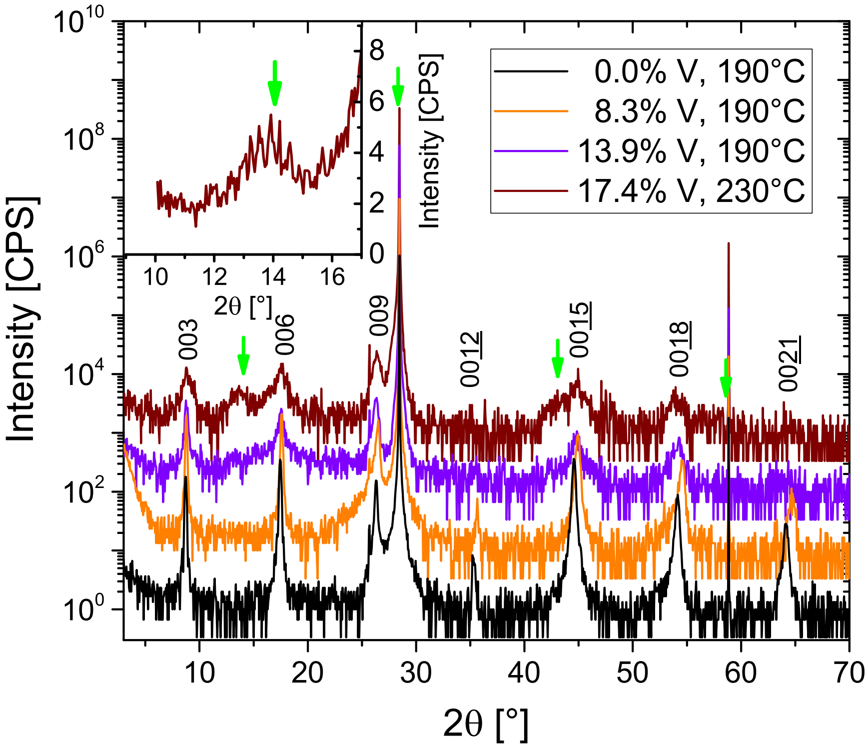

Fig. 8.6: $2\theta-\theta$ XRD scans of layers with a V content of 0 at.%, 8.3 at.%, 13.9 at.% and 17.4 at.% with the substrate temperature given in the legend. The inset shows a more accurate measurement of the peak at about 13.4° of the layer with 17.4 at.% V. The expected peak positions for the V_2Te_3 phase are marked with green arrows.

thermore, a higher temperature is expected to promote the formation of clusters due to the larger diffusion length of the atoms.

EDX measurements yield a V content of 13.9 at.% and 17.4 at.% for the two layers. For the 13.9 at.% V layer the surface follows the trend of lower roughness at higher V content and exhibits a RMS roughness of only 0.8 nm in $5\times5\,\mu m^2$ AFM images. For the layer with 17.4 at.% V the RMS roughness increases significantly to about 4 nm, possibly due to the desorption at the higher substrate temperature or due to the formation of V-rich phases.

In Fig. 8.6, $2\theta-\theta$ XRD scans of the two V-rich layers are shown with the 0 at.% V and 8.3 at.% V layers as comparison. Both V-rich layers show weak, significantly broadened peaks. A massive increase in the rocking curve FWHM of the 006 reflection indicates a strongly deteriorated crystalline quality, which causes the low intensity. The FWHM in $2\theta-\theta$ scans of high-quality layers scales inverse to the height of crystallites in the layer, which is typically equal to the layer thickness. In the present case, the V-rich layers show significant broadening despite similar layer thickness. This may indicate that the layers consist of several crystallites on top of each other, possibly separated by a V_xTe_y phase in the van-der-Waals gap. Inhomogeneous incorporation of V causing a gradient in the lattice constants may also result in such broadening.

At 17.4 at.% V, the appearance of additional peaks at 13.4°, 42.6° and about 57° as well as a shoulder at 27.9° indicate the formation of a V-rich phase. The inset shows a scan of the first of these peaks with a longer integration time. Green arrows are placed at the expected peak positions for the $00\underline{2n}$ reflections of a V_2Te_3 phase according to [RGH64]. The observed peaks are at slightly smaller angles indicating a marginally larger lattice constant c. Since the lattice constant c in [RGH64] depends on the quenching process, it is likely that the observed deviation is due to a different sample preparation and the peaks originate from the V_2Te_3 phase. A similar Cr_2Te_3 phase was observed in [TSD+17] in highly doped Cr-$(Bi,Sb)_2Te_3$. Alternatively, the peaks might also originate from a monoclinic VTe_2 phase as observed in [RGH64] and [NBE+17]. In EDX, a slightly increased Te content of 61.3% was detected, which might indicate that such a Te rich phase is present, possibly coexisting with the V_2Te_3 phase. A mixture of several phases, conceivably without simple stoichiometric composition, could also lead to the observed broadening of the peaks. While the determination of the lattice constant c is inaccurate due to the high FWHM and low intensity of the peaks, it is still evident that the two V-rich layers do no longer follow the previously observed trend of linearly decreasing lattice constants shown in Fig. 8.3. Instead, the lattice constant $c = 30.3\,\text{Å}$ seems to increase or at least stay constant, which indicates a different V incorporation consistent with the observation of V-rich phases.

Local EDX measurements at different spots of the 17.4 at.% V layer were performed with a lateral resolution of about 20 nm to probe the layer for inhomogeneities. On this length scale no lateral clustering of V could be observed in this layer. This may indicate that the V_xTe_y phases are located within the van-der-Waals gap or in tiny clusters and are distributed rather homogeneously in the lateral directions.

In conclusion, a series of layers with increasing V content shows an accumulation of incorporated V and Te in a 2/3 ratio with a corresponding increase in layer thickness. Up to 8.3 at.% V, XRD scans show a linear anisotropic lattice contraction with increasing V doping and no additional peaks from separated V-rich phases. Quantitatively, this contraction is consistent with the expected behavior for substitutional incorporation of V as V^{3+} ions or a mixture of V^{3+}/V^{4+} ions at group-V sites. The surface of the layers significantly flattens with increasing V content, possibly due to the improved nucleation with V. In SQUID measurements a magnetization of about 1.3 μ_B per V ion is observed for V contents between 1.3 at.% and 6.8 at.%. Such magnetization is consistent with both proposed valence states. At 17.4 at.% V and a higher substrate temperature the appearance of additional peaks in XRD is observed. These peaks likely originate from a V$_2$Te$_3$ or VTe$_2$ phase, which may be located within the van-der-Waals gap between the QLs.

9 Magnetically doped topological insulator heterostructures

9.1 Zero Hall plateau in trilayer heterostructures

The experimental verification of the predicted axion insulator state in magnetically doped TI heterostructures is a subject of great interest in the community. This state can presumably be realized if the magnetization at the top and bottom interface is in antiparallel configuration and is always pointing outward or inward over the whole surface of the 3D TI which causes all surface states to be gapped.[MFN15, MKT^{+}17] Such an orientation may occur in heterostructures with magnetically doped top and bottom layers with different coercive fields decoupled by an undoped layer in between.[WLQZ15] At a magnetic field between the two different coercive fields, the layer becomes insulating and the zero Hall plateau (ZHP) should be observed. In this state, exotic phenomena like the topological magnetoelectric effect may be observed.

Experimentally, a ZHP was first observed in homogeneously doped magnetic topological insulator layers.[KPW^{+}15, FFO^{+}15] The origin of this insulating phase is not the axion insulator phase, but probably scattering from random magnetic domains during the reversal of magnetization.[WLZ14]

The observation of a ZHP originating from the axion insulator state was first claimed in [MKY^{+}17] in a Cr doped (Bi,Sb)$_2$Te$_3$ heterostructure. Given that the origin of an insulating phase can not be determined from the magneto-transport experiments, magnetic domain imaging was employed to prove the antiparallel orientation of the two surface layers. For the initial observation of such a ZHP no evidence of antiparallel magnetization was found [MKY^{+}17, XJS^{+}18]. In heterostructures with Cr and V in the top and bottom layer, which exhibit a more pronounced ZHP [MKT^{+}17, XJS^{+}18], antiparallel orientation was claimed based on magnetic force microscopy at 5 K, above the observation temperature of the QAHE.[XJS+18] This may indicate that the insulating state is the predicted axion insulator state, but unambiguous evidence is still missing. In this chapter, a similar ZHP measured by Kajetan Fijalkowski in the transport group in EP3 on a V doped trilayer heterostructure is presented.

In order to realize the ZHP, symmetrically as well as asymmetrically doped trilayer heterostructures were grown. For the asymmetrically doped heterostructures the V content in the top layer is reduced to cause different coercive fields. For all layers the Sb content is fixed to 0.79, similar to the homogeneously doped layers exhibiting the QAHE. The thicknesses of the individual layers are about 2 nm (bottom), 7 nm (intermediate) and 2 nm (top). The growth of the layer stack was continuous, with the V cell shutter closed during the growth of the intermediate undoped layer, while the V cell temperature was adjusted to a lower temperature for asymmetric layers.

The inefficient nucleation of undoped $(Bi,Sb)_2Te_3$ on Si observed in previous chapters is not relevant here, given that the undoped layer is deposited on an existing $(V,Bi,Sb)_2Te_3$ layer, leading to efficient nucleation.

Magneto-transport measurements performed at 4 K show no ZHP for the asymmetric layers. Layers with 4 at.% V in the bottom layer and 2 at.% V in the top layer or 2 at.% V in the bottom layer and 1 at.% V in the top layer show only a slightly reduced σ_{xy} around the coercive field, but no clear ZHP. Layers with only 1.5 at.% V in the bottom layer and 0.7 at.% V in the top layer exhibit no ferromagnetic hysteresis at 4 K. Layers with 6.5 at.% V in the bottom layer and about 3 at.% V in the top layer have no reduced σ_{xy} around the coercive field, but a strongly reduced anomalous Hall resistivity with an inverted sign, which will be investigated in the next chapter in more detail.

In contrast to the asymmetric layers, symmetric layers with 1.5 at.% V in the doped top and bottom layer, close to the V content in homogeneous layers exhibiting the QAHE, show a more pronounced ZHP at 4 K. A subsequent measurement at 25 mK with an applied gate voltage of 7.5 V is shown in Fig. 9.1. An insulating phase with a well-defined ZHP and a dip in σ_{xx} is observed between the -1 and +1 plateau. Above the coercive field the QAHE is observed, although some residual bulk conduction likely causes the finite residual σ_{xx}. This parasitic bulk conduction may be due to the lack of optimization of the Sb content in the undoped intermediate layer.

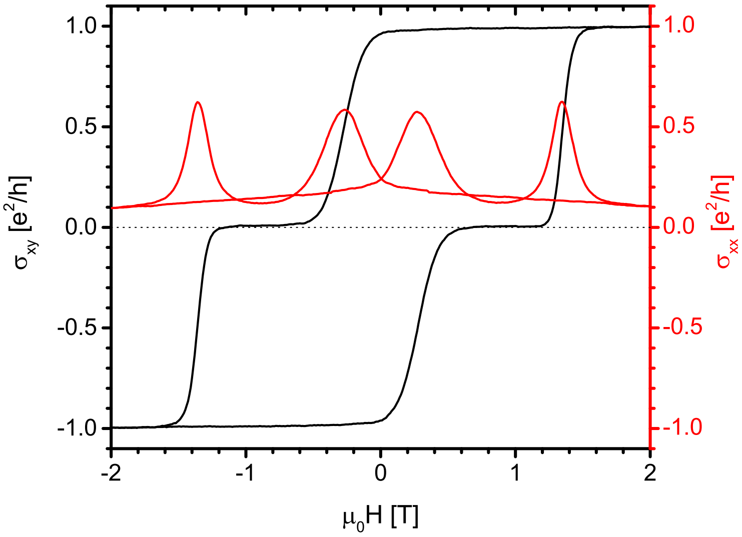

Fig. 9.1: Hall conductivity σ_{xy} (black) and longitudinal conductivity σ_{xx} (red) against the external magnetic field of a magnetic trilayer heterostructure at 25 mK with an applied gate voltage of 7.5 V.

In conclusion, the asymmetric trilayers show a deterioration of the magnetic properties likely due to the deviation from 2 at.% in the top or bottom layer. On the other hand, slight asymmetries in nominally symmetric trilayers seem to be enough to enable individual switching of the top and bottom layer. Magnetic heterostructures with nominally symmetric doping of 1.5 at.% V in 2 nm thick top and bottom layers separated by 7 nm of undoped $(Bi,Sb)_2Te_3$ exhibit a zero Hall plateau at 25 mK, which may be the axion insulator state. Similar studies published comparable results in the literature [MKY$^+$17, MKT$^+$17, XJS$^+$18] interpreting the insulating phase as the axion insulator state. Given that antiparallel magnetic orientation was not shown at the relevant mK temperatures yet, it is not fully established that the origin of the observed insulating phase is the axion insulator phase.

9.2 Inverse sign of the anomalous Hall effect in highly doped heterostructures

After the observation of an inverse sign of the anomalous Hall effect (AHE) in highly doped trilayer heterostructures in the previous chapter, this effect and its

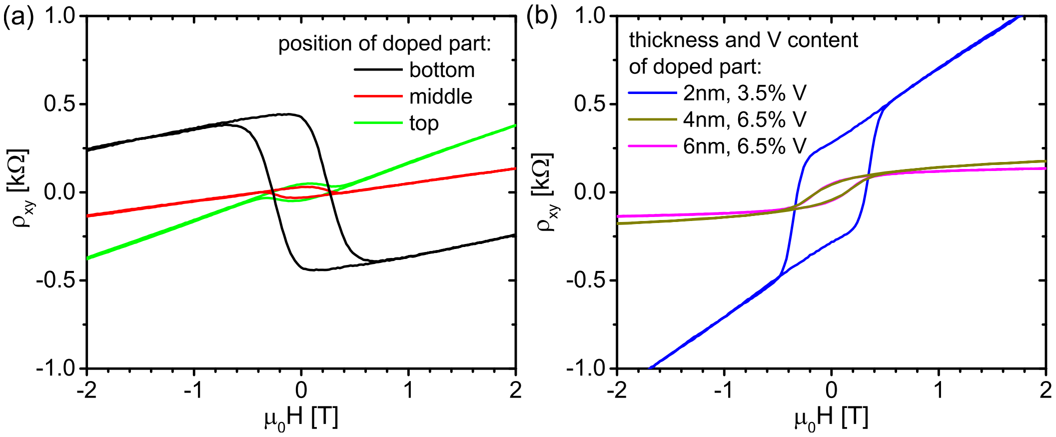

Fig. 9.2: Hall resistivity ρ_{xy} against the external magnetic field measured at 4 K for 8.5 nm thick $(Bi,Sb)_2Te_3$ layers with a highly V doped part. (a) 2 nm thick part at bottom (black), middle (red) and top (green) doped with 6.5 at.% V. (b) Top 2 nm doped with 3.5 at.% V (blue), top 4 nm doped with 6.5 at.% V (dark yellow) and top 6 nm doped with 6.5 at.% V (purple).

structural requirements are studied in this chapter. In the literature, the reversal of the sign of the AHE was reported in different compounds due to a change in composition, temperature, illumination or gate voltage.[Lav61, FJ72, OKR$^+$14, CWE$^+$10] Such an inverse sign is of particular interest in magnetic TI systems, given that it may be tied to the topological surface states and even a quantized version could exist.

The complex trilayer heterostructure was simplified to a homogeneously, highly doped layer and bilayers consisting of an undoped and a highly doped region to study the requirements of the effect. Reducing the structure to a 2 nm thin highly doped $(Bi,Sb)_2Te_3$ layer results in insulating behavior. For such low thicknesses the layer is likely not fully closed. On the other hand, 10 nm thick layers, homogeneously doped with 6.5 at.% V, do not exhibit the inverted sign. Nesting the highly doped layer in an undoped $(Bi,Sb)_2Te_3$ layer enables conduction and the influence of its thickness on the sign of the AHE can be studied.

A series of heterostructures was grown, with the top 2 nm, 4 nm and 6 nm of an overall 8.5 nm thick $(Bi,Sb)_2Te_3$ layer doped with 6.5 at.% V. Additional layers with a 2 nm thick highly doped region shifted to the middle and bottom position in the $(Bi,Sb)_2Te_3$ layer were fabricated. Lastly, the V content of a 2 nm thick doped top layer was reduced to 3.5 at.% and 1.6 at.%.

For the layers starting with undoped $(Bi,Sb)_2Te_3$ directly on Si, the loss of material due to the inefficient nucleation of such layers observed in chapter 6 has to be compensated with an increased growth duration. The resulting overall layer thickness measured by XRR is mostly consistent with the sum of the nominal thicknesses of the individual layer regions. Some deviations are likely due to a limited reproducibility of the material desorption during the nucleation of the undoped material. The thickness of the doped layer part investigated here should be unaffected.

The given V contents are based on EDX measurements of thicker calibration samples. All samples are capped with an about 10 nm thick Te cap. The magnetotransport measurements were performed by the EP3 transport group at 4 K with an applied gate voltage to maximize the anomalous Hall resistivity. Great care was taken to set up the external magnetic field, current direction and voltage probes consistently, so that the sign of the AHE can be compared.

In Fig. 9.2 (a), the Hall resistivity ρ_{xy} of the series of 8.5 nm thick $(Bi,Sb)_2Te_3$ layers with a 2 nm thick region doped with 6.5 at.% V at the bottom (black), middle (red) and top (green) is shown as a function of external magnetic field. All three layers exhibit the inverted sign of the AHE in respect to the QAHE observed in homogeneously doped layers, independent of the position of the doped layer. The anomalous Hall resistivity is nearly an order of magnitude higher if the doped region is at the bottom, which may indicate that scattering at the interfaces plays a role in the reversal of the sign.

Fig. 9.2 (b) shows the Hall resistivity ρ_{xy} of a layer with reduced V content of 3.5 at.% (blue) and of layers with increased thickness of the doped region to 4 nm (dark yellow) and 6 nm (purple) against the external magnetic field. Additionally, a bilayer with only 1.6 at.% V was measured as well (not shown here). None of the layers show the inverted sign. Apparently, a high V content of more than 3.5 at.% as well as a low thickness of the doped part are structural requirements for the inverted sign.

Notably, the anomalous Hall resistivity for all layers is far from the von Klitzing constant and the positive Hall slopes indicate a dominating residual p-type conduction at 4 K.

In conclusion, all layers containing at least one highly doped part of 6.5 at.% with a thickness of 2 nm feature an inverted sign. On the other hand, all layers with doping contents of 3.5 at.% or below or higher thicknesses of at least 4 nm show a non-inverted sign, independent of other parameters like the Sb content or the dominant carrier type.

The effect is furthermore reproducible and persists at 30 mK and over the whole gate voltage range from -9 V to 9 V. Additional SQUID measurements show that the direction of the magnetization is the same for samples with inverted and non-inverted sign. The origin of the inverted sign thus seems to be electronic. The fact that the inverted sign is observed only in thin doped layers and the anomalous Hall effect changes in magnitude depending on the interfaces of the doped layer may indicate that scattering at the interfaces causes contributions to the anomalous Hall effect of opposite sign compared to the bulk scattering effects.

10 Summary

The subject of this thesis is the fabrication and characterization of magnetic topological insulator layers of $(V,Bi,Sb)_2Te_3$ exhibiting the quantum anomalous Hall effect. A major task was the experimental realization of the quantum anomalous Hall effect, which is only observed in layers with very specific structural, electronic and magnetic properties. These properties and their influence on the quantum anomalous Hall effect are analyzed in detail.

First, the optimal conditions for the growth of pure Bi_2Te_3 and Sb_2Te_3 crystal layers and the resulting structural quality are studied. The crystalline quality of Bi_2Te_3 improves significantly at higher growth temperatures resulting in a small mosaicity-tilt and reduced twinning defects. The optimal growth temperature is determined as 260°C, low enough to avoid desorption while maintaining a high crystalline quality.

The crystalline quality of Sb_2Te_3 is less dependent on the growth temperature. Temperatures below 230°C are necessary to avoid significant material desorption, though. Especially for the nucleation on Si(111)-H, a low sticking coefficient is observed preventing the coalescence of islands into a homogeneous layer.

The influence of the substrate type, miscut and annealing sequence on the growth of Bi_2Te_3 layers is investigated. The alignment of the layer changes depending on the miscut angle and annealing sequence: Typically, layer planes align parallel to the Si(111) planes. This can enhance the twin suppression due to transfer of the stacking order from the substrate to the layer at step edges, but results in a step bunched layer morphology. For specific substrate preparations, however, the layer planes are observed to align parallel to the surface plane. This alignment avoids displacement at the step edges, which would cause anti-phase domains. This results in narrow Bragg peaks in XRD rocking curve scans due to long-range order in the absence of anti-phase domains. Furthermore, the use of rough Fe:InP(111):B substrates leads to a strong reduction of twinning defects and a significantly reduced mosaicity-twist due to the smaller lattice mismatch.

Next, the magnetically doped mixed compound $V_z(Bi_{1-x}Sb_x)_{2-z}Te_3$ is studied in order to realize the quantum anomalous Hall effect. The addition of V and Bi to Sb_2Te_3 leads to efficient nucleation on the Si(111)-H surface and a closed, homogeneous layer. Magneto-transport measurements of layers reveal a finite anomalous Hall resistivity significantly below the von Klitzing constant. The observation of the quantum anomalous Hall effect requires the complete suppression of parasitic bulklike conduction due to defect induced carriers. This can be achieved by optimizing the thickness, composition and growth conditions of the layers.

The growth temperature is observed to strongly influence the structural quality. Elevated temperatures result in bigger islands, improved crystallographic orientation and reduced twinning. On the other hand, desorption of primarily Sb is observed, affecting the thickness, composition and reproducibility of the layers. At 190°C, desorption is avoided enabling precise control of layer thickness and composition of the quaternary compound while maintaining a high structural quality.

It is especially important to optimize the Bi/Sb ratio in the $(V,Bi,Sb)_2Te_3$ layers, since by alloying n-type Bi_2Te_3 and p-type Sb_2Te_3 charge neutrality is achieved at a specific mixing ratio. This is necessary to shift the Fermi level into the magnetic exchange gap and fully suppress the bulk conduction. The Sb content x furthermore influences the in-plane lattice constant a significantly. This is utilized to accurately determine x even for thin films below 10 nm thickness required for the quantum anomalous Hall effect. Furthermore, x strongly influences the surface morphology: with increasing x the island size decreases and the RMS roughness increases by up to a factor of 4 between $x = 0$ and $x = 1$.

A series of samples with x varied between 0.56-0.95 is grown, while carefully maintaining a constant thickness of 9 nm and a doping concentration of 2 at.% V. Magneto-transport measurements reveal the charge neutral point around $x = 0.86$ at 4.2 K. The maximum of the anomalous Hall resistivity of $0.44\,h/e^2$ is observed at $x = 0.77$ close to charge neutrality. Reducing the measurement temperature to 50 mK significantly increases the anomalous Hall resistivity. Several samples in a narrow range of x between 0.76-0.79 show the quantum anomalous Hall effect with the Hall resistivity reaching the von Klitzing constant and a vanishing longitudinal resistivity. Having realized the quantum anomalous Hall effect as the first group in Europe, this breakthrough enabled us to study the electronic and magnetic properties of the samples in close collaborations with other groups.

In collaboration with the Physikalisch-Technische Bundesanstalt high-precision measurements were conducted with detailed error analysis yielding a relative deviation from the von Klitzing constant of $(0.17 \pm 0.25) \times 10^{-6}$. This is published as the smallest, most precise value at that time, proving the high quality of the provided samples. This result paves the way for the application of magnetic topological insulators as zero-field resistance standards.

Non-local magneto-transport measurements were conducted at 15 mK in close collaboration with the transport group in EP3. The results prove that transport happens through chiral edge channels. The detailed analysis of small anomalies in transport measurements reveals instabilities in the magnetic phase even at 15 mK. Their time dependent nature indicates the presence of superparamagnetic contributions in the nominally ferromagnetic phase.

Next, the influence of the capping layer and the substrate type on structural properties and the impact on the quantum anomalous Hall effect is investigated. To this end, a layer was grown on a semi-insulating Fe:InP(111)B substrate using the previously optimized growth conditions. The crystalline quality is improved significantly with the mosaicity twist reduced from 5.4° to 1.0°. Furthermore, a layer without protective capping layer was grown on Si and studied after providing sufficient time for degradation. The uncapped layer on Si shows perfect quantization, while the layer on InP deviates by about 5%. This may be caused by the higher crystalline quality, but variations in e.g. Sb content cannot be ruled out as the cause. Overall, the quantum anomalous Hall effect seems robust against changes in substrate and capping layer with only little deviations.

Furthermore, the dependence of the quantum anomalous Hall effect on the thickness of the layers is investigated. Between 5-8 nm thickness the material typically transitions from a 2D topological insulator with hybridized top and bottom surface states to a 3D topological insulator. A set of samples with 6 nm, 8 nm, and 9 nm thickness exhibits the quantum anomalous Hall effect, while 5 nm and 15 nm thick layers show significant bulk contributions. The analysis of the longitudinal and Hall conductivity during the reversal of magnetization reveals distinct differences between different thicknesses. The 6 nm thick layer shows scaling consistent with the integer quantum Hall effect, while the 9 nm thick layer shows scaling expected for the topological surface states of a 3D topological insulator. The unique scaling of the 9 nm thick layer is of particular interest as it may be a result of axion electrodynamics in a 3D topological insulator.

Subsequently, the influence of V doping on the structural and magnetic properties of the host material is studied systematically. Similarly to Bi alloying, increased V doping seems to flatten the layer surface significantly. With increasing V content, Te bonding partners are observed to increase simultaneously in a 2:3 ratio as expected for V incorporation on group-V sites. The linear contraction of the in-plane and out-of-plane lattice constants with increasing V doping is quantitatively consistent with the incorporation of V^{3+} ions, possibly mixed with V^{4+} ions, at the group-V sites. This is consistent with SQUID measurements showing a magnetization of $1.3\,\mu_B$ per V ion.

Finally, magnetically doped topological insulator heterostructures are fabricated and studied in magneto-transport. Trilayer heterostructures with a non-magnetic $(Bi,Sb)_2Te_3$ layer sandwiched between two magnetically doped layers are predicted to host the axion insulator state if the two magnetic layers are decoupled and in antiparallel configuration. Magneto-transport measurements of such a trilayer heterostructure with 7 nm undoped $(Bi,Sb)_2Te_3$ between 2 nm thick layers doped with 1.5 at.% V exhibit a zero Hall plateau representing an insulating state. Similar results in the literature were interpreted as axion insulator state, but in the absence of a measurement showing the antiparallel magnetic orientation other explanations for the insulating state cannot be ruled out.

Furthermore, heterostructures including a 2 nm thin, highly V doped layer region show an anomalous Hall effect of opposite sign compared to previous samples. A dependency on the thickness and position of the doped layer region is observed, which indicates that scattering at the interfaces causes contributions to the anomalous Hall effect of opposite sign compared to bulk scattering effects.

Many interesting phenomena in quantum anomalous Hall insulators as well as axion insulators are still not unambiguously observed. This includes Majorana bound states in quantum anomalous Hall insulator/superconductor hybrid systems and the topological magneto-electric effect in axion insulators. The limited observation temperature of the quantum anomalous Hall effect of below 1 K could be increased in 3D topological insulator/magnetic insulator heterostructures which utilize the magnetic proximity effect.

The main achievement of this thesis is the reproducible growth and characterization of $(V,Bi,Sb)_2Te_3$ layers exhibiting the quantum anomalous Hall effect. The detailed study of the structural requirements of the quantum anomalous Hall effect and the observation of the unique axionic scaling behavior in 3D magnetic topological insulator layers leads to a better understanding of the nature of this new quantum state. The high-precision measurements of the quantum anomalous Hall effect reporting the smallest deviation from the von Klitzing constant are an important step towards the realization of a zero-field quantum resistance standard.

Zusammenfassung

Das Thema dieser Arbeit ist die Herstellung und Charakterisierung von Schichten des magnetischen topologischen Isolators $(V,Bi,Sb)_2Te_3$, die den Quanten anomalen Hall-Effekt zeigen. Die Hauptaufgabe war die experimentelle Realisierung des Quanten anomalen Hall-Effekts, welcher nur in Schichten mit bestimmten strukturellen, elektronischen und magnetischen Eigenschaften beobachtet wird. Diese Eigenschaften wurden ermittelt und ihr Einfluss genau analysiert.

Als Erstes wurden die optimalen Bedingungen für das Wachstum von reinen Bi_2Te_3 und Sb_2Te_3 Kristallschichten und die resultierende strukturelle Qualität untersucht. Die kristalline Qualität von Bi_2Te_3 verbessert sich signifikant bei hohen Wachstumstemperaturen, welche die Neigung der Domänen verringern und Zwillingsdefekte reduzieren. Als optimale Wachstumstemperatur wurde 260°C ermittelt, ausreichend niedrig um Desorption zu vermeiden während eine hohe Kristallqualität erhalten bleibt.

Die Wachstumstemperatur von Sb_2Te_3 hat einen geringeren Einfluss auf die Kristallqualität. Temperaturen unter 230°C sind allerdings nötig um erhebliche Desorption zu vermeiden. Ein geringer Haftkoeffizient wurde besonders bei der Nukleation auf der Si(111)-H Oberfläche beobachtet und verhindert das Zusammenwachsen von Inseln zu einer homogenen Schicht.

Der Einfluss des Substrattyps, der Fehlorientierung der Oberfläche und der Ausheizsequenz auf das Wachstum von Bi_2Te_3 Schichten wurde untersucht. Die Ausrichtung der Schicht ändert sich je nach Winkel der Fehlorientierung und der Ausheilsequenz: Typischerweise orientieren sich die Ebenen der Schicht parallel zu den Si(111) Ebenen, was aufgrund des Transfers der Stapelfolge vom Substrat zur Schicht an den Stufenkanten die Unterdrückung von Zwillingsdefekte verbessert. Andererseits führt diese Orientierung zu Anti-Phasen-Domänen durch die Verschiebung an den Stufenkanten und zu einer gestuften Oberflächenmorphologie. Für bestimmte Substratpräparationen richtet sich die Schicht jedoch parallel zur Oberfläche aus. Diese Orientierung verhindert Verschiebungen an Stufenkanten

und damit Anti-Phasen-Domänen. Dies führt aufgrund der langreichweitigen Ordnung zu sehr schmalen Bragg-Reflexen in XRD rocking curve Diffraktogrammen. Weiterhin führen raue Fe:InP(111):B Substrate zu einer starken Unterdrückung von Zwillingsdefekten und aufgrund der besseren Gitteranpassung zu einer deutlich verringerten Verdrehung der Domänen.

Als Nächstes wurde das magnetisch dotierte $V_z(Bi_{1-x}Sb_x)_{2-z}Te_3$ untersucht mit dem Ziel den Quanten anomalen Hall-Effekt zu realisieren. Die Zugabe von V und Bi zu Sb_2Te_3 führt zu einer effizienten Nukleation auf der Si(111)-H Oberfläche und einer geschlossenen, homogenen Schicht. Magnetotransport Messungen der Schichten ergeben einen messbaren anomalen Hall-Widerstand deutlich unter der von-Klitzing-Konstanten. Die Beobachtung des Quanten anomalen Hall-Effekts setzt eine vollständige Unterdrückung der defekt-induzierten, parasitären Leitfähigkeit im Inneren der Schicht voraus. Dies kann durch die Optimierung der Dicke, Zusammensetzung und Wachstumsbedingungen der Schicht erreicht werden.

Beobachtungen zeigen, dass die Wachstumstemperatur die strukturelle Qualität stark beeinflusst. Erhöhte Temperaturen erzielen größere Inseln, eine verbesserte kristalline Orientierung und weniger Zwillingsdefekte. Andererseits wird Desorption von überwiegend Sb beobachtet, was sich auf die Dicke, Zusammensetzung und Reproduzierbarkeit der Schichten auswirkt. Bei 190°C kann Desorption vermieden werden, was eine präzise Kontrolle über Schichtdicke und Zusammensetzung des quaternären Verbunds ermöglicht, während eine hohe strukturelle Qualität erhalten bleibt.

Es ist besonders wichtig das Bi/Sb Verhältnis zu optimieren, da durch das Legieren des n-Typ Bi_2Te_3 mit dem p-Typ Sb_2Te_3 bei einem bestimmten Verhältnis Ladungsneutralität erzielt wird. Dies ist nötig um die Leitung im Inneren der Schicht vollständig zu unterdrücken und die Fermikante in die magnetische Austauschlücke zu schieben. Der Sb Gehalt x beeinflusst außerdem die Gitterkonstante a in der Ebene deutlich, im Gegensatz zur Gitterkonstante c in Wachstumsrichtung. Mit Hilfe dieses Zusammenhangs kann x selbst in dünnen Schichten unter 10 nm Dicke, wie sie für den Quantum anomalen Hall-Effekt benötigt werden, genau bestimmt werden. Der Sb Gehalt x beeinflusst weiterhin die Oberflächenmorphologie deutlich: mit steigenden x verringert sich die Inselgröße und die RMS Rauigkeit wächst um bis zu einem Faktor 4 zwischen $x = 0$ und $x = 1$.

Eine Probenserie mit x zwischen $0{,}56-0{,}95$ wurde hergestellt, wobei darauf geachtet wurde eine konstante Dicke von 9 nm und eine Dotierkonzentration von 2 at.% V beizubehalten. Magnetotransport Messungen bei 4,2 K zeigen Ladungsneutralität bei $x = 0{,}86$. Der maximale anomale Hall-Widerstand von $0{,}44\,h/e^2$ wird bei $x = 0{,}77$ nahe der Ladungsneutralität beobachtet. Wird die Messtemperatur auf 50 mK reduziert, steigt der anomale Hall-Widerstand signifikant an. Mehrere Proben mit x in einem schmalen Bereich von $0{,}76 - 0{,}79$ zeigen den Quanten anomalen Hall-Effekt mit einem Hall-Widerstand, der die von-Klitzing-Konstante erreicht, und verschwindendem longitudinalen Widerstand. Die Realisierung des Quantum anomalen Hall-Effekts als erste Gruppe in Europa ermöglichte es uns die elektrischen und magnetischen Eigenschaften der Proben in Zusammenarbeit mit anderen Gruppen zu untersuchen.

In Kollaboration mit der Physikalisch-Technische Bundesanstalt wurden Hochpräzisionsmessungen mit detaillierter Fehleranalyse durchgeführt und eine relative Abweichung von der von-Klitzing-Konstante von $(0{,}17 \pm 0{,}25) \times 10^{-6}$ erzielt. Dieser Wert wurde als kleinster und genauester Wert publiziert, was die hohe Qualität der zur Verfügung gestellten Proben zeigt. Dieses Ergebnis ebnet den Weg für die Anwendung von magnetischen topologischen Isolatoren als Widerstand Standards ohne Magnetfeld.

In enger Zusammenarbeit mit der Transport Gruppe in der EP3 wurden nichtlokale Magnetotransport Messungen bei 15 mK durchgeführt. Das Ergebnis beweist, dass Transport durch chirale Randkanäle erfolgt. Die detaillierte Analyse kleiner Anomalien in Transport Messungen offenbart Instabilitäten in der magnetischen Phase selbst bei 15 mK. Der zeitabhängige Charakter dieser Anomalien weist auf superparamagnetische Anteile in der nominell ferromagnetischen Phase hin.

Als nächstes wurde der Einfluss der Deckschicht und des Substrattyps auf die strukturellen Eigenschaften und die Auswirkungen auf den Quanten anomalen Hall-Effekt untersucht. Dazu wurde eine Schicht auf halbisolierendem Fe:InP(111)B Substrat unter den zuvor optimierten Wachstumsbedingungen gewachsen. Dies führt zu einer deutlich erhöhten kristallinen Qualität mit einem verringerten Verdrehungswinkel von 5,4° auf 1,0°. Weiterhin wurde eine Schicht ohne schützende Deckschicht auf Si gewachsen und, nachdem ausreichend Zeit für mögliche Degradation vergangen war, gemessen. Die Schicht auf Si ohne Deckschicht zeigt perfekte Quantisierung, während die Schicht auf InP eine Abweichung von etwa 5% aufweist. Ursache könnte die höhere kristalline Qualität sein, Variationen in z.B. Sb Gehalt könnten jedoch auch eine Rolle spielen. Insgesamt scheint der Quanten anomale Hall-Effekt robust gegenüber Änderungen des Substrats und der Deckschicht zu sein.

Des Weiteren wurde die Abhängigkeit des Quanten anomalen Hall-Effekts von der Schichtdicke untersucht. Zwischen 5−8 nm Dicke wechselt das Material typischerweise von einem 2D topologischen Isolator mit hybridisierten oberen und unteren Oberflächenzustand zu einem 3D topologischen Isolator. Eine Probenreihe mit 6 nm, 8 nm und 9 nm Schichtdicke zeigt den Quanten anomalen Hall-Effekt, während 5 nm und 15 nm dicke Schichten deutliche Beiträge aus dem Volumen haben. Die Analyse der longitudinalen- und Hall-Leitfähigkeit während der Umkehrung der Magnetisierung offenbart eindeutige Unterschiede. Die 6 nm dicke Schicht zeigt ein Skalierungsverhalten konsistent mit dem ganzzahligen Quanten-Hall-Effekt, die 9 nm dicke Schicht dagegen zeigt das erwartete Skalierungsverhalten für die topologischen Oberflächenzustände eines 3D topologischen Isolators. Das besondere Skalierungsverhalten der 9 nm dicken Schicht ist von besonderem Interesse, da es der axionischen Elektrodynamik in einem 3D topologischen Isolator entspringen könnte.

Anschließend wird der Einfluss von V Dotierung auf die strukturellen und magnetischen Eigenschaften der Schichten systematisch untersucht. Ähnlich wie das Legieren mit Bi, scheint V Dotieren die Oberfläche deutlich zu glätten. Mit steigenden V Gehalt erhöht sich die Zahl der Te Bindungspartner simultan im 2:3 Verhältnis, wie erwartet für den Einbau von V auf Gruppe-V Plätzen. Die lineare Kontraktion der Gitterkonstanten in der Ebene und senkrecht dazu mit steigender V Dotierung ist quantitativ konsistent mit dem Einbau von V^{3+} Ionen, möglicherweise gemischt mit V^{4+} Ionen, auf Gruppe-V Plätzen. Dies ist konsistent mit SQUID Messungen die eine Magnetisierung von $1{,}3\,\mu_B$ pro V Ion zeigen.

Schließlich werden magnetisch dotierte topologische Isolator Heterostrukturen hergestellt und in Magnetotransport Messungen charakterisiert. Der Axion-Isolator Zustand wurde in dreischichtigen Heterostrukturen mit einer nichtmagnetischen $(Bi,Sb)_2Te_3$ Lage zwischen zwei magnetischen Schichten vorhergesagt, falls die beiden magnetischen Lagen entkoppelt sind und in antiparalleler Ausrichtung vorliegen. Magnetotransport Messungen solcher dreischichtigen Heterostrukturen mit 7 nm undotiertem $(Bi,Sb)_2Te_3$ zwischen jeweils 2 nm dicken dotierten Schichten mit 1,5 at.% V zeigen ein Null Hall-Plateau, das einen isolierenden Zustand repräsentiert. Ähnliche Ergebnisse in der Literatur wurden als Axion-Isolator Zustand interpretiert, jedoch können andere Erklärungen ohne eine direkten Messung der antiparallelen magnetischen Orientierung nicht ausgeschlossen werden.

Weiterhin zeigen Heterostrukturen mit einer 2 nm dünnen, hoch V dotierten Schicht einen anomalen Hall-Effekt mit entgegengesetzten Vorzeichen im Vergleich zu vorhergehenden Proben. Die Abhängigkeit von der Dicke und Position dieser Schicht könnte darauf hindeuten, dass Streuprozesse an den Grenzflächen einen

Beitrag zum anomalen Hall-Effekt entgegengesetzt zu den Volumenstreuprozessen verursachen.

Viele interessante Phänomene in Quanten anomalen Hall Isolatoren sowie Axion-Isolatoren sind noch nicht eindeutig beobachtet worden. Dies schließt gebundene Majorana-Zustände in Quanten anomalen Hall Isolator/Supraleiter Hybridsystemen und den topologischen magneto-elektrischen Effekt in Axion-Isolatoren ein. Die limitierte Beobachtungstemperatur des Quanten anomalen Hall-Effekts von unter 1 K könnte in Heterostrukturen aus 3D topologischen Isolator und magnetischen Isolator Schichten welche den magnetischen Proximity-Effekt nutzen erhöht werden.

Das wichtigste Ergebnis dieser Arbeit ist das reproduzierbare Wachstum und die Charakterisierung von $(V,Bi,Sb)_2Te_3$ Schichten die den Quanten anomalen Hall-Effekt zeigen. Die detaillierte Untersuchung der strukturellen Voraussetzungen und die Beobachtung des besonderen axionischen Skalierungsverhaltens in 3D magnetischen Isolatorschichten führt zu einem besseren Verständnis dieses neuen Quantenzustands. Die Hochpräzisionsmessungen des Quanten anomalen Hall-Effekts mit der geringsten Abweichung von der von-Klitzing-Konstanten sind ein wichtiger Schritt zur Realisierung eines Widerstand-Standards basierend auf Quantisierung ohne magnetischem Feld.

Bibliography

[Aha00] A. Aharoni. *Introduction to the theory of ferromagnetism.* International Series of monographs on physics. Oxford University Press, second edition edition (2000).

[And13] Y. Ando. Topological insulator materials. *Journal of the Physical Society of Japan*, **82**, 102001 (2013).

[ANS98] T. Ando, T. Nakanishi, and R. Saito. Berry's phase and absence of back scattering in carbon nanotubes. *Journal of the Physical Society of Japan*, **67**, 2857 (1998).

[BFK$^+$15] A. Bestwick, E. Fox, X. Kou, L. Pan, K. L. Wang, and D. Goldhaber-Gordon. Precise quantization of the anomalous Hall effect near zero magnetic field. *Physical Review Letters*, **114**, 187201 (2015).

[Bir06] M. Birkholz. *Thin film analysis by X-ray scattering.* John Wiley & Sons (2006).

[Büt86] M. Büttiker. Four-terminal phase-coherent conductance. *Physical Review Letters*, **57**, 1761 (1986).

[BZ06] B. A. Bernevig and S.-C. Zhang. Quantum Spin Hall Effect. *Physical Review Letters*, **96**, 106802 (2006).

[CAC$^+$09] Y. L. Chen, J. G. Analytis, J.-H. Chu, Z. K. Liu, S.-K. Mo, X. L. Qi, H. J. Zhang, D. H. Lu, X. Dai, Z. Fang, S. C. Zhang, I. R. Fisher, Z. Hussain, and Z.-X. Shen. Experimental realization of a three-dimensional topological insulator, Bi_2Te_3. *Science*, **325**, 178 (2009).

[CCC$^+$04] J. Choi, S. Choi, J. Choi, Y. Park, H.-M. Park, H.-W. Lee, B.-C. Woo, and S. Cho. Magnetic properties of Mn-doped Bi_2Te_3 and Sb_2Te_3. *Physica Status Solidi (b)*, **241**, 1541 (2004).

[CKD$^+$99] S. Cho, Y. Kim, A. DiVenere, G. K. Wong, J. B. Ketterson, and J. R. Meyer. Antisite defects of Bi_2Te_3 thin films. *Applied Physics Letters*, **75**, 1401 (1999).

[CL02] Y. Cui and L. Li. Evolution of spirals during molecular beam epitaxy of GaN on 6H-SiC(0001). *Physical Review B*, **66**, 155330 (2002).

[CWE+10] D. Chiba, A. Werpachowska, M. Endo, Y. Nishitani, F. Matsukura, T. Dietl, and H. Ohno. Anomalous Hall Effect in Field-Effect Structures of (Ga,Mn)As. *Physical Review Letters*, **104**, 106601 (2010).

[CYT+14] J. Checkelsky, R. Yoshimi, A. Tsukazaki, K. Takahashi, Y. Kozuka, J. Falson, M. Kawasaki, and Y. Tokura. Trajectory of the anomalous Hall effect towards the quantized state in a ferromagnetic topological insulator. *Nature Physics*, **10**, 731 (2014).

[CZF+13] C.-Z. Chang, J. Zhang, X. Feng, J. Shen, Z. Zhang, M. Guo, K. Li, Y. Ou, P. Wei, L.-L. Wang, Z.-Q. Ji, Y. Feng, S. Ji, X. Chen, J. Jia, X. Dai, Z. Fang, S.-C. Zhang, K. He, Y. Wang, L. Lu, X.-C. Ma, and Q.-K. Xue. Experimental Observation of the Quantum Anomalous Hall Effect in a Magnetic Topological Insulator. *Science*, **340**, 167 (2013).

[CZK+15a] C.-Z. Chang, W. Zhao, D. Y. Kim, P. Wei, J. Jain, C. Liu, M. H. Chan, and J. S. Moodera. Zero-field dissipationless chiral edge transport and the nature of dissipation in the quantum anomalous Hall state. *Physical Review Letters*, **115**, 057206 (2015).

[CZK+15b] C.-Z. Chang, W. Zhao, D. Y. Kim, H. Zhang, B. A. Assaf, D. Heiman, S.-C. Zhang, C. Liu, M. H. W. Chan, and J. S. Moodera. High-precision realization of robust quantum anomalous Hall state in a hard ferromagnetic topological insulator. *Nature*, **14**, 473 (2015).

[CZK+15c] C.-Z. Chang, W. Zhao, D. Y. Kim, H. Zhang, B. A. Assaf, D. Heiman, S.-C. Zhang, C. Liu, M. H. W. Chan, and J. S. Moodera. Supplemental Material: High-precision realization of robust quantum anomalous Hall state in a hard ferromagnetic topological insulator. *Nature*, **14**, 473 (2015).

[CZU05] Y.-J. Chien, Z. Zhou, and C. Uher. Growth and transport properties of $Sb_{2-x}V_xTe_3$ thin films on sapphire substrates. *Journal of Crystal Growth*, **283**, 309 (2005).

[DHLcvU02] J. S. Dyck, P. Hájek, P. Lošt'ák, and C. Uher. Diluted magnetic semiconductors based on $Sb_{2-x}V_xTe_3$ ($0.01 <\sim x <\sim 0.03$). *Physical Review B*, **65**, 115212 (2002).

[DLRHT11] O. Durand, A. Letoublon, D. Rogers, and F. Hosseini Teherani. Interpretation of the two-components observed in high resolution X-ray diffraction ω scan peaks for mosaic ZnO thin films grown on c-sapphire substrates using pulsed laser deposition. *Thin Solid Films*, **519**, 6369 (2011).

[Dol99] B. P. Dolan. Modular invariance, universality and crossover in the quantum Hall effect. *Nuclear Physics B*, **554**, 487 (1999).

[DRCJ$^+$07] D. Drouin, A. Réal Couture, D. Joly, X. Tastet, V. Aimez, and R. Gauvin. CASINO V2.42-A Fast and Easy-to-use Modeling Tool for Scanning Electron Microscopy and Microanalysis Users. *Scanning*, **29**, 92 (2007).

[dVPM$^+$17] E. K. de Vries, S. Pezzini, M. J. Meijer, N. Koirala, M. Salehi, J. Moon, S. Oh, S. Wiedmann, and T. Banerjee. Coexistence of bulk and surface states probed by Shubnikov–de Haas oscillations in Bi_2Se_3 with high charge-carrier density. *Physical Review B*, **96**, 045433 (2017).

[DWSY17] J. W. Dankanich, M. Walker, M. W. Swiatek, and J. T. Yim. Recommended Practice for Pressure Measurement and Calculation of Effective Pumping Speed in Electric Propulsion Testing. *Journal of Propulsion and Power*, **33**, 668 (2017).

[EMV09] A. M. Essin, J. E. Moore, and D. Vanderbilt. Magnetoelectric polarizability and axion electrodynamics in crystalline insulators. *Physical Review Letters*, **102**, 146805 (2009).

[FFO$^+$15] Y. Feng, X. Feng, Y. Ou, J. Wang, C. Liu, L. Zhang, D. Zhao, G. Jiang, S.-C. Zhang, K. He, X. Ma, Q.-K. Xue, and Y. Wang. Observation of the Zero Hall Plateau in a Quantum Anomalous Hall Insulator. *Physical Review Letters*, **115**, 126801 (2015).

[FFW$^+$16] X. Feng, Y. Feng, J. Wang, Y. Ou, Z. Hao, C. Liu, Z. Zhang, L. Zhang, C. Lin, J. Liao, Y. Li, L. Wang, S. Ji, X. Chen, X. Ma, S. Zhang, Y. Wang, K. He, and Q. Xue. Thickness Dependence of the Quantum Anomalous Hall Effect in Magnetic Topological Insulator Films. *Advanced Materials*, **28**, 6386 (2016).

[FGT$^+$88] J. Fleurial, L. Gailliard, R. Triboulet, H. Scherrer, and S. Scherrer. Thermal properties of high quality single crystals of bismuth telluride-Part I: Experimental characterization. *Journal of Physics and Chemistry of Solids*, **49**, 1237 (1988).

[FJ72] A. Fert and O. Jaoul. Left-Right Asymmetry in the Scattering of Electrons by Magnetic Impurities, and a Hall Effect. *Physical Review Letters*, **28**, 303 (1972).

[FK08] L. Fu and C. L. Kane. Superconducting proximity effect and Majorana fermions at the surface of a topological insulator. *Physical Review Letters*, **100**, 096407 (2008).

[FRY+18] E. J. Fox, I. T. Rosen, Y. Yang, G. R. Jones, R. E. Elmquist, X. Kou, L. Pan, K. L. Wang, and D. Goldhaber-Gordon. Part-per-million quantization and current-induced breakdown of the quantum anomalous Hall effect. *Physical Review B*, **98**, 075145 (2018).

[GFP+18] M. Götz, K. M. Fijalkowski, E. Pesel, M. Hartl, S. Schreyeck, M. Winnerlein, S. Grauer, H. Scherer, K. Brunner, C. Gould, F. J. Ahlers, and L. W. Molenkamp. Precision measurement of the quantized anomalous Hall resistance at zero magnetic field. *Applied Physics Letters*, **112**, 072102 (2018).

[GFS+17a] S. Grauer, K. M. Fijalkowski, S. Schreyeck, M. Winnerlein, K. Brunner, R. Thomale, C. Gould, and L. W. Molenkamp. Scaling of the Quantum Anomalous Hall Effect as an Indicator of Axion Electrodynamics. *Physical Review Letters*, **118**, 246801 (2017).

[GFS+17b] S. Grauer, K. M. Fijalkowski, S. Schreyeck, M. Winnerlein, K. Brunner, R. Thomale, C. Gould, and L. W. Molenkamp. Supplemental Material: Scaling of the Quantum Anomalous Hall Effect as an Indicator of Axion Electrodynamics. *Physical Review Letters*, **118**, 1 (2017).

[GSW+15] S. Grauer, S. Schreyeck, M. Winnerlein, K. Brunner, C. Gould, and L. W. Molenkamp. Coincidence of superparamagnetism and perfect quantization in the quantum anomalous Hall state. *Physical Review B*, **92**, 201304 (2015).

[Hal88] F. D. M. Haldane. Model for a quantum Hall effect without Landau levels: Condensed-matter realization of the "parity anomaly". *Physical Review Letters*, **61**, 2015 (1988).

[Has12] S. Hasegawa. *Reflection High-Energy Electron Diffraction*, 1–14. American Cancer Society (2012).

[HFM+01] J. O. Hauch, M. Fonine, U. May, R. Calarco, H. Kittur, J. M. Choi, U. Rüdiger, and G. Güntherodt. The Growth of Transition Metals on H-Passivated Si (111) Substrates. *Advanced Functional Materials*, **11**, 179 (2001).

[HQW+08] D. Hsieh, D. Qian, L. Wray, Y. Xia, Y. S. Hor, R. J. Cava, and M. Z. Hasan. A topological Dirac insulator in a quantum spin Hall phase. *Nature*, **452**, 970 (2008).

[HRB+10] Y. S. Hor, P. Roushan, H. Beidenkopf, J. Seo, D. Qu, J. G. Checkelsky, L. A. Wray, D. Hsieh, Y. Xia, S.-Y. Xu, D. Qian, M. Z. Hasan, N. P. Ong, A. Yazdani, and R. J. Cava. Development of ferromagnetism in the doped topological insulator $Bi_{2-x}Mn_xTe_3$. *Physical Review B*, **81**, 195203 (2010).

[HTN+97] T. Hayashi, M. Tanaka, T. Nishinaga, H. Shimada, H. Tsuchiya, and Y. Otuka. (GaMn)As:GaAs-based III-V diluted magnetic semiconductors grown by molecular beam epitaxy. *Journal of Crystal Growth*, **175**, 1063 (1997).

[HvK86] J. Horák, K. Čermák, and L. Koudelka. Energy formation of antisite defects in doped Sb_2Te_3 and Bi_2Te_3 crystals. *Journal of Physics and Chemistry of Solids*, **47**, 805 (1986).

[HXY+12] L. He, F. Xiu, X. Yu, M. Teague, J. Wanjun, Y. Fan, X. Kou, M. Lang, Y. Wang, G. Huang, N.-C. Yeh, and K. L. Wang. Surface-Dominated Conduction in a 6 nm thick Bi_2Se_3 Thin Film. *Nano Letters*, **12**, 1486–1490 (2012).

[ICP+18] M. F. Islam, C. M. Canali, A. Pertsova, A. Balatsky, S. K. Mahatha, C. Carbone, A. Barla, K. A. Kokh, O. E. Tereshchenko, E. Jiménez, N. B. Brookes, P. Gargiani, M. Valvidares, S. Schatz, T. R. F. Peixoto, H. Bentmann, F. Reinert, J. Jung, T. Bathon, K. Fauth, M. Bode, and P. Sessi. Systematics of electronic and magnetic properties in the transition metal doped Sb_2Te_3 quantum anomalous Hall platform. *Physical Review B*, **97**, 155429 (2018).

[JB93] T. B. Joyce and T. J. Bullough. Beam equivalent pressure measurements in chemical beam epitaxy. *Journal of Crystal Growth*, **127**, 265 (1993).

[JF75] B. Joyce and C. Foxon. Kinetic studies of the growth of III-V compounds using modulated molecular beam techniques. *Journal of Crystal Growth*, **31**, 122 (1975).

[JSC+12] Y. Jiang, Y. Y. Sun, M. Chen, Y. Wang, Z. Li, C. Song, K. He, L. Wang, X. Chen, Q.-K. Xue, X. Ma, and S. Zhang. Fermi-Level Tuning of Epitaxial Sb_2Te_3 Thin Films on Graphene by Regulating Intrinsic Defects and Substrate Transfer Doping. *Physical Review Letters*, **108**, 066809 (2012).

[JZS+91] B. Joyce, J. Zhang, T. Shitara, J. Neave, A. Taylor, S. Armstrong, M. Pemble, and C. Foxon. Dynamics and kinetics of MBE growth. *Journal of Crystal Growth*, **115**, 338 (1991).

[KBP+15] J. Kampmeier, S. Borisova, L. Plucinski, M. Luysberg, G. Mussler, and D. Grützmacher. Suppressing Twin Domains in Molecular Beam Epitaxy Grown Bi_2Te_3 Topological Insulator Thin Films. *Crystal Growth & Design*, **15**, 390–394 (2015).

[KM05] C. L. Kane and E. J. Mele. Z_2 topological order and the quantum spin Hall effect. *Physical Review Letters*, **95**, 146802 (2005).

[KPW+15] X. Kou, L. Pan, J. Wang, Y. Fan, E. S. Choi, W.-L. Lee, T. Nie, K. Murata, Q. Shao, S.-C. Zhang, and K. L. Wang. Metal-to-insulator switching in quantum anomalous Hall states. *Nature Communications*, **6**, 8474 (2015).

[KWB+07] M. König, S. Wiedmann, C. Brüne, A. Roth, H. Buhmann, L. W. Molenkamp, X.-L. Qi, and S.-C. Zhang. Quantum spin Hall insulator state in HgTe quantum wells. *Science*, **318**, 766 (2007).

[Lav61] J. M. Lavine. Extraordinary Hall-Effect Measurements on Ni, Some Ni Alloys, and Ferrites. *Physical Review*, **123**, 1273 (1961).

[LCW+15] M. Li, C.-Z. Chang, L. Wu, J. Tao, W. Zhao, M. H. W. Chan, J. S. Moodera, J. Li, and Y. Zhu. Experimental Verification of the Van Vleck Nature of Long-Range Ferromagnetic Order in the Vanadium-Doped Three-Dimensional Topological Insulator Sb_2Te_3. *Physical Review Letters*, **114**, 146802 (2015).

[LES+15] W. Liu, L. Endicott, V. A. Stoica, H. Chi, R. Clarke, and C. Uher. High-quality ultra-flat $BiSbTe_3$ films grown by MBE. *Journal of Crystal Growth*, **410**, 23–29 (2015).

[LKK+16] M. Lanius, J. Kampmeier, S. Kölling, G. Mussler, P. Koenraad, and D. Grützmacher. Topography and structure of ultrathin topological insulator Sb_2Te_3 films on Si(111) grown by means of molecular beam epitaxy. *Journal of Crystal Growth*, **453**, 158–162 (2016).

[LNK+00] M. Lippmaa, N. Nakagawa, M. Kawasaki, S. Ohashi, and H. Koinuma. Growth mode mapping of $SrTiO_3$ epitaxy. *Applied Physics Letters*, **76**, 2439 (2000).

[LPV+98] J.-L. Lin, D. Petrovykh, J. Viernow, F. Men, D. Seo, and F. Himpsel. Formation of regular step arrays on Si (111) 7x7. *Journal of Applied Physics*, **84**, 255 (1998).

[LQD+08] C.-X. Liu, X.-L. Qi, X. Dai, Z. Fang, and S.-C. Zhang. Quantum Anomalous Hall Effect in $Hg_{1-y}Mn_yTe$ Quantum Wells. *Physical Review Letters*, **101**, 146802 (2008).

[LSY+10] H.-Z. Lu, W.-Y. Shan, W. Yao, Q. Niu, and S.-Q. Shen. Massive Dirac fermions and spin physics in an ultrathin film of topological insulator. *Physical Review B*, **81**, 115407 (2010).

[LWL12] Y. Liu, M. Weinert, and L. Li. Spiral Growth without Dislocations: Molecular Beam Epitaxy of the Topological Insulator Bi_2Se_3 on Epitaxial Graphene/SiC(0001). *Physical Review Letters*, **108**, 115501 (2012).

[LWQZ10] R. Li, J. Wang, X.-L. Qi, and S.-C. Zhang. Dynamical axion field in topological magnetic insulators. *Nature Physics*, **6**, 284 (2010).

[LZY+10] C.-X. Liu, H. Zhang, B. Yan, X.-L. Qi, T. Frauenheim, X. Dai, Z. Fang, and S.-C. Zhang. Oscillatory crossover from two-dimensional to three-dimensional topological insulators. *Physical Review B*, **81**, 041307 (2010).

[MFN15] T. Morimoto, A. Furusaki, and N. Nagaosa. Topological magnetoelectric effects in thin films of topological insulators. *Physical Review B*, **92**, 085113 (2015).

[MKS+18] J. Moon, N. Koirala, M. Salehi, W. Zhang, W. Wu, and S. Oh. Solution to the hole-doping problem and tunable quantum Hall effect in Bi_2Se_3 thin films. *Nano Letters*, **18**, 820 (2018).

[MKT+17] M. Mogi, M. Kawamura, A. Tsukazaki, R. Yoshimi, K. S. Takahashi, M. Kawasaki, and Y. Tokura. Tailoring tricolor structure of magnetic topological insulator for robust axion insulator. *Science Advances*, **3** (2017).

[MKY+17] M. Mogi, M. Kawamura, R. Yoshimi, A. Tsukazaki, Y. Kozuka, N. Shirakawa, K. Takahashi, M. Kawasaki, and Y. Tokura. A magnetic heterostructure of topological insulators as a candidate for an axion insulator. *Nature Materials*, **16**, 516 (2017).

[MMC+14] J. Manson, A. Madubuonu, D. A. Crandles, C. Uher, and P. Loš'ták. Infrared spectroscopy of Cr- and V-doped Sb_2Te_3: Dilute magnetic semiconductors. *Physical Review B*, **90**, 205205 (2014).

[Nak63] S. Nakajima. The crystal structure of $Bi_2Te_{3-x}Se_x$. *Journal of Physics and Chemistry of Solids*, **24**, 479 (1963).

[NBE+17] K. Nikonov, M. Brekhovskikh, A. Egorysheva, T. Menshchikova, and V. Fedorov. Chemical vapor transport growth of vanadium (IV) selenide and vanadium (IV) telluride single crystals. *Inorganic Materials*, **53**, 1126 (2017).

[NN11] K. Nomura and N. Nagaosa. Surface-Quantized Anomalous Hall Current and the Magnetoelectric Effect in Magnetically Disordered Topological Insulators. *Physical Review Letters*, **106**, 166802 (2011).

[O'H03] J. F. O'Hanlon. *A Users Guide to Vacuum Technology.* Wiley, 3rd edition (2003).

[OKR+14] Y. Ohuchi, Y. Kozuka, N. Rezaei, M. S. Bahramy, R. Arita, K. Ueno, A. Tsukazaki, and M. Kawasaki. Photoinduced sign inversion of the anomalous Hall effect in EuO thin films. *Physical Review B*, **89**, 121114 (2014).

[OV15] F. Ortmann and S. O. Valenzuela. *Topological insulators: Fundamentals and perspectives.* John Wiley & Sons (2015).

[PBS+16] T. R. F. Peixoto, H. Bentmann, S. Schreyeck, M. Winnerlein, C. Seibel, H. Maaß, M. Al-Baidhani, K. Treiber, S. Schatz, S. Grauer, C. Gould, K. Brunner, A. Ernst, L. W. Molenkamp, and F. Reinert. Impurity states in the magnetic topological insulator V:$(Bi,Sb)_2Te_3$. *Physical Review B*, **94**, 195140 (2016).

[PSA+15] J. Park, Y.-A. Soh, G. Aeppli, X. Feng, Y. Ou, K. He, and Q.-K. Xue. Crystallinity of tellurium capping and epitaxy of ferromagnetic topological insulator films on $SrTiO_3$. *Scientific Reports*, **5** (2015).

[QHX+10] D.-X. Qu, Y. S. Hor, J. Xiong, R. J. Cava, and N. Ong. Quantum oscillations and Hall anomaly of surface states in the topological insulator Bi_2Te_3. *Science*, **329**, 821 (2010).

[QHZ08] X.-L. Qi, T. L. Hughes, and S.-C. Zhang. Topological field theory of time-reversal invariant insulators. *Physical Review B*, **78**, 195424 (2008).

[QLZZ09] X.-L. Qi, R. Li, J. Zang, and S.-C. Zhang. Inducing a magnetic monopole with topological surface states. *Science*, **323**, 1184 (2009).

[RDD+17] C. L. Richardson, J. M. Devine-Stoneman, G. Divitini, M. E. Vickers, C.-Z. Chang, M. Amado, J. S. Moodera, and J. W. A. Robinson. Structural properties of thin-film ferromagnetic topological insulators. *Scientific Reports*, **7**, 12061 (2017).

[RGH64] E. Röst, L. Gjertsen, and H. Haraldsen. Über die Vanadintelluride und ihre magnetischen Eigenschaften. *Zeitschrift für anorganische und allgemeine Chemie*, **333**, 301 (1964).

[RTS+10] Z. Ren, A. Taskin, S. Sasaki, K. Segawa, and Y. Ando. Large bulk resistivity and surface quantum oscillations in the topological insulator Bi_2Te_2Se. *Physical Review B*, **82**, 241306 (2010).

[Sha76] R. D. Shannon. Revised effective ionic radii and systematic studies of interatomic distances in halides and chalcogenides. *Acta Crystallographica Section A*, **32**, 751 (1976).

[SHSS88] Z. Starý, J. Horák, M. Stordeur, and M. Stölzer. Antisite defects in $Sb_{2-x}Bi_xTe_3$ mixed crystals. *Journal of Physics and Chemistry of Solids*, **49**, 29 (1988).

[SKS62] M. J. Smith, R. J. Knight, and C. W. Spencer. Properties of Bi_2Te_3-Sb_2Te_3 Alloys. *Journal of Applied Physics*, **33**, 2186 (1962).

[SLF+11] H. Steinberg, J.-B. Laloë, V. Fatemi, J. S. Moodera, and P. Jarillo-Herrero. Electrically tunable surface-to-bulk coherent coupling in topological insulator thin films. *Physical Review B*, **84**, 233101 (2011).

[STK+13] S. Schreyeck, N. V. Tarakina, G. Karczewski, C. Schumacher, T. Borzenko, C. Brüne, H. Buhmann, C. Gould, K. Brunner, and L. W. Molenkamp. Molecular beam epitaxy of high structural quality Bi_2Se_3 on lattice matched InP(111) substrates. *Applied Physics Letters*, **102**, 041914 (2013).

[SWM+18] K. L. Scipioni, Z. Wang, Y. Maximenko, F. Katmis, C. Steiner, and V. Madhavan. Role of defects in the carrier-tunable topological-insulator $(Bi_{1-x}Sb_x)_2Te_3$ thin films. *Physical Review B*, **97**, 125150 (2018).

[TKNdN82] D. J. Thouless, M. Kohmoto, M. P. Nightingale, and M. den Nijs. Quantized Hall Conductance in a Two-Dimensional Periodic Potential. *Physical Review Letters*, **49**, 405 (1982).

[TNA+97] E. Tok, J. Neave, F. Allegretti, J. Zhang, T. Jones, and B. Joyce. Incorporation kinetics of As_2 and As_4 on GaAs (110). *Surface Science*, **371**, 277 (1997).

[TRS+11] A. Taskin, Z. Ren, S. Sasaki, K. Segawa, and Y. Ando. Observation of Dirac holes and electrons in a topological insulator. *Physical Review Letters*, **107**, 016801 (2011).

[TSB+12] N. V. Tarakina, S. Schreyeck, T. Borzenko, C. Schumacher, G. Karczewski, K. Brunner, C. Gould, H. Buhmann, and L. W. Molenkamp. Comparative Study of the Microstructure of Bi_2Se_3 Thin Films Grown on Si(111) and InP(111) Substrates. *Crystal Growth & Design*, **12**, 1913–1918 (2012).

[TSD+17] N. V. Tarakina, S. Schreyeck, M. Duchamp, G. Karczewski, C. Gould, K. Brunner, R. E. Dunin-Borkowski, and L. W. Molenkamp. Microstructural characterization of Cr-doped $(\mathrm{Bi,Sb})_2\mathrm{Te}_3$ thin films. *CrystEngComm*, **19**, 3633 (2017).

[TSL+14] N. V. Tarakina, S. Schreyeck, M. Luysberg, S. Grauer, C. Schumacher, G. Karczewski, K. Brunner, C. Gould, H. Buhmann, R. E. Dunin-Borkowski, and L. W. Molenkamp. Suppressing Twin Formation in $\mathrm{Bi}_2\mathrm{Se}_3$ Thin Films. *Advanced Materials Interfaces*, **1**, 1400134 (2014).

[TSS+03] T. Thonhauser, T. Scheidemantel, J. Sofo, J. Badding, and G. Mahan. Thermoelectric properties of $\mathrm{Sb}_2\mathrm{Te}_3$ under pressure and uniaxial stress. *Physical Review B*, **68**, 085201 (2003).

[WDSW82] C. Wood, D. Desimone, K. Singer, and G. Wicks. Magnesium- and calcium-doping behavior in molecular-beam epitaxial III-V compounds. *Journal of Applied Physics*, **53**, 4230 (1982).

[WLG+11] Z. Wang, H. Li, X. Guo, W. Ho, and M. Xie. Growth characteristics of topological insulator $\mathrm{Bi}_2\mathrm{Se}_3$ films on different substrates. *Journal of Crystal Growth*, **334**, 96–102 (2011).

[WLQZ15] J. Wang, B. Lian, X.-L. Qi, and S.-C. Zhang. Quantized topological magnetoelectric effect of the zero-plateau quantum anomalous Hall state. *Physical Review B*, **92**, 081107 (2015).

[WLZ14] J. Wang, B. Lian, and S.-C. Zhang. Universal scaling of the quantum anomalous Hall plateau transition. *Physical Review B*, **89**, 085106 (2014).

[WSG+17] M. Winnerlein, S. Schreyeck, S. Grauer, S. Rosenberger, K. M. Fijalkowski, C. Gould, K. Brunner, and L. W. Molenkamp. Epitaxy and structural properties of $(\mathrm{V,Bi,Sb})_2\mathrm{Te}_3$ layers exhibiting the quantum anomalous Hall effect. *Physical Review Materials*, **1**, 011201 (2017).

[WWG+92] J. Wei, X.-S. Wang, J. Goldberg, N. Bartelt, and E. D. Williams. Step-height mixtures on vicinal Si(111) surfaces. *Physical Review Letters*, **68**, 3885 (1992).

[WZS+11] G. Wang, X.-G. Zhu, Y.-Y. Sun, Y.-Y. Li, T. Zhang, J. Wen, X. Chen, K. He, L.-L. Wang, X.-C. Ma, J.-F. Jia, S. B. Zhang, and Q.-K. Xue. Topological Insulator Thin Films of $\mathrm{Bi}_2\mathrm{Te}_3$ with Controlled Electronic Structure. *Advanced Materials*, 2929 (2011).

[WZW+10] G. Wang, X. Zhu, J. Wen, X. Chen, K. He, L. Wang, X. Ma, Y. Liu, X. Dai, Z. Fang, J. Jia, and Q. Xue. Atomically smooth ultrathin films of topological insulator Sb_2Te_3. *Nano Research*, **3**, 874 (2010).

[XHW+11] F. Xiu, L. He, Y. Wang, L. Cheng, L.-T. Chang, M. Lang, G. Huang, X. Kou, Y. Zhou, X. Jiang, Z. Chen, J. Zou, A. Shailos, and K. L. Wang. Manipulating surface states in topological insulator nanoribbons. *Nature Nanotechnology*, **6**, 216 (2011).

[XJS+18] D. Xiao, J. Jiang, J.-H. Shin, W. Wang, F. Wang, Y.-F. Zhao, C. Liu, W. Wu, M. H. W. Chan, N. Samarth, and C.-Z. Chang. Realization of the Axion Insulator State in Quantum Anomalous Hall Sandwich Heterostructures. *Physical Review Letters*, **120**, 056801 (2018).

[XQH+09] Y. Xia, D. Qian, D. Hsieh, L. Wray, A. Pal, H. Lin, A. Bansil, D. Grauer, Y. S. Hor, R. J. Cava, *et al.* Observation of a large-gap topological-insulator class with a single Dirac cone on the surface. *Nature Physics*, **5**, 398 (2009).

[XZZ+13] L. Xue, P. Zhou, C. Zhang, C. He, G. Hao, L. Sun, and J. Zhong. First-principles study of native point defects in Bi_2Se_3. *AIP Advances*, **3**, 052105 (2013).

[YZZ+10a] R. Yu, W. Zhang, H.-J. Zhang, S.-C. Zhang, X. Dai, and Z. Fang. Quantized Anomalous Hall Effect in Magnetic Topological Insulators. *Science*, **329**, 61 (2010).

[YZZ+10b] R. Yu, W. Zhang, H.-J. Zhang, S.-C. Zhang, X. Dai, and Z. Fang. Quantized Anomalous Hall Effect in Magnetic Topological Insulators. *Science*, **329**, 61 (2010).

[ZCU05] Z. Zhou, Y.-J. Chien, and C. Uher. Thin-film ferromagnetic semiconductors based on $Sb_{2-x}V_xTe_3$ with T_C of 177K. *Applied Physics Letters*, **87**, 112503 (2005).

[ZCU06] Z. Zhou, Y.-J. Chien, and C. Uher. Thin film dilute ferromagnetic semiconductors $Sb_{2-x}Cr_xTe_3$ with a Curie temperature up to 190 K. *Physical Review B*, **74**, 224418 (2006).

[ZCZ+11] J. Zhang, C.-Z. Chang, Z. Zhang, J. Wen, X. Feng, K. Li, M. Liu, K. He, L. Wang, X. Chen, Q.-K. Xue, X. Ma, and Y. Wang. Band structure engineering in $(Bi_{1-x}Sb_x)_2Te_3$ ternary topological insulators. *Nature Communications*, **2** (2011).

[ZEY11] Y. Zhang, J. R. G. Evans, and S. Yang. Corrected Values for Boiling Points and Enthalpies of Vaporization of Elements in Handbooks. *Journal of Chemical & Engineering Data*, **56**, 328 (2011).

[ZHC+10] Y. Zhang, K. He, C.-Z. Chang, C.-L. Song, L.-L. Wang, X. Chen, J.-F. Jia, Z. Fang, X. Dai, W.-Y. Shan, S.-Q. Shen, Q. Niu, X.-L. Qi, S.-C. Zhang, X.-C. Ma, and Q.-K. Xue. Crossover of the three-dimensional topological insulator Bi_2Se_3 to the two-dimensional limit. *Nature Physics*, **6**, 584 (2010).

[ZLQ+09] H. Zhang, C.-X. Liu, X.-L. Qi, X. Dai, Z. Fang, and S.-C. Zhang. Topological insulators in Bi_2Se_3, Bi_2Te_3 and Sb_2Te_3 with a single Dirac cone on the surface. *Nature Physics*, **5**, 438 (2009).

Publications

Full papers - published

* Coincidence of superparamagnetism and perfect quantization in the quantum anomalous Hall state.
  S. Grauer, S. Schreyeck, **M. Winnerlein**, K. Brunner, C. Gould, and L. W. Molenkamp
  Physical Review B, **92**, 201304 (2015).

* Impurity states in the magnetic topological insulator $\mathrm{V{:}(Bi,Sb)_2Te_3}$.
  T. R. F. Peixoto, H. Bentmann, S. Schreyeck, **M. Winnerlein**, C. Seibel, H. Maaß, M. Al-Baidhani, K. Treiber, S. Schatz, S. Grauer, C. Gould, K. Brunner, A. Ernst, L. W. Molenkamp, and F. Reinert
  Physical Review B, **94**, 195140 (2016).

* Scaling of the Quantum Anomalous Hall Effect as an Indicator of Axion Electrodynamics.
  S. Grauer, K. M. Fijalkowski, S. Schreyeck, **M. Winnerlein**, K. Brunner, R. Thomale, C. Gould, and L. W. Molenkamp
  Physical Review Letters, **118**, 246801 (2017).

* Epitaxy and structural properties of $\mathrm{(V,Bi,Sb)_2Te_3}$ layers exhibiting the quantum anomalous Hall effect.
  M. Winnerlein, S. Schreyeck, S. Grauer, S. Rosenberger, K. M. Fijalkowski, C. Gould, K. Brunner, and L. W. Molenkamp
  Physical Review Materials, **1**, 011201 (2017).

* Precision measurement of the quantized anomalous Hall resistance at zero magnetic field.
  M. Götz, K. M. Fijalkowski, E. Pesel, M. Hartl, S. Schreyeck, **M. Winnerlein**, S. Grauer, H. Scherer, K. Brunner, C. Gould, F. J. Ahlers, and L. W. Molenkamp
  Physical Review Letters, **112**, 072102 (2018).

- COEXISTENCE OF SURFACE AND BULK FERROMAGNETISM MIMICS SKYRMION HALL EFFECT IN A TOPOLOGICAL INSULATOR.
  K. M. Fijalkowski, M. Hartl, **M. Winnerlein**, P. Mandal, S. Schreyeck, K. Brunner, C. Gould, and L. W. Molenkamp
  Physical Review X, **10**, 011012 (2020).

- ABSENCE OF EVIDENCE FOR CHIRAL MAJORANA MODES IN QUANTUM ANOMALOUS HALL-SUPERCONDUCTOR DEVICES.
  M. Kayyalha, D. Xiao, R. Zhang, J. Shin, J. Jiang, F. Wang, Y.-F. Zhao, R. Xiao, L. Zhang, K. M. Fijalkowski, P. Mandal, **M. Winnerlein**, C. Gould, Q. Li, L. W. Molenkamp, M. H. W. Chan, N. Samarth, and C.-Z. Chang
  Science, **367**, 64-67 (2020).

- COMPARING MAGNETIC GROUND-STATE PROPERTIES OF THE V- AND CR-DOPED TOPOLOGICAL INSULATOR $(\mathrm{Bi,Sb})_2\mathrm{Te}_3$.
  A. Tcakaev, V. B. Zabolotnyy, R. J. Green, T. R. F. Peixoto, F. Stier, M. Dettbarn, S. Schreyeck, **M. Winnerlein**, R. C. Vidal, S. Schatz, H. B. Vasili, M. Valvidares, K. Brunner, C. Gould, H. Bentmann, F. Reinert, L. W. Molenkamp, and V. Hinkov
  Physical Review B, **101**, 045127 (2020).

Full papers - submitted

- NON-LOCAL EFFECT OF IMPURITY STATES ON THE EXCHANGE COUPLING MECHANISM IN MAGNETIC TOPOLOGICAL INSULATORS.
  T. R. F. Peixoto, H. Bentmann, P. Rüßmann, A. Tcakaev, **M. Winnerlein**, S. Schreyeck, S. Schatz, R. C. Vidal, F. Stier,V. Zabolotnyy, R. J. Green, C. H. Min, C. I. Fornari, H. Maaß, H. B. Vasili, P. Gargiani, M. Valvidares, A. Barla, J. Buck, M. Hoesch, F. Diekmann, S. Rohlf, M. Kalläne, K. Rossnagel, C. Gould, K. Brunner, S. Blügel, V. Hinkov, L. W. Molenkamp, and F. Reinert
  submitted to npj Quantum Materials (2020)

Manuscripts in preparation

- INFLUENCE OF VANADIUM DOPING ON STRUCTURAL AND MAGNETIC PROPERTIES OF $(\mathrm{Bi,Sb})_2\mathrm{Te}_3$ TOPOLOGICAL INSULATOR LAYERS.
  M. Winnerlein, K. M. Fijalkowski, M. Hartl, S. Schreyeck, C. Gould, K. Brunner, and L. W. Molenkamp
  in preparation

- * An Axion Insulator Must be a Bulk Three-Dimensional Topological Insulator.
  K. M. Fijalkowski, N. Liu, M. Hartl, **M. Winnerlein**, P. Mandal, A. Coschizza, A. Fothergill, S. Grauer, S. Schreyeck, K. Brunner, R. Thomale, C. Gould, and L. W. Molenkamp
  in preparation

Acknowledgements

It is my great pleasure to thank everyone who contributed to the progress and success of this work. My thanks go to

- Prof. Dr. Karl Brunner for the excellent supervision of my work, including many detailed scientific discussions and quick and extensive feedback, while offering considerable independence.

- Prof. Dr. Laurens W. Molenkamp for accepting me at his chair of Experimental Physics III, his scientific guidance and encouragement.

- Dr. Steffen Schreyeck for sharing his considerable knowledge about MBE and experimental techniques with me and his continued support in various ways throughout my thesis.

- The transport team for many scientific discussions and explanations, the lithography and the electronic and magnetic characterization of the samples, which made this thesis possible: Prof. Charles Gould, Stefan Grauer, Kajetan Fijalkowski, Matthias Hartl and Pankaj Mandal.

- Martin Zipf, Carmen Bundschuh, Petra Wolf-Müller, Volkmar Hock and Dr. Claus Schumacher for technical assistance and their support at the MBE and in the clean room.

- Max Kessel, Mirko Trabel, Lukas Lunczer, Prof. Dr. Grzegorz Karczewski, Dr. Tanja Borzenko, Dr. Johannes Kleinlein for various advice, discussions and support.

- All the collaboration partners from different groups.

- My office colleagues Konstantin Martin, Boby Chrisol Joseph and Alwyn Antony for the nice atmosphere and welcome distractions.

- All my colleagues and former colleagues at the EP III, for the great atmosphere and cooperation as well as advice and support.

Special thanks go to my family that always showed interest in my work and supported me in many ways.